Novel effects of strains in graphene and other two dimensional materials

B. Amorim[a,b,*], A. Cortijo[a], F. de Juan[c,d], A. G. Grushin[e], F. Guinea[a,f,g], A. Gutiérrez-Rubio[a], H. Ochoa[a,h], V. Parente[a,g], R. Roldán[a], P. San-Jose[a], J. Schiefele[a], M. Sturla[i], M. A. H. Vozmediano[a]

[a] *Instituto de Ciencia de Materiales de Madrid, CSIC, Cantoblanco, E-28049 Madrid, Spain*
[b] *Department of Physics and Center of Physics, University of Minho, P-4710-057, Braga, Portugal*
[c] *Materials Science Division, Lawrence Berkeley National Laboratories, Berkeley, CA 94720, USA*
[d] *Department of Physics, University of California, Berkeley, CA 94720, USA*
[e] *Max-Planck-Institut fur Physik komplexer Systeme, 01187 Dresden, Germany*
[f] *School of Physics and Astronomy, University of Manchester, Oxford Road, Manchester M13 9PL, UK*
[g] *IMDEA Nanociencia Calle de Faraday, 9, Cantoblanco, 28049, Madrid, Spain*
[h] *Donostia International Physics Center (DIPC), 20018 San Sebastián, Spain*
[i] *IFLP-CONICET. Departamento de Física, Universidad Nacional de La Plata, (1900) La Plata, Argentina*

Abstract

The analysis of the electronic properties of strained or lattice deformed graphene combines ideas from classical condensed matter physics, soft matter, and geometrical aspects of quantum field theory (QFT) in curved spaces. Recent theoretical and experimental work shows the influence of strains in many properties of graphene not considered before, such as electronic transport, spin-orbit coupling, the formation of Moiré patterns and optics. There is also significant evidence of anharmonic effects, which can modify the structural properties of graphene. These phenomena are not restricted to graphene, and they are being intensively studied in other two dimensional materials, such as the transition metal dichalcogenides. We review here recent developments related to the role of strains in the structural and electronic properties of graphene and other two dimensional compounds.

Keywords: Graphene, 2D materials, Strain, Elasticity theory

Contents

*Corresponding author
Email address: amorim.bac@icmm.csic.es, amorim.bac@gmail.com (B. Amorim)

1. Introduction

Graphene has a number of special properties [1]. The unique combination of a two dimensional (2D) structure and massless electronic carriers leads to a variety of phenomena never considered before. These features are amplified by the high stiffness of the graphene lattice. The analysis of the electronic properties of strained or lattice deformed graphene combines ideas from classical condensed matter physics, soft matter [2, 3, 4], and geometrical aspects of quantum field theory (QFT) in curved spaces [5].

A vast literature already exists on topics such as ripples, effective gauge fields and "strain engineering" in graphene [6] and there are already a number of excellent books and reviews describing the advances in

the understanding of strain related effects [7, 8, 9]. The understanding of these phenomena has motivated the study of related effects in other 2D materials.

Recent theoretical and experimental work shows the influence of strains on many properties of graphene not considered before, such as electronic transport, spin-orbit coupling, the formation of Moiré patterns and optics. There is also significant evidence of anharmonic effects, which can modify the structural properties of graphene. These phenomena are not restricted to graphene, and they are being intensively studied in other 2D materials, such as the metallic dichalcogenides.

We review here recent developments related to the role of strains in the structural and electronic properties of graphene and other 2D compounds. We emphasize how strains influence a number of features not considered before.

The review is divided into five self–contained sections which cover the main recent developments. A summary of basic properties, formalism and notation used throughout the review are found in Section 2. This section introduces the formalism by which elastic deformations of the lattice encoded in the strain tensor of the elasticity theory couple to the electronic degrees of freedom described by the Dirac equation in the continuum limit. A symmetry approach is used to derive all possible electron–phonon couplings and their physical content is described. The "elastic" gauge fields and the deformation potential to be used through the review are defined there. This section also includes a geometrical description based on quantum field theory in curved spaces that allows to predict some new effects as the Fermi velocity as a space–dependent tensor. This formalism is also used to describe some new developments on topological properties of the materials.

Section 3 is devoted to the new developments concerning the membrane properties of the lattices. Although these aspects attracted attention from the birth of graphene [9], recent experiments [10, 11, 12] have shown that anharmonic effects in graphene and other 2D crystalline membranes have been seriously underestimated. This section describes the present situation concerning the effects of these anharmonicities on the elastic and mechanical properties of the membranes. A summary of the classical theory of flat membranes (Section 3.1.1) to fix the notations and definitions, is followed by a description of the modifications to the electron–phonon interaction due to defects (Section 3.1.2) and quantum corrections (Section 3.1.3). The modifications to the mechanical and thermodynamic properties are described in Sections 3.2, 3.3. The section concludes with an overview of the recent advances on the influence of topological defects on the membrane properties (Section 3.4).

Section 4 deals with the new developments concerning the effect of strain on the electronic properties of the samples. Particular attention is put on the analysis of the correlation between carrier mobilities and amplitudes of strain distributions demonstrated recently (Sec. 4.1). The combined influence of strain and interactions is analysed in Sec. 4.5 which addresses in particular the access to topological phases through the interplay between strain and electron-electron interactions. Interaction induced magnetic or superconducting phenomena in strained graphene are also described. The optical properties of graphene and other atomically thin materials promise a wealth of applications. In particular, graphene plasmonics in the THz and mid-infrared bands [13], as well as graphene based broadband devices working in the near-infrared and visible part of the spectrum [14], have recently attracted attention. Further, the unusual magneto-optical properties of graphene, which are determined by the nonlinear Landau level spectrum of massless Dirac Fermions [15, 16], offer a great potential for the development of non-reciprocal optical devices. Optical properties are described in Sec. 4.6.

Isolated atomic planes can now be reassembled into heterostructures made in a precisely chosen sequence [17]. Section 5 deals with the electronic properties of these new compounds that include superlattices of graphene deposited on other 2D crystals like hBN, SiC or graphene itself. The induced strains on the pristine sheet, resulting from a competition between the adhesion potential and the elasticity of the layer, are the factor ultimately determining the electronic and mechanical properties of the sheet. A general description (5.1) is followed by an analysis of the spontaneous deformations arising in the samples and their experimental consequences (5.2).

Section 6 is devoted to the new 2D materials whose synthesis followed naturally that of graphene. It includes a bibliographic summary of the on-going research in isolated mono- and few-layers of hexagonal boron nitride (hBN), molybdenum disulphide, other dichalcogenides, black phosphorus and layered oxides.

There are important aspects of the vast subject of physics of strain that have been left out of the review. Some of them have been appropriately described in previous literature [8]; others, including mechanical and numerical approaches to analyse the stability of the lattice [18], have been omitted for lack of expertise. This review is the collective work of a theory group in Madrid that has been active in the field from the beginning and continues working on it.

2. Geometric aspects: Group symmetry approach

The aim of this chapter is to discuss the minimal models for the low energy modes of graphene. Both symmetry group and differential geometry arguments are employed in order to construct effective actions for the dynamics of graphene electrons and phonon modes, and the coupling between them. The standard $\mathbf{k}\cdot\mathbf{p}$ derivation is compared with a quantum field theory approach based on the study of the Dirac equation in curved spaces. Finally, we review some topological aspects of graphene physics, with special emphasis on topological defects, closely related to the structural properties of the graphene lattice.

2.1. Electrons and phonons in graphene. Symmetry approach

The idea of constructing effective actions for physical systems based only on symmetry considerations has been extensively used both in quantum field theory (QFT) and in condensed matter physics and it lies at the heart of the Landau Fermi liquid theory of metals. In solid state systems, it is the underlying crystal group what imposes the symmetry constraints on the action describing the dynamics of both electrons and phonons.

Graphene consists on a single layer of sp^2 hybridized carbon atoms forming a honeycomb lattice, which is a triangular Bravais lattice with two atoms per unit cell. Three of the four electrons in the outer-shell participate in the strong σ bond which keeps them covalently attached forming a planar structure with a distance between atoms of $a_{CC} = 1.42$ Å. These σ electrons are responsible for the structural properties of graphene, in particular its stiffness. The remaining electrons occupying the p_z orbital perpendicular to the graphene plane are free to hop between neighbouring sites, leading to the π bands. In pristine graphene, the Fermi level lies at the two inequivalent corners of the hexagonal Brillouin zone, $K_\pm$ (see Fig. 1).

The three dimensional (3D) point group of the graphene crystal is $D_{6h} = D_6 \otimes i = C_{6v} \otimes \sigma_h$. We follow the notation of Ref. [19], which can be simplified if we only refer to the operations of the planar group, C_{6v}, that contains 12 elements: the identity, five rotations along the axis perpendicular to the graphene plane (z axis) and six reflections in planes perpendicular to it. Additionally, we have to take into account the reflection operation along the z axis, σ_h, when dealing with out-of-plane distortions.

Instead of dealing with degenerate states at two inequivalent points of the Brillouin zone one can enlarge the unit cell in order to contain six atoms. Therefore, the folded Brillouin zone is three times smaller and the $K_\pm$ points are mapped onto the Γ point, see Fig. 1. From the point of view of the lattice symmetries, this means that the two elementary translations $(t_{\vec{a}_1}, t_{\vec{a}_2})$ are factorized out of the translation group and added to the point group, which becomes $C''_{6v} = C_{6v} + t_{\vec{a}_1} \times C_{6v} + t_{\vec{a}_2} \times C_{6v}$ [20]. This allows us to treat all electronic excitations at the corners of the Brillouin zone on a same footing, including also possible inter-valley couplings. The Bloch wave function is given by a 6-component vector which represents the amplitude of the p_z orbitals at the 6 atoms of the unit cell. This vector can be reduced as $A_1 + B_2 + G'$. The 1-dimensional irreducible representations A_1 and B_2 correspond to the bonding and anti-bonding states at the original Γ point, whereas $\psi \sim G'$ corresponds to the Bloch states at the original Brillouin zone corners. Then, in order to construct the electronic Hamiltonian for quasiparticles around the $K_\pm$ points, we must consider the 16 hermitian operators acting in the 4-dimensional space defined by the Bloch wave functions ψ. These operators may be classified according to the transformation rules under the symmetry operations of C''_{6v}, taking into account the algebraical reduction

$$G' \times G' \sim A_1 + A_2 + B_1 + B_2 + E_1 + E_2 + E'_1 + E'_2 + G'.$$

In order to make the discussion more clear we introduce the basis $\psi = (\psi_{A+}, \psi_{B+}, \psi_{A-}, \psi_{B-})$, where each entry represents the projection of the Bloch wave function around each valley $K_\pm$ on sublattice A/B. Then,

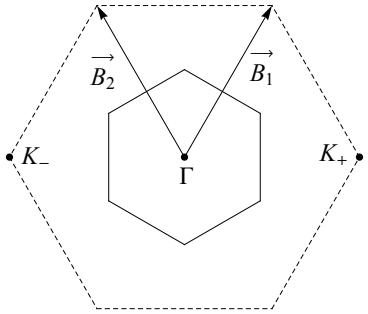

Figure 1: Graphene Brillouin zone corresponding to a real space unit cell with with 2 (dashed line) and 6 (solid line) atoms in the unit cell.

A_1	$\mathcal{I}$ (+)
A_2	$\tau_z \otimes \sigma_z$ (-)
B_1	τ_z (-)
B_2	σ_z (+)
E_1	$\begin{pmatrix} \tau_z \otimes \sigma_x \\ \sigma_y \end{pmatrix}$ (-)
E_2	$\begin{pmatrix} \sigma_x \\ \tau_z \otimes \sigma_y \end{pmatrix}$ (+)
E_1'	$\begin{pmatrix} \tau_x \otimes \sigma_x \\ \tau_y \otimes \sigma_x \end{pmatrix}$ (+)
E_2'	$\begin{pmatrix} -\tau_y \otimes \sigma_y \\ \tau_x \otimes \sigma_y \end{pmatrix}$ (-)
G'	$\begin{pmatrix} -\tau_y \\ \tau_x \otimes \sigma_z \\ -\tau_y \otimes \sigma_z \\ \tau_x \end{pmatrix}$ (+)

Table 1: Classification of the electronic operators according to the irreducible representations of C_{6v}''. The signs $\pm$ denote if the operator is even or odd under time reversal.

we introduce two inter-commutating Pauli algebras σ_i and τ_i associated to sublattice and valley degrees of freedom respectively. The 16 possible electronic operators are generated by considering the direct products of the elements of these algebras (and the identity). Their symmetry properties are summarized in Tab. 1. We must take into account also the time reversal operation, which is implemented by the antiunitary operator $\mathcal{T} = \tau_x \mathcal{K}$, where $\mathcal{K}$ represents complex conjugation.

The effective low energy Hamiltonian is constructed as an expansion in powers of the crystalline momentum $\vec{k} = (k_x, k_y) \sim E_1$ around $K_\pm$ points. Up to first order in $\vec{k}$ we have

$$H_0 = v_F \left(\tau_z \sigma_x k_x + \sigma_y k_y \right), \tag{1}$$

where v_F is the Fermi velocity. This Dirac Hamiltonian describes the approximately conical dispersion of π bands around $K_\pm$ points.

Phonon modes of graphene within the tripled unit cell can be also classified according to the irreducible representations of C_{6v}'' as shown in Tabs. 2 and 3. The modes belonging to the valley-diagonal irreducible representations correspond to the acoustic and optical modes at the original Γ point, according to which atoms of different sublattices oscillate in-phase or out-of-phase respectively. The modes belonging to the valley off-diagonal irreducible representations correspond to the modes at the $K_\pm$ points, in particular, real linear combinations of displacements at both valleys.

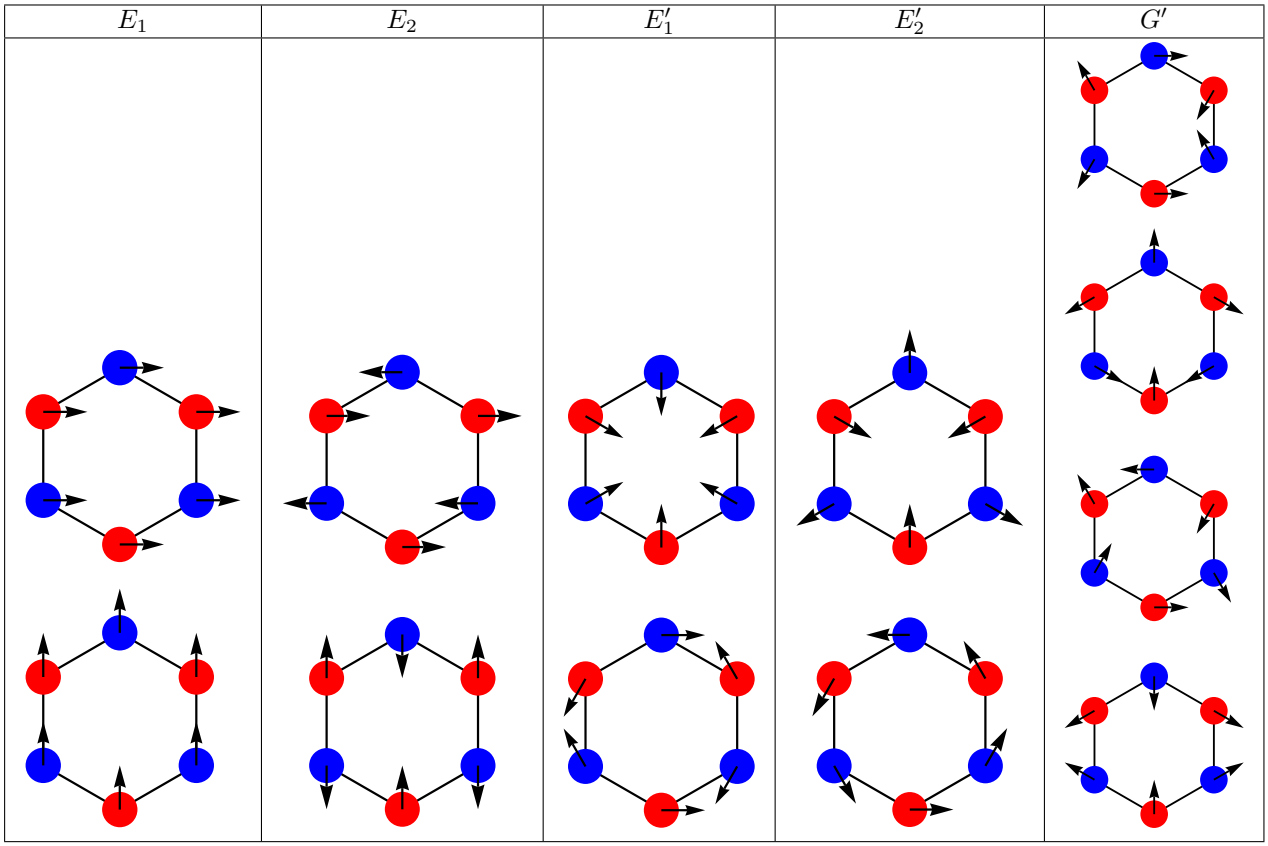

Table 2: Classification of in-plane phonon modes according to the irreducible representations of C_{6v}''.

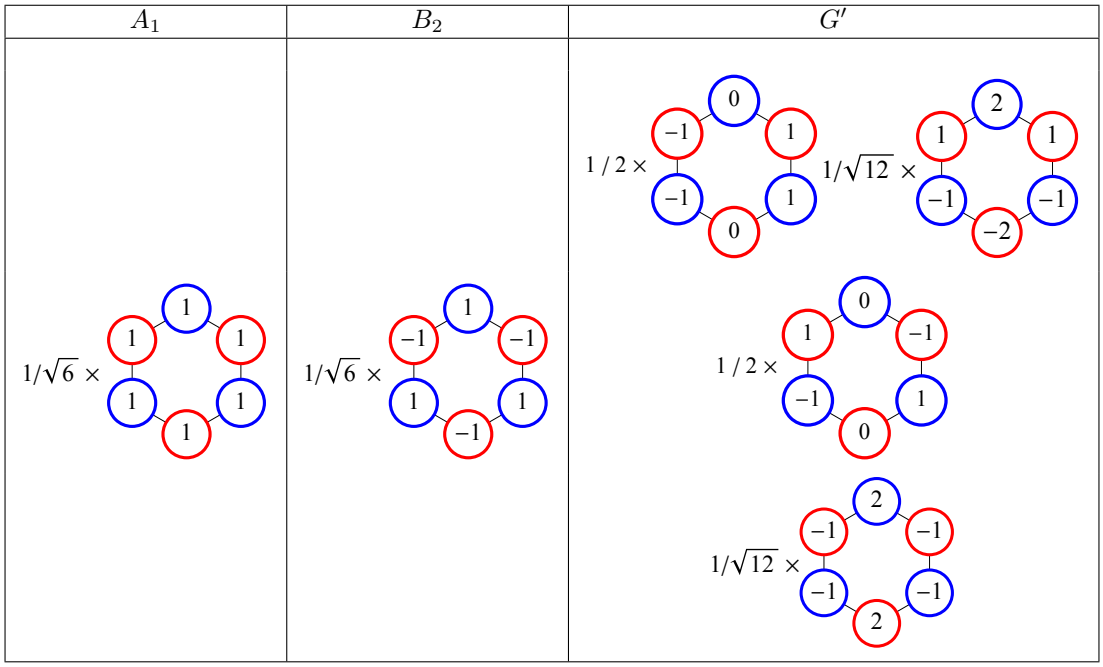

Table 3: Classification of flexural phonon modes according to the irreducible representations of C_{6v}''.

2.2. Theory of elasticity: graphene as a crystalline membrane

The dynamics of low energy vibration modes of graphene are governed by its elastic constants, and a long-wavelength description in terms of a theory in the continuum is valid since we focus on in-phase displacements only. The mechanics of solids, regarded as continuous media, is the subject of the theory of elasticity [21, 22], which can be constructed by purely geometrical means with the only constraint imposed by the symmetry of the underlying crystalline structure. The unit cells of the graphene crystal can be seen as points on a surface embedded in $\mathbb{R}^3$, each of them labelled by a 3D vector $\mathbf{r}$ (throughout the text we will denote 3D vectors with upright bold font and 2D vectors with an arrow). Therefore, the elastic energy associated with such an object can be split into two terms with a different geometrical and physical origin, which we write as

$$F_{\text{elastic}} = F_{\text{st}} + F_{\text{b}}, \tag{2}$$

where F_{st} is a stretching energy term that accounts for the energy cost due to relative changes in the distances and in-plane bond angles between atoms, and F_{b} is a bending energy term which penalizes deviations from a flat configuration.

The stretching energy depends on the first fundamental form, which is nothing but the pull-backed metric of the embedding space projected onto the surface,

$$g_{ij} = \partial_i \mathbf{r} \cdot \partial_j \mathbf{r}, \tag{3}$$

where ∂_i, $i = 1, 2$, is the derivative with respect to the internal coordinates which parametrize the surface. Note that this is a completely intrinsic quantity. In the Monge representation, carbon atoms at equilibrium, flat configurations are assumed to occupy positions labelled by $\mathbf{r}_0 = (x_0, y_0, 0)$, where x_0, y_0 correspond to the intrinsic coordinates that parametrize the surface. We consider deviations from these equilibrium positions given by a vector of displacements $\mathbf{r} = \mathbf{r}_0 + \mathbf{u}$. The displacements are fields which depend on the position of the unit cell, $\mathbf{u}(x_0, y_0)$. The first fundamental form is given by

$$g_{ij} = \delta_{ij} + 2u_{ij}, \tag{4}$$

where u_{ij} is the strain tensor. To the lowest order in the displacements, $\mathbf{u} = (u_x, u_y, h)$, this reads

$$u_{ij} = \frac{1}{2}\left(\partial_i u_j + \partial_j u_i + \partial_i h \partial_j h\right) \quad , \quad i, j = x, y. \tag{5}$$

Note that u_{ij} is quadratic to the lowest order in the out-of-plane displacements, h, as a manifestation of σ_h symmetry. We write the linear strain tensor only due to in-plane deformations as $u_{(i,j)} = \left(\partial_i u_j + \partial_j u_i\right)/2$ and the in-plane displacement as $\vec{u} = (u_x, u_y)$. The energy cost due to stretching can be written as a quadratic form in the strain tensor components [22, 21],

$$F_{\text{st}} = \frac{1}{2}\int d^2\vec{r}\, \mathcal{C}^{ijkl} u_{ij} u_{kl}, \tag{6}$$

where repeated indices are summed over and $\mathcal{C}^{ijkl}$ is the elastic constants tensor. Since $u_{ij} = u_{ji}$ by definition, in principle there are only 6 independent elastic constants in a 2D solid. Additionally, the elastic energy density must be invariant under the point group symmetries of the crystal. Note that Eq. (6) is not a complete invariant under coordinate transformations since for that the integration measure should be completed with the factor $\sqrt{\det g} \approx 1 + u_{ii}$. The description in the continuum of a 2D hexagonal crystal is essentially different from a fluid or any continuous media in the sense that the action must not be invariant under diffeomorphisms given that the atoms in the solid define a special coordinate system [23].

For isotropic media, only two elastic constants are independent. Since in that case the response of the solid must be independent of the direction, the only tensor available to construct higher order tensors is the Kronecker delta δ^{ij}. The only 4-rank tensors formed by δ^{ij} satisfying the symmetries of $\mathcal{C}^{ijkl}$ are $\delta^{ij}\delta^{kl}$ and $\delta^{ik}\delta^{jl} + \delta^{il}\delta^{jk}$, therefore

$$\mathcal{C}^{ijkl} = \lambda \delta^{ij}\delta^{kl} + \mu\left(\delta^{ik}\delta^{jl} + \delta^{il}\delta^{jk}\right), \tag{7}$$

where λ, μ are the Lamé coefficients. In 2D, this is precisely the case of hexagonal crystals. In the particular case of graphene, the 3 independent components of u_{ij} transform according to

$$\begin{aligned} u_{xx} + u_{yy} &\sim A_1, \\ \begin{pmatrix} u_{xx} - u_{yy} \\ -2u_{xy} \end{pmatrix} &\sim E_2. \end{aligned} \tag{8}$$

Then, among the six independent combinations of the form $u_{ij}u_{kl}$, only two of them form scalars belonging to A_1 irreducible representations. This is inferred from the algebraical reductions

$$\begin{aligned} A_1 \times A_1 &\sim A_1, \\ A_1 \times E_2 &\sim E_2, \\ E_2 \times E_2 &\sim A_1 + A_2 + E_2. \end{aligned} \tag{9}$$

Therefore, for crystals with C_{6v} there are only 2 independent elastic constants corresponding to the Lamé coefficients. Thus, the stretching energy for graphene has the explicit form

$$F_{\rm st} = \frac{1}{2}\int d^2\vec{r}\left(\lambda u_{ii}^2 + 2\mu u_{ij}u_{ij}\right). \tag{10}$$

Notice that inclusion of the quadratic term $\partial_i h \partial_j h$ in u_{ij} makes the theory defined by the above equation an interacting theory. For free membranes this has important consequences as will be seen in Section 3. If we discard these anharmonic terms in Eq. (10), we obtain two in-plane acoustic phonons with linear dispersion relations. At low momentum these modes can be classified as longitudinal and transverse, and the respective dispersion relations are given by

$$\omega_{\vec{q}}^{L} = \sqrt{\frac{\lambda + 2\mu}{\rho}}\,|\vec{q}| = v_L\,|\vec{q}|\,, \tag{11}$$

$$\omega_{\vec{q}}^{T} = \sqrt{\frac{\mu}{\rho}}\,|\vec{q}| = v_T\,|\vec{q}|\,, \tag{12}$$

where $\rho \approx 7.6 \times 10^{-7}$ kg/m^2 is the graphene's mass density and $v_{L/T}$ is the longitudinal/transverse sound velocity. Typical values for the elastic constants of graphene are $\mu \approx 3\lambda \approx 9$ eV Å^{-2} [24, 25, 26], leading to $v_{L/T} \sim 10^4$ m/s.

Information about the bending of the membrane, or in other words, its embedding in 3 dimensional space, such as changes from point to point of the normal vector to the surface, $\hat{\mathbf{n}} = \partial_1\mathbf{r} \times \partial_2\mathbf{r}/|\partial_1\mathbf{r} \times \partial_2\mathbf{r}|$, are described by the second fundamental form,

$$\mathcal{F}_{ij} = \hat{\mathbf{n}} \cdot \partial_i\partial_j\mathbf{r}. \tag{13}$$

To lowest order in the displacement fields, and assuming smooth out-of-plane displacements, the normal vector at each point of the membrane is given by $\hat{\mathbf{n}} \approx (-\partial_x h, -\partial_y h, 1)$. In this approximation the second fundamental form is given by

$$\mathcal{F}_{ij} \approx \partial_i\partial_j h. \tag{14}$$

Two scalars may be constructed from the second fundamental form: the mean extrinsic curvature, $\mathcal{F}_{ii}$, and the intrinsic or Gaussian curvature $\det\mathcal{F}$, but note that the latter is a purely topological term which does not affect the equations of motion. The bending energy is then a quadratic form of the former [4],

$$F_{\rm b} = \frac{\kappa}{2}\int d^2\vec{r}\,(\mathcal{F}_{ii})^2 \approx \frac{\kappa}{2}\int d^2\vec{r}\left(\nabla^2 h\right)^2. \tag{15}$$

Here $\kappa \approx 1$ eV [26] is the (bare) bending rigidity. The dispersion relation of out-of-plane or flexural acoustic phonon modes of a free membrane is then quadratic,

$$\omega_{\vec{q}}^{F} = \sqrt{\frac{\kappa}{\rho}} \left|\vec{q}\right|^{2} . \tag{16}$$

However, a rotational symmetry breaking tends to linearize the dispersion relation, for instance, due to the presence of strain. On the other hand, these modes are strongly suppressed in supported samples, where part of the spectral weight is transferred to a hybrid state with the surface Rayleigh mode of the substrate [27].

Putting together the two contributions to the elastic energy of the membrane we obtain

$$F_{\text{elastic}} = \frac{1}{2} \int d^{2}\vec{r} \left(\kappa \left(\nabla^{2} h \right)^{2} + \lambda u_{ii}^{2} + 2\mu u_{ij} u_{ij} \right) . \tag{17}$$

This equation has the same functional form as the usual von Kármán free energy for thin plates [21]. However, two differences must be pointed out. First, for a thin plate the bending rigidity, κ, is related to the elastic constants λ and μ and the thickness of the plate. The same is not true for atomically thin membranes, for which it is not possible to define a thickness. Therefore, κ is an independent parameter of the model for a membrane. Secondly, Eq. (17) corresponds to the potential energy of a Hamiltonian, not a free energy. The difference becomes important when thermal fluctuations, discussed in Section 3.1.1, are taken into account. For κ sufficiently large, as in a plate, anharmonic interactions are suppressed and the free energy is given by the same expression as the potential energy. If κ is small, the case of a membrane, then anharmonic interactions become dominant and the free energy can have a very different form than the potential energy.

2.3. Electron-phonon coupling

The symmetry approach has been widely applied to the problem of strained graphene (*e.g.* [28],[29],[30]). With the help of group analysis it is possible to construct a systematic derivative expansion of the low energy effective Hamiltonian of graphene in the presence of non-uniform elastic deformations. For the sake of simplicity we will consider only the case of spinless graphene. The spinful case and the role of strain in spin relaxation are discussed in Refs. [31, 32]. We restrict ourselves to linear order in the electron momentum k (first derivatives), so that the effective Hamiltonian will be a function of the strain tensor u_{ij} and its derivatives, and the electron fields ψ and $\psi^{\dagger}$. Beyond the Dirac approximation the procedure can be straightforwardly extended to higher order in k. In this way, the systematic expansion is characterized by two integers, (n_q, n_k), the order of the derivatives of the strain tensor and the electron fields respectively.

Since we are interested in long wavelength deformations that are not able to couple different valleys, in what follows we will construct the possible interactions allowed by symmetry based on the little group approach [33]. As explained in Ref. [34] it is sufficient to consider terms invariant under C_{3v}, the little group of one of the inequivalent Dirac points, together with the combined operation $\mathcal{T}C_2$, where C_2 is a $\pi-$rotation around the z axis. Once the degrees of freedom are established and the symmetries of the system are determined, all we need to know is the way they transform under the relevant group operations and how these can be decomposed as a sum of irreducible representations. Using standard group character operation [33] it is possible to determine how many and which are the terms allowed by symmetry at a given order (n_q, n_k). As explained in Ref. [34], up to first order in derivatives, $n_q + n_k \leq 1$, there are only six terms involving the strain tensor. These six terms corresponding to K_+ are listed in Tab. 4 together with their physical significance and the corresponding relative sign at the inequivalent Dirac Point K_-.

We can now write the most general Hamiltonian in the presence of non-uniform strain, up to first derivatives of the strain tensor u_{ij} (5), and up to first order in the derivatives of the electron fields ψ and $\psi^{\dagger}$. It is important to note that u_{ij} is a function of two independent variables u_i and h. In order to keep the necessary number of independent coupling constants, we will introduce for each H term, function only of u_{ij}, an extra term $\tilde{H}$, function only of h;

H_i	(n_q, n_k)	Interaction term	Physical interpretation	K_-
H_1	(0,0)	$(u_{xx}+u_{yy})\mathbb{1}$	Position-dependent electrostatic pseudopotential	+
H_2	(0,0)	$(u_{xx}-u_{yy})\sigma_x - 2u_{xy}\sigma_y$	Dirac cone shift or U(1) pseudogauge field $(\mathcal{A}_x^{el}, \mathcal{A}_y^{el})$	−
H_3	(0,1)	$\left[(u_{xx}-u_{yy})k_x - 2u_{xy}k_y\right]\mathbb{1}$	Dirac cone tilt	−
H_4	(0,1)	$(u_{xx}+u_{yy})(\sigma_x k_x + \sigma_y k_y)$	Isotropic position-dependent Fermi velocity	+
H_5	(0,1)	$u_{ij}\sigma_i k_j \;\;;\;\; i,j = x,y$	Anisotropic position-dependent Fermi velocity	+
H_6	(1,0)	$\left[\partial_y(u_{xx}-u_{yy}) + 2\partial_x u_{xy}\right]\sigma_z$	Gap opening by non-uniform strain	−

Table 4: Effective low energy terms in the Hamiltonian for the electron–strain interactions allowed by symmetry. The role of the gamma matrices as projectors into irreducible representations is clarified in [35].

$$H = H_0 + \sum_{i=1}^{6} g_i H_i + \sum_{i=1}^{6} \tilde{g}_i \tilde{H}_i. \tag{18}$$

The first term is the standard Dirac contribution $H_0 = v_F(\pm\sigma_x k_x + \sigma_y k_y)$, and the terms H_i are given in Tab. 4, and described below. The terms $\tilde{H}_i$ are obtained from those in Tab. 4 through the substitution $u_{ij} \to \partial_i h \partial_j h$. Of course, the symmetry machinery can give us all the possible terms up to a given order in derivatives, but the coupling constants remain undetermined and have to be fixed with a concrete microscopic model.

The second-quantized Hamiltonian operator is given by $\mathcal{H} = \int d^2\vec{r}\,\psi^\dagger H \psi$, where the symmetric convention for the derivatives acting on the electron fields is assumed, i.e., $\psi^\dagger k_i \psi \to -i/2(\psi^\dagger \overleftrightarrow{\partial_i} \psi) \equiv -i/2(\psi^\dagger \partial_i \psi - \partial_i \psi^\dagger \psi)$. In more general terms, ∂_j acts only on the electron fields. The construction of second quantized hermitian operators becomes simpler using the symmetric derivative convention. Note that Tab. 4 gives the orders of the derivatives when terms are written with the symmetric convention.

- $H_1 = (u_{xx}+u_{yy})\mathbb{1}$: This term has been already described in Ref. [36]. It is a scalar potential

$$V_s(\vec{r}) = g_1\left(u_{xx}(\vec{r}) + u_{yy}(\vec{r})\right). \tag{19}$$

  The coupling g_1 is called deformation potential and its strength has been estimated to be of the order 4 eV for single layer graphene [37], although other works [38, 39] argue that screening leads to a strongly suppressed $g_1 \approx 0$. Its physical consequences have been explored in Ref. [40] and will be discussed in Section 4.

- $H_2 = (u_{xx}-u_{yy})\sigma_x - 2u_{xy}\sigma_y$: This term represents a shift in momentum space of the Dirac cone. It corresponds to the well known $U(1)$ elastic pseudo-gauge field

$$\vec{\mathcal{A}}^{el}(\vec{r}) = \pm g_2\left(u_{xx}(\vec{r}) - u_{yy}(\vec{r}), -2u_{xy}(\vec{r})\right). \tag{20}$$

  In the tight binding formalism $g_2 \sim \beta = -\partial(\log t)/\partial(\log a)$, where t is the hopping integral between nearest neighbours and a is the lattice constant. It is at the basis of most of the results in the literature related to strain engineering and there are experimental realizations [8]. It has also been used to explain data in artificial graphene [41].

- $H_3 = \left[(u_{xx}-u_{yy})k_x - 2u_{xy}k_y\right]\mathbb{1}$: Dirac cone tilt. This term appears naturally in the description of the two dimensional organic superconductors [42] which are described by anisotropic Dirac fermions. It also arises when applying uniaxial strain in the zigzag direction, a situation that has been discussed at length in the literature [43, 44, 45, 37]. A novel physical manifestation of the Dirac cone tilt has been described recently in [46].

- $H_4 = (u_{xx}+u_{yy})(\sigma_x k_x + \sigma_y k_y)$: Isotropic position-dependent Fermi velocity [47].

- $H_5 = u_{ij}\sigma_i k_j \;\; ; \;\; i,j = x,y$: Anisotropic position-dependent Fermi velocity [47]. This term, together with H_4, has been predicted to arise within the geometric modelling of graphene based on techniques of quantum field theory in curved space [48]. It was later obtained in a tight binding model by expanding the low energy Hamiltonian to linear order in $\vec{k}$ and u_{ij} [47, 49]. Since the Fermi velocity is arguably the most important parameter in graphene physics, this term affects all the experiments and will induce extra spatial anisotropies in strained samples near the Dirac point [50, 51, 52, 53, 54, 55]. This term will be described in detail in Section 2.4.
- $H_6 = \left[\partial_y(u_{xx} - u_{yy}) + 2\partial_x u_{xy}\right]\sigma_z$: This is a very interesting term that suggests a new gap-opening mechanism [34]. It can be seen as the Zeeman coupling of pseudospin to the associated pseudomagnetic field $B_z = \partial_x \mathcal{A}_y^{el} - \partial_y \mathcal{A}_x^{el}$ [56]. The magnitude of this gap has been estimated to be 7 meV [34] .

It is important to notice that because of the symmetric convention, some non-spurious terms seem to be missing, as it is the case of the vector field Γ_i [47]. This is just an artefact of the symmetric convention and all the relevant terms will appear in the equation of motion. In the case of Γ_i, its presence becomes evident by integrating by parts H_4 and H_5.

2.3.1. Experimental confirmation of the elastic pseudomagnetic fields

The term H_2 representing fictitious magnetic fields coupling with opposite sign to the two valleys was the first to be identified in the early publications and its physical consequences were discussed at length in the review [8]. The theoretical suggestion that Landau levels can form associated to strain in graphene was done in [57, 58]. The simple observation that applying a trigonal strain gives rise to uniform pseudomagnetic fields in a region of the sample, gave birth to real strain engineering. The theoretical proposal was soon followed by the experimental confirmation. A Landau level structure was observed in a STM experiment on graphene samples with triangular nanobubbles in [59]. Fields of up to 300 Tesla were estimated in the central region of the bubbles. This pioneer experiment was followed by many reports of elastic Landau levels in graphene samples [60, 61, 62], cold atoms [63], and artificial graphene [64]. Elastic gauge fields have also been described in bilayer graphene [65], other 2D semiconductors [66] and lately in the recently discovered three dimensional Weyl semimetals [67]. The effects of the elastic pseudomagnetic fields on various transport coefficients have been analysed in numerous publications [68, 69, 70] and will be described in more detail in Section 4.

2.3.2. Experiments probing local variations in v_F

There are several ways to measure the Fermi velocity experimentally. In this section, we concentrate on measurements that are local and can thus probe the spatial variation of the Fermi velocity predicted by Eq. (26). The optimal experimental technique to do this is scanning tunnelling spectroscopy (STS), which is sensitive to the local density of states (LDOS)[1]. Since the LDOS depends on v_F as $\rho(E) = 2|E|/\pi v_F^2$, if the strain variation is smooth one may replace $v_F \to v_F(x)$ and fit the slope of the measured LDOS to this expression to obtain a local measurement of v_F.

Two recent experiments have reported evidence of a spatially varying v_F using this method. The first was performed on graphene grown on a Rh foil [71], which develops quasiperiodic ripples. Local variations of v_F on different parts of the ripples were reported with a rather wide distribution of values, consistent with the strain induced by the ripples. In the second, graphene was grown on BN [72], where strained ridges were randomly formed. In a more quantitative comparison, the LDOS measured in these ridges reveals a spatially dependent v_F which is shown to be correlated with the height of the ridges. This represents convincing evidence that v_F fluctuations indeed originate from strain.

An alternative way to measure v_F locally is with Landau Level spectroscopy. In the presence of a magnetic field, the LDOS is rearranged into a series of well defined peaks at the Landau Level energies, given by $E_n = \mathrm{sgn}(n) v_F \sqrt{2e\hbar B n}$. A measurement of v_F can thus be obtained by fitting this expression as well. This type of experiment has been performed with randomly strained graphene as grown on SiO_2, and the measurement indeed reveals a local variation of v_F of 5-10 % [73].

[1] See section 5 for a discussion of how superlattices may also induce local variations of the LDOS that is seen by STM.

2.4. Quantum field theory in curved spaces

One of the features that makes graphene unique is the way the electronic degrees of freedom couple to structural deformations of the lattice, and how this allows to modify its electronic properties in interesting ways. In the previous section, we have shown how the deformation of the lattice is described in terms of a strain tensor u_{ij}, and what are the possible strain couplings allowed by the discrete symmetry of the lattice in the low energy Dirac Hamiltonian. In this section, we discuss a complementary approach to the study of the effects of deformations which provides insightful connections to the geometry of the problem. This approach originates in the idea that, since local distances in the strained lattice can be described in terms of a metric (the first fundamental form introduced in (3)), a natural model to describe the coupling of electrons to the deformation should be the Dirac equation in curved space. The formalism in full glory is taken from quantum field theory (QFT) in curved space [5] and was explained in detail in the review article [8]. In this section we describe the modern uses of the metric (unrelated to strain deformations) to generate response functions in condensed matter theory.

While this approach is phenomenological rather than microscopic in nature, it offers an interesting geometrical interpretation of the different couplings, and it is a well understood formalism. The Dirac equation in curved space is completely determined by the metric $g_{ij} = \delta_{ij} + 2u_{ij}$ and takes the form

$$\mathcal{H} = -i \int d^2\vec{x}\sqrt{g}\bar{\psi}\gamma^a e_a^i(\partial_i + \Omega_i)\psi, \tag{21}$$

where $a = 1, 2$ and $i = 1, 2$ run over the space dimensions, $\bar{\psi} = \psi^\dagger\gamma^0$, $\gamma^0\gamma^i = \sigma^i$ are the Pauli matrices, e_a^i are the tetrads, Ω_i is the spin connection and $\sqrt{g}$ is the volume factor. These three geometric quantities can be obtained from g_{ij}, see Ref. [47] for explicit expressions. Many authors have studied this model in connection with different problems, which include the spectrum of fullerenes [74], the modelling of disclinations[75, 76], graphene wormholes [77] proposals of metrics to generate in optical lattices [78], the holography conjecture [79] and the Unruh effect [80, 81, 82]. This model has also been applied to the study of the optical conductivity in graphene [83, 84], to the scattering by smooth deformations in topological insulator surfaces[85, 86], and to study the Quantum Hall effect [87].

To be able to compare this approach with the standard tight-binding results, one proceeds by expanding Eq. 21 to first order in u_{ij} for small strains, which can be written as

$$H = -i[v_{ij}(x)\sigma_i\partial_j + \sigma_i\Gamma_i], \tag{22}$$

where

$$v_{ij} = v_F(\delta_{ij} + \delta_{ij}u_{kk} - u_{ij}) \tag{23}$$

$$\Gamma_i = \frac{1}{2}\partial_j v_{ij} \tag{24}$$

where v_F is the Dirac fermion velocity in the absence of distortion. The most interesting feature of this model is the presence of the matrix v_{ij}, which may be interpreted as a tensorial, spatially dependent Fermi velocity. This interpretation was first put forward in Ref. [48], where it was shown that it can be responsible for local modulations of the density of states (DOS) that are correlated with strain. The model also displays a spin connection, which can be responsible for pseudo-spin precession, for example. It can be seen that the two terms in the expression for the Fermi velocity are consistent with those allowed by the discrete symmetry of the lattice, terms H_4 and H_5 in Section 2.3.

The model just presented has many nice features and has proven useful, but it has the drawback that it has not been derived from a microscopic Hamiltonian. The simplest microscopic derivation of the coupling of electrons to strain can be done with a tight-binding model, assuming that the hopping parameters change locally with distance, $t_n = t(1 - g_2|\Delta u_n|)$, where g_2 is the dimensionless electron phonon coupling defined in the previous section. This model has been used extensively across the graphene literature to show that, to lowest order, strain couples as a gauge field of the form H_2 in the low energy Hamiltonian. The space-dependent Fermi velocity is also present in this model, when the expansion is taken to first order both in

strain and in momentum [47], which gives a Hamiltonian

$$H_{TB} = -i[v_{ij}^{TB}(x)\sigma_i\partial_j + v_F\sigma_i\Gamma_i + iv_F\sigma_i\mathcal{A}_i^{el}], \tag{25}$$

where the field $\mathcal{A}_i^{el}$ is the one given in the Hamiltonian H_2 of Section 2.3, and v_{ij}^{TB} is the Fermi velocity tensor obtained from tight-binding, which is

$$v_{ij}^{TB} = v_F[\delta_{ij} - \frac{g_2}{4}(2u_{ij} + \delta_{ij}u_{kk})], \tag{26}$$

with $v_F = 3/2ta$. Again, the two terms found from the microscopic approach are consistent with those found in the symmetry analysis, H_4 and H_5. One may observe, however, that the coefficients obtained for these terms in tight-binding are not the same as those in the curved space model. The physical predictions of these two models are however qualitatively similar. The fact that the tight binding model gives the functional form of the Fermi velocity tensor that is different from the one postulated by curved space model was recently discussed in Ref. [88].

Analytical expressions for the dependence of the Fermi velocity on strain from which the coefficients of the terms H_4 and H_5 can be extracted were also reported in Refs. [89, 54]. The anisotropy in the Fermi velocity was demonstrated numerically in tight-binding studies [90, 91] and in *ab initio* calculations [37]. The corrections to the Fermi velocity tensor to second order in strain were computed in Ref. [92]. The approach of Refs. [93, 94] based on discrete differential geometry can also be used to compute higher order corrections. The tight binding model with space-dependent velocity has also been used to study bound states in strain superlattices [95] and to study the modulation of persistent currents in graphene rings[96]. The possibility of tuning the strain to get a given velocity profile has been suggested in [97].

It is worth emphasizing that the Fermi velocity tensor, as well as the other terms obtained from the symmetry analysis, was computed by expanding the Hamiltonian around the high symmetry point K. Only in this way one can classify the different terms under the symmetry of the little group at K. It has recently been argued that, in the case of constant strain, since the Dirac point is shifted due to the constant vector potential, the Fermi velocity tensor has a different form when the expansion is performed around the shifted Dirac point [93, 94].

There are several works that have addressed the modelling of a spatially dependent Fermi velocity with a different phenomenological model, which amounts to the direct replacement of v_F by a scalar function $v(x)$ in the Hamiltonian [98, 99, 100, 101, 102]. This model is equivalent to considering just the isotropic coupling to the strain H_4 with a scalar function $v(x) = v_F u_{kk}$.

The motivation to study the case when the only term affecting the Fermi velocity is the isotropic one is to analyse how to control wave propagation by velocity changes in analogy with the modulation of the refraction index in optics. These works studied the propagation of Dirac electrons in different scalar velocity profiles, concluding that the transmission through a velocity barrier has a strong dependence on the incidence angle, but is always equal to one at normal incidence. When v_F in the barrier is larger than outside it, there is a critical angle above which no transmission is possible, in analogy with the Brewster angle.

2.4.1. Uses of the metric as an auxiliary field to generate response coefficients

We here review some uses of the metric and the spin connection as auxiliary tools to derive exotic transport properties of materials.

In an effective action framework transport coefficients can be computed from the partition function of a system by coupling appropriate source terms to the operators whose response we want to analyse. The best example is that of the electromagnetic currents obtained by coupling a background electromagnetic potential (even in the absence of actual fields). Then Kubo formulae can be used to compute the coefficients of the current-current correlation functions.

Thermal transport is one of the most difficult aspects to address in materials. In a seminal work J. M. Luttinger [103] proposed the use of the metric as an auxiliary tool to analyse thermoelectric transport coefficients in solids. In the remarkable footnote 7 he writes: *In fact, if the gravitational field didn't exist, one could invent one for the purpose of this paper.* The aim was to derive an expression for the thermal conductivity similar to the Kubo formula of the electrical conductivity. The main difficulty with thermal transport

coefficients is that there is no Hamiltonian which describes a thermal gradient since the temperature is a statistical property of the system. Inspired by the relation between the metric and the energy-momentum or stress tensor ($T^{\mu\nu}$, with Greek indices running over space-time coordinates) that holds in general relativity:

$$T^{\mu\nu} = \frac{2}{\sqrt{-g}} \frac{\delta \mathcal{S}}{\delta g_{\mu\nu}}. \tag{27}$$

($\mathcal{S}$ is the action of the matter) he proposed to couple the electron system to an auxiliary field (an inhomogeneous gravitational field) which causes energy or heat currents to flow. The interaction term was $S_{int} = \int h(r)\Phi(r,t)$ where $h(r)$ is the Hamiltonian density of the matter system and $\Phi(r,t)$ is a "gravitational potential". A varying Φ will give rise to a varying energy density which in turn will correspond to a varying temperature. No matter how ambiguous the original work can look today, it paved the way to very important recent developments in condensed matter. An attempt to put this work on firmer grounds by deriving expressions similar to (27) for a non-relativistic system has appeared recently in [104]. The proposed formalism involves the Riemann Cartan geometry, which, in addition to curvature, includes torsion in the background geometry (for a "primer" on torsion in condensed matter applications see [105]). The viscosity, another important transport coefficient of the electronic fluid, also involves the metric in its definition as will be discussed in the next subsection.

2.5. Topological aspects and time–dependent deformations

Topological phases of matter are a new paradigm in condensed matter physics. These phases add to the standard classification in terms of local order parameters and broken symmetries new quantum numbers associated to topological invariants [106, 107]. Since the early developments of the field and due to its peculiar properties, the honeycomb lattice has been used as the ideal model to demonstrate topological properties. The pioneer works proposing this lattice as a "condensed matter simulation of a three-dimensional anomaly" [108, 109], together with the analysis of the spin orbit in graphene done in Refs. [110, 111] opened the modern field of topological insulators. Most of the new topological materials (graphene, topological insulators and superconductors, Weyl semimetals [112, 113]) share the property that their low energy electronic properties are described by Dirac fermions [114, 115] in one, two or three spacial dimensions enlarging and widening the bridge between high energy and condensed matter in this century.

At a zeroth order approach to topological aspects, Dirac points in (2+1) dimensions are usually protected by a winding number: the Berry phase acquired by the spinor wave function when circling around a Dirac point in momentum space. Time reversal symmetry implies that Dirac points in crystals arise in pairs with opposite winding numbers [116]. Lattice deformations move the Dirac points that eventually can merge giving rise to interesting topological phases. The existence and merging of Dirac points in crystals was studied in the early work [117] and a very complete analysis of the issue has appeared in the recent review [115].

In this section we review the late developments on the influence of lattice deformations on the topological properties of graphene and related materials. The topological phases induced by a combination of strain and interaction will be discussed in Section 4.5.1.

2.5.1. Hall viscosity

In a similar way as done by Luttinger with the heat transport, the metric is being used more recently to analyse properties such as the Hall viscosity [118] in topological insulators and in quantum Hall fluids [119, 120, 121, 122]. The analogue of friction in fluid dynamics is provided by viscosity, which causes dissipation of the energy (momentum) flow. In elasticity theory we can define (see Section 2.2)

$$T^{ij} = \mathcal{C}^{ijkl} u_{kl} + \eta^{ijkl} \dot{u}_{kl}, \tag{28}$$

where u_{ij} is the strain tensor, and $\mathcal{C}^{ijkl}$ and η^{ijkl} are the elastic and viscosity coefficients. Viscosity can then be defined as the response of the system to a time-varying strain. In general, this viscosity tensor possesses both symmetric and antisymmetric components under the permutation of pairs of indices. While

the symmetric part is generally associated to dissipation and vanishes at zero temperature, the antisymmetric part arises when time reversal symmetry is broken and was first described in the quantum Hall fluid [118]. A stress-stress form for the response function yields a Kubo formula for the viscosity.

The Hall viscosity can be derived by coupling the system to an external metric g_{ij}. Under a small time-dependent shape deformation which preserves the volume: $g_{ij} = \delta_{ij} + \delta g_{ij}(t)$, the stress tensor is

$$T^{ij} = P\delta^{ij} - \frac{1}{2}\eta^{ijkl}\partial_t \delta g_{ij}, \tag{29}$$

where P is the pressure and the tensor $\eta_{ijkl} = -\eta_{klij}$ is the Hall viscosity. This transport coefficient is particularly interesting in the case of fractional quantum Hall fluids (FQHF). Unlike the Hall conductivity which is quantized and dimensionless, the Hall viscosity has units of $1/L^2$. In a quantum Hall system the Hall viscosity, defined as the response of the electronic fluid to geometric shear distortions, is proportional to the density of intrinsic angular momentum: $\eta_A = 1/2sn$ (n is the particle number density and s is the average spin per particle, so sn is the area density of intrinsic angular momentum). Computation of the Hall viscosity in topological matter and its relation to the total angular momentum is one of the most active areas of research nowadays involving all the geometrical tools concerning the study of QFT in curved background fields including torsion [119, 122, 123]. In a very recent publication [124], Ward identities have been used to relate Hall viscosities, Hall conductivities and the angular momentum.

In the early publication [125] it was recognized that Hall fluids couple also to the curvature of the background surface, a fact that manifests itself by the presence of a shift in the relation between the number of electrons N_e, and the number of magnetic flux quanta N_ϕ going through the manifold. In a flat system they are related by $\nu N_\phi = N_e$, where ν is the filling factor. In a compact curved manifold such as a sphere there is a shift $\mathcal{S}$ such that:

$$N_\phi = \nu^{-1} N_e - \mathcal{S}. \tag{30}$$

It was observed that the shift on a sphere and in a torus were different (it was zero in a torus) what led the authors to conjecture that the Hall fluid did couple to the spin connection vector form defined as $\Omega_\mu = \omega_\mu^{ab}\varepsilon_{ab}$. Coupling this vector as a source in an effective action formalism allows to obtain the shift as the coefficient of a mixed Chern-Simons electromagnetic–gravitational term of the form $S_{WZ} \sim \varepsilon^{ijk}\omega_i \nabla_j a_k$, known as the Wen–Zee term. The effective Chern Simons action describing the geometrical factors in Hall fluids has been put in firmer grounds recently in [123].

The Wen–Zee action can also be seen as an example of anomaly related transport, a field that is also investigated very actively these days in both condensed matter and high energies in the context of the quark-gluon plasma [126]. The most commonly cited example of the new non-dissipative transport phenomena occurring in the quark–gluon plasma is the chiral magnetic effect [127] that refers to the generation of an electric current parallel to a magnetic field whenever an imbalance between the number of right and left-handed fermions is present. Another interesting example is the axial magnetic effect (AME) associated with the generation of an energy current parallel to an axial magnetic field, i. e. a magnetic field coupling with opposite signs to right and left handed fermions. These new transport phenomena are specially relevant to the (3+1) dimensional Dirac materials, particularly in Weyl semimetals. The axial magnetic effect in Weyl semimetals as a fingerprint of the gravitational anomaly has been proposed in [128]. Of particular interest is the part associated to the anomalous transport coefficients generated by the gravitational anomaly [129, 130, 131].

2.5.2. Transverse conductivity from time-dependent deformations

The valley degree of freedom in graphene has been proposed as a novel ingredient to encode information, its control and manipulation led to the concept of valleytronics [132]. As mentioned in Section 2.3, lattice deformations and defects couple to the electronic current in graphene in the form of vector fields that couple with opposite signs in the two valleys. This fact has given rise to several interesting proposals related to valley physics in strained graphene [133]. It was shown in [50] that the combination of real and fictitious magnetic field induces a valley asymmetry in the Landau level structure.

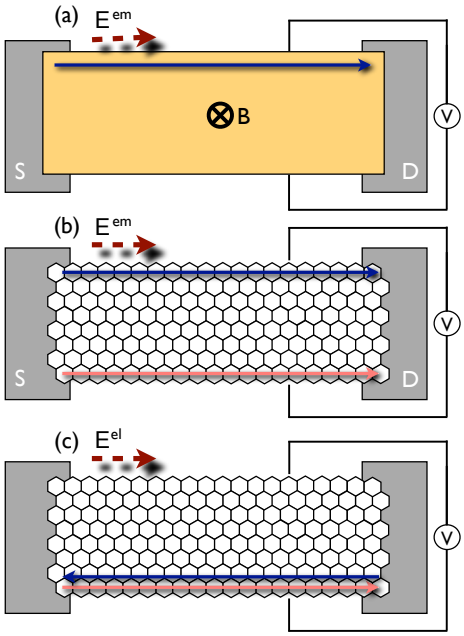

Figure 2: (colour online) Comparison between the Hall effect (upper), the valley Hall effect (middle), and the effect proposed in the text (lower) following the scheme of the original implementation of the experiment first proposed by Hall. The arrows indicate the flow of valley polarized electrons under the action of an external electric field or voltage (upper and middle) and of a time dependent strain (lower part). In the later case the total current is $< J^i_K + J^i_{K'} > \sim E^{el}_j$.(Fig. adapted from ref. [135]).

Following Eq. (20), a time-dependent deformation gives rise to a "synthetic electric field" $E^{el}_i = \partial_0 \mathcal{A}^{el}_i$ that also couples with opposite signs to the two Fermi points. The observable consequences of the "synthetic electric field" in graphene were described in the early publication [134]. It was recognized that, due to the opposite signs of the coupling at the two valleys, this synthetic electric field can drive charge–neutral valley currents in carbon nanotubes and graphene that are not subjected to screening and hence can have a stronger influence on the electronics than the deformation potential.

An interesting topological response due to the interplay of electromagnetic and a time-dependent elastic vector field was studied in [135]. The total Chern number - and hence the Hall conductivity - of a time-reversal invariant system is zero. The topological signals in these systems, such as the spin Hall effect, have associated dissipationless transverse currents involving degrees of freedom – spin, valley, layer [136] other than the electric charge. It was shown in [135] that the interplay of electromagnetic and elastic vector fields can give rise to a transverse electric current. The argument goes as follows: In the presence of an external electromagnetic and elastic field the gapped graphene Hamiltonian reads:

$$\mathcal{H} = \sum_\tau \psi^\dagger_{\tau,\vec{k}} \left(\tau\sigma_x k_x + \sigma_y k_y\right) \psi_{\tau,\vec{k}} \quad - \quad \sum_\tau [\psi^\dagger_{\tau,\vec{k}} \tau\sigma_x \left(eA^{em}_x + \tau g_2 \mathcal{A}^{el}_x\right) \psi_{\tau,\vec{k}}] - \\ - \quad \sum_\tau [\psi^\dagger_{\tau,\vec{k}} \sigma_y \left(eA^{em}_y + \tau g_2 \mathcal{A}^{el}_y\right) \psi_{\tau,\vec{k}} + m\psi^\dagger_{\tau,\vec{k}} \sigma_3 \psi_{\tau,\vec{k}}], \qquad (31)$$

where $\tau = \pm 1$ denotes the valley degree of freedom, e is the electric charge, $\vec{A}^{em}$ and $\vec{\mathcal{A}}^{el}$ stand for the electromagnetic and the elastic vector fields respectively, and the parameter $g_2 > 0$ encodes the strength of the elastic coupling. The coefficient τ in front of the coupling of the electronic current to the elastic vector field marks the difference with the electromagnetic gauge field that couples with the same sign to the two valleys. In the presence of a time-reversal preserving mass m (having the same sign in both valleys) as the one considered in (31) there is a non zero Chern number which takes opposite values at the two Fermi points

$C_{\vec{K}} = -C_{\vec{K}'} = \mathrm{sgn}(m)/2$. In the absence of elastic deformations the response to an external electric field $\mathbf{E}^{em}$ is a transverse charge current with opposite signs at each Fermi point: $\langle J^i_\tau \rangle = e^2 C_\tau \varepsilon^{ij} E^{em}_j$, so the total charge current $\langle J^i_{\vec{K}} + J^i_{\vec{K}'} \rangle$ vanishes. The synthetic elastic field will induce a charge response in the system at each Fermi point: $\langle J^i_\tau \rangle \sim \tau C_\tau \varepsilon^{ij} E^{el}_j$. Now, because $C_{\vec{K}} = -C_{\vec{K}'}$ the total net charge current is non zero and its value is twice larger than the value at each Fermi point:

$$\langle J^i_{\vec{K}} + J^i_{\vec{K}'} \rangle \sim 2 C_{\vec{K}} \varepsilon^{ij} E^{el}_j . \tag{32}$$

This result can also be understood from the mixed Chern-Simons action arising from the combined vector field $V_i = A^{em}_i + \tau \mathcal{A}^{el}_i$. Within a functional integral approach one can integrate out the fermionic degrees of freedom $\psi_{\tau,\vec{k}}, \psi^\dagger_{\tau,\vec{k}}$ in the action derived from Eq. (31) and write the odd part of the effective Lagrangian:

$$\begin{aligned} \mathcal{L}_{eff} &= 2 e g_2 C_{\vec{K}} \varepsilon^{\mu\rho\nu} A^{em}_\mu \partial_\rho \mathcal{A}^{el}_\nu + 2 e g_2 C_{\vec{K}} \varepsilon^{\mu\rho\nu} \mathcal{A}^{el}_\mu \partial_\rho A^{em}_\nu + \\ &+ J^\mu A^{em}_\mu + J^\mu_{el} \mathcal{A}^{el}_\mu , \end{aligned} \tag{33}$$

where we have added to the Chern–Simons action the external sources: J^μ is the total charge density current that naturally couples to the electromagnetic field, and J^μ_{el} is a classically conserved current associated to the elastic field $\mathcal{A}^{el}_\mu$. Notice that the standard Chern–Simons term bilinear in A^{em} or $\mathcal{A}^{el}$ vanishes for the total action due to the opposite value of C_K at the two valleys. Only the mixed term survives. The total charge current density ($\mathcal{S}_{eff} = \int d^3 \mathcal{L}_{eff}$) is:

$$\langle J^i \rangle = \frac{\delta \mathcal{S}_{eff}}{\delta A^{em}_i} = 2 e \hat{\beta} C_K \varepsilon^{ij} \dot{\mathcal{A}}^{el}_j \equiv 2 e g_2 \frac{m}{|m|} \varepsilon^{ij} E^{el}_j , \tag{34}$$

where for simplicity it has been assumed that $\mathcal{A}^{el}_0 = 0$ and have replaced $\varepsilon^{ij0} = \varepsilon^{ij}$. Notice that the generation of this transverse electric current in a time reversal invariant system does not contradict the general result of "no Hall current in T-invariant systems" because the Hall current is the response to an electric field while the present current is the response of the system to a time-dependent elastic deformation. A schematic description of the various possible valley currents is presented in Fig. 2. The action discussed here is similar to the Wen–Zee action described in Section 2.5.1 but there the additional vector field that couples to the electromagnetic field in the mixed Chern Simons term was induced by the geometric spin connection (higher order in derivatives, see discussion in Section 2.3) while here it is the elastic gauge field. The result in both cases is similar: an electromagnetic response induced by a time–dependent deformation. This can also be seen as a quantum analogue of standard piezoelectricity.

Elastic electric fields have also been analysed recently in [137, 138, 139]. As it is known, what prevents graphene from having observable topological properties is the the small value of the spin orbit coupling and the difficulty to open a gap in the spectrum. It has recently observed that depositing graphene on hexagonal BN opens a sizeable gap and a valley Chern invariant arises in commensurate stacking [140]. These type of heterostructures are discussed at length in Section 5.

3. Lattice anharmonic effects in crystalline membranes

3.1. Theory of anharmonic crystalline membranes

3.1.1. Classical theory for ideal free, flat membrane

The usual starting point for the study of lattice properties of a solid is the harmonic theory for lattice vibrations. The harmonic theory is valid provided that the fluctuations of the atoms around the equilibrium positions are much smaller than the average interatomic distance. In bulk three-dimensional crystals, the harmonic theory, or minimal extensions of it as the quasi-harmonic approximation, is usually a sufficient approximation for most applications. However, the situation is quite different in two-dimensional crystalline membrane (membranes with a finite shear modulus, also referred to as solid membranes), such as graphene and other two dimensional crystals, where, due to the low dimensionality, atomic fluctuations are not small.

As a matter of fact, it was argued by Peierls [141] and Landau [142] that two dimensional crystals should not exist at any finite temperature. Mermin [143] formalized this argument and proved that, provided the pair interaction between two atoms decays faster than r^{-2} (r is the distance between atoms), there is no positional long-range order. However, there is a residual quasi-long range order, characterized by correlations with a logarithmic behaviour with distance, which is typical of two dimensional systems. Nevertheless, Mermin also pointed out that orientational long-range order can still exist.

For a free two dimensional crystalline membrane embedded in a three dimensional space, the situation is potentially worse since now the membrane has the possibility of fluctuating in the third dimension. Therefore the study of properties of the flat phase in crystalline membranes, its thermodynamic stability and the study of in-plane and out-of-plane positional and orientational orders became a topic of intensive research in the context of statistical mechanics (for an in depth discussion on the physics of membranes, the interested reader can refer to Refs. [4, 144, 145]). It turns out that, although a free crystalline membrane does not have positional long range order, the anharmonic interaction between in-plane and out-of-plane modes is essential in reducing fluctuations and protecting the long-range in-plane and out-of-plane orientational orders, such that a flat configuration of the membrane is thermodynamically stable. [3, 23, 146].

Much of the physics of flat crystalline membranes can be understood using the simple classical model of continuous local elasticity with a potential energy described by Eq. (17). [3, 23] As already discussed in Sec. 2.2, the inclusion of the term $\partial_i h \partial_j h$ in the strain tensor u_{ij} makes the theory defined by Eq. (17) interacting. Neglecting anharmonic effects, in-plane and out-of-plane modes are decoupled and at classical level the theory is described by the correlation functions

$$\langle h(\vec{q})h(-\vec{q})\rangle_0 = \frac{k_B T}{\rho(\omega_{\vec{q}}^F)^2} = \frac{k_B T}{\kappa|\vec{q}|^4}, \tag{35}$$

$$\begin{aligned}\langle u_i(\vec{q})u_j(-\vec{q})\rangle_0 &= \frac{k_B T}{\rho(\omega_{\vec{q}}^L)^2} P_{ij}^L(\vec{q}) + \frac{k_B T}{\rho(\omega_{\vec{q}}^T)^2} P_{ij}^T(\vec{q}) \\ &= \frac{k_B T}{(\lambda+2\mu)|\vec{q}|^2} P_{ij}^L(\vec{q}) + \frac{k_B T}{\mu|\vec{q}|^2} P_{ij}^T(\vec{q}),\end{aligned} \tag{36}$$

where $P_{ij}^{L/T}(\vec{q})$ is the longitudinal/transverse projector along the momentum $\vec{q}$, $\omega_{\vec{q}}^F$, $\omega_{\vec{q}}^L$ and $\omega_{\vec{q}}^T$ are, respectively, the dispersion relations for the flexural, in-plane longitudinal and in-plane transverse phonons (see Eqs. (11), (12) and (16) of Sec. 2.2), and $\langle\rangle_0$ is a thermal average with respect to the harmonic theory. Using the harmonic correlation functions to compute the on-site displacement-displacement correlation functions one obtains

$$\left\langle \vec{u}^2 \right\rangle_0 = \int \frac{d^2\vec{q}}{(2\pi)^2} \langle u_i(\vec{q})u_i(-\vec{q})\rangle_0 \sim \log\left(L/a\right), \tag{37}$$

$$\left\langle h^2 \right\rangle_0 = \int \frac{d^2\vec{q}}{(2\pi)^2} \langle h(\vec{q})h(-\vec{q})\rangle_0 \sim L^2, \tag{38}$$

where L is the linear size of the membrane and a is an interatomic distance. The logarithmic dependence of $\left\langle \vec{u}^2 \right\rangle_0$ with the system size is the expected behaviour of quasi-long range order in two dimensional systems. However, the linear growth of the out-of-plane fluctuations with system size, $\sqrt{\langle h^2\rangle_0} \sim L$, indicates that at harmonic level a flat membrane is not possible, and that the membrane is instead crumpled. There is however a long range in-plane orientational order, which can be seen by looking at [143]

$$\left\langle \partial_i u_j \partial_k u_l \right\rangle_0 = \int \frac{d^2\vec{q}}{(2\pi)^2} q_i q_k \langle u_j(\vec{q})u_l(-\vec{q})\rangle_0, \tag{39}$$

which remains finite. There is also a quasi-long range order of the local normals of the membrane, $\hat{\mathbf{n}}(x)$,

$$\langle \delta\hat{\mathbf{n}} \cdot \delta\hat{\mathbf{n}} \rangle_0 \simeq \int \frac{d^2\vec{q}}{(2\pi)^2} |\vec{q}|^2 \langle h(\vec{q})h(-\vec{q})\rangle_0 \sim \log\left(L/a\right), \tag{40}$$

where, to lowest order in the displacements, $\delta\hat{\mathbf{n}}(x) = \hat{\mathbf{n}}(x) - \hat{\mathbf{z}} \simeq -(\nabla h(x), 0)$, with $\hat{\mathbf{z}}$ the unit vector pointing in the reference out-of-plane direction. Nelson and Peliti [3] were the first to argue that the interactions between the in-plane and out-of-plane fluctuations present in Eq. (17) would give origin to a long-range interaction between local Gaussian curvatures (which to lowest order in the displacements reads $-\nabla^2 P^T_{ij}\partial_i h \partial_j h/2$), that would stabilize the flat phase. Since Eq. (17) is quadratic in the in-plane displacements, u_i, these can be integrated out, and the effective action describing the dynamics of the out-of-plane mode is given by [3]

$$S_{\text{eff}}[h] = \frac{\kappa}{2}\int d^2\vec{r}\left(\partial^2 h\right)^2 + \frac{Y}{8}\int d^2\vec{r}\left(P^T_{ij}\partial_i h\partial_j h\right)^2, \tag{41}$$

where $Y = 4\mu(\lambda+\mu)/(\lambda+2\mu)$ is the two dimensional Young modulus of the membrane. Computing to lowest order in perturbation theory the self-energy correction to the out-of-plane mode correlation function, $\langle h(\vec{q})h(-\vec{q})\rangle = k_B T\left(\kappa|\vec{q}|^4 + \Sigma(\vec{q})\right)^{-1}$, due to the anharmonic terms in Eq. (41) one obtains [3, 4, 147, 148, 149]

$$\Sigma(\vec{q}) = \frac{3Yk_BT}{16\pi\kappa}|\vec{q}|^2. \tag{42}$$

As we go to low momentum we have that $\Sigma(\vec{q}) \gg \kappa|\vec{q}|^4$, which shows that perturbation theory breaks down and that a crystalline membrane is a strongly interacting system. Using a Ginzburg like criterion, from the condition $\Sigma(\vec{q}) \simeq \kappa|\vec{q}|^4$, the momentum scale below which anharmonic effects become dominant is given by[3, 4, 150, 147, 148, 149]

$$q^* = \sqrt{\frac{3k_BTY}{16\pi\kappa^2}}, \tag{43}$$

which for graphene has the value $q^* \simeq 0.2$ Å^{-1}. This momentum scale can be translated into a length scale $L^* = 2\pi/q^* \simeq 3$ nm, that is typical size of a membrane above which anharmonic effects become dominant. For large membranes and below the anharmonic scale q^*, Nelson and Peliti [3] showed that a non-perturbative treatment calculation of the self-energy leads to a correlation function for the out-of-plane displacement characterized by an anomalous momentum dependence. A renormalization group calculation [23] showed that the in-plane correlation functions also acquire an anomalous momentum dependence. In general, at small momenta the behaviour of the displacement correlation functions is characterized by two exponents η_h and η_u, such that

$$\langle h(\vec{q})h(-\vec{q})\rangle \sim q^{-4+\eta_h}, \tag{44}$$

$$\langle u_i(\vec{q})u_j(-\vec{q})\rangle \sim q^{-2-\eta_u}. \tag{45}$$

This behaviour can also be seen as the effective elastic constants becoming momentum dependent at low momenta

$$\kappa_{\text{eff}}(q) \sim q^{-\eta_h}, \tag{46}$$

$$\lambda_{\text{eff}}(q), \mu_{\text{eff}}(q) \sim q^{\eta_u}. \tag{47}$$

Using the renormalization group method, it was shown that the exponents η_h and η_u are not independent, but are related by [23, 146]

$$\eta_u + 2\eta_h = 4 - D, \tag{48}$$

where D is the dimension of the membrane, with $D = 2$ for physical membranes. Provided $\eta_h > 0$ and $\eta_u < 2$ (for $D = 2$, these are equivalent conditions, provided Eq. (48) holds), there is in-plane and out-of-plane long-range orientational order, since taking into account the momentum dependence of the effective elastic constants yields

$$\langle \partial_i u_j \partial_k u_l\rangle \sim L^{\eta_u - 2}, \tag{49}$$

$$\langle \delta\hat{\mathbf{n}}\cdot\delta\hat{\mathbf{n}}\rangle \sim L^{-\eta_h}, \tag{50}$$

and therefore a flat phase for the membrane is indeed stable. It was argued in Refs. [151, 146] that the lower critical dimension above which a flat phase for a crystalline membrane is possible should be smaller than 2. Anharmonic effects also reduce the crumpling of the membrane, since the height fluctuations scale with the system size as

$$\langle h^2 \rangle \sim L^{2\zeta}, \tag{51}$$

where $\zeta = 1 - \eta_h/2$ is the roughness exponent of the membrane. At the same time, for $\eta_u > 0$, the anharmonic effects generated by the out-of-plane fluctuations lead to a degradation of the positional quasi-long range order of the membrane, since

$$\langle \vec{u}^2 \rangle \sim L^{\eta_u}. \tag{52}$$

The anomalous dependence on momentum of the effective elastic constants was confirmed using the self-consistent screening approximation for the continuous model described by Eq. (17) [152, 153, 147], Monte Carlo and molecular dynamics simulations [154, 155, 156, 157, 158, 159] and functional renormalization group methods [160, 161, 162, 163]. The relation between anomalous exponents Eq. (48) was also derived using the self-consistent screening approximation [164, 152] and was further tested using Monte Carlo simulations [155, 156].

Although it is believed that the anomalous exponents should be universal quantities, there is some dispersion on the reported values. An analytical result obtained using the self-consistent screening approximation (which becomes exact in the limit of large codimension of the membrane, d_C, which for a physical membrane if given by $d_C = 3 - 2 = 1$) gives a value for η_h of 0.821 [152], an improved self-consistent calculation to next leading order in $1/d_C$ gives a value of 0.789 [153], functional renormalization group calculations give 0.849 [160, 163] and 0.85 [161, 162], molecular dynamics simulations give 0.81 [154], Monte Carlo simulations give 0.72 [155, 156], 0.85 [157] and 0.795 [158], while renormalization group Monte Carlo gives 0.79 [159].

3.1.2. Deviations from the ideal case: defects, corrugations and residual strains

The previous section concerned ideal membranes without defects and unconstrained by any external stress or fixed boundary condition. In an experimental setup graphene samples are either supported on a substrate or suspended over a trench. In supported samples coupling to the substrate leads to the opening of a gap in the out-of-plane phonon dispersion relation and, therefore, anharmonic effects should be severely quenched [27]. A suspended sample is much closer to the ideal case. Nevertheless, even a suspended sample is still subject to constrained boundary conditions, residual stresses, impurities and other sources of disorder. Therefore, it is important to understand how the previous discussion is affected once we consider these effects.

The possibility of buckling due to constrained boundary conditions was studied in Refs. [165, 166]. The effect of residual stresses was studied in Ref. [167], where it was found that the anomalous momentum dependence of the correlation functions survived for small externally applied stresses. It was estimated that, in graphene, an applied stress corresponding to a strain of 0.25% can completely quench anharmonic effects.

The effect of disorder in the stability of flat membranes was studied in Refs. [168, 169, 170, 171], where disorder was simulated by random strain and curvature fields. It was found that disorder can indeed destabilize the flat phase and that this instability can still be present at finite temperature, depending on the type of disorder. This possibility was verified with atomistic simulations of graphene [172], where it was found that a 20% adsorption of OH molecules leads to crumpling of the membrane. Membranes with a frozen non-flat background metric characterized by out-of-plane variances with a power law dependence on momentum, called warped membranes, were studied in Refs. [173, 174]. In these works it was found that for strong enough fluctuations of the background metric the anomalous exponents can differ from the ones due to thermal fluctuations in a flat membrane. The effect of short range quenched curvature disorder was also recently studied in Ref. [175] using a renormalization group analysis. There it was found that the experimental results of Refs. [176] and [177], for the average size of ripples and the mean deviation of the normals in suspended graphene samples, compare well with values obtained with the renormalization group analysis for weak curvature disorder.

3.1.3. Quantum theory

The previous discussion was based on a classical description of membranes. The original theoretical works on crystalline membranes were motivated by the study of biological amphiphilic membranes [4]. Since such objects are formed by very large molecules, one can expect that their mechanical behaviour will be governed by classical statistical mechanics at room temperature. The same assumption is not easily justifiable in atomically thin membranes such as graphene. A simple estimation of graphene's Debye temperature, gives us $T_D \sim 1000$ K, considerably larger than room temperature. In this scenario one expects that quantum effects will still be important at room temperature.

The quantum treatment of flexural phonons was first performed in Ref. [178], in the context of the study of the combined effects of phonon-phonon and electron-phonon interactions in graphene. Performing a self-consistent calculation, it was found that at zero temperature and in the absence of electron-phonon interactions, anharmonic effects lead to logarithmic corrections to the bending rigidity of graphene. The effect of quantum fluctuations at zero temperature on the Young modulus was studied in Ref. [179] using an expansion in the number of out-of-plane directions of the membrane (which for a physical membrane is one). It was found out that quantum fluctuations contribute to a reduction of the Young modulus at small momentum scales, just as thermal fluctuations, although being a much smaller effect. It was estimated that thermal fluctuations are dominant with respect to quantum fluctuations for momentum scales smaller than the thermal wavelength for flexural phonons

$$q_Q(T) = \left(\sqrt{\frac{\rho}{\kappa}} \frac{k_B T}{\hbar} \right)^{1/2} . \tag{53}$$

Anharmonic crystalline membranes at zero temperature were also studied in Ref. [180] by performing a renormalization group study. It was found that zero temperature fluctuations lead to an increase of the effective coupling constant between in-plane and out-of-plane phonons which leads to a destabilization of the flat phase of the membrane. This behaviour is to be contrasted with the effect of thermal fluctuations, which lead to an increase of the bending rigidity at large length scales, and therefore stabilize the flat phase. Refs. [178, 179, 180] did not take into account retardation effects for the in-plane phonons, effectively treating them as classical, on the basis that typical frequencies of in-plane phonons are much larger than the frequencies of out-of-plane phonons at low momenta. The effect of retardation of the in-plane phonons was studied in Ref. [148, 149] by means of a perturbative calculation of the out-of-plane phonon self-energy. It was found that such retardation effects, change the corrections to the bending rigidity from being logarithmic to a power law in momentum, contributing to an increase of the bending rigidity at long wavelengths, a scenario that is very similar to the one due to thermal fluctuations. Furthermore, it was estimated that the effect of quantum fluctuations is dominant for temperatures smaller than

$$T^* \simeq \frac{2\hbar}{3 k_B \rho^{1/2} \kappa^{1/2}} \frac{(\lambda + 2\mu)^2}{Y} f, \tag{54}$$

where f is a dimensionless cutoff dependent quantity. For graphene it is estimated that $T^* \simeq 70 - 90$ K. The momentum scale below which anharmonic effects dominate, in the low temperature regime, was found to be smaller but of the same order of magnitude as in the high temperature limit Eq. (43). Quantum corrections to thermodynamic and elastic properties of graphene were also studied in Ref. [181], by means of a self-consistent calculation of the density matrix, where it was found that quantum and anharmonic effects become comparable for temperatures smaller than 100 K, while quantum fluctuations still play a significant role for temperatures as high as 1000 K.

The contradictory nature of the results published so far does not allow one to access what is the exact role and importance of quantum effects in the physics of crystalline membranes, such as graphene.

3.1.4. Anharmonic effects and electron-phonon interaction

As we have seen in the previous sections, the flat phase of a crystalline membrane is very fragile and anharmonic effects play a very important role. In membranes that have low energy electronic excitations,

such as graphene, one might ask if these electronic degrees of freedom can have a significant impact in the physics of crystalline membranes.

This question was first addressed in Ref. [182]. There it was argued that the deformation potential interaction between graphene electrons and phonons, Eq. (19), gives origin to an effective strain of the form $\sigma = g_1 n$, where n is the electronic carrier density. This coupling is asymmetric with respect to electron or hole doping. While for electron doping, $n > 0$, the membrane would be subject to a tension, in the case of hole doping, $n < 0$, the membrane would be subject to a compressive strain, which would lead to the buckling of the membrane. Such a structural deformation induced by electron-phonon interaction bears some resemblance with the physics of the Peierls transition and formation of charge density waves. The role of electron-phonon interactions in undoped graphene was studied in Ref. [183], where it was shown that the decay of flexural phonons into electron-hole pairs, leads to the disappearance of the flexural mode branch below a critical momentum. It was speculated that such disappearance could be associated with the formation of ripples. A perturbative evaluation of the normal-normal correlation function in the classical limit performed in Ref. [53], also displayed a peak at finite momentum induced by the electron-phonon interaction. Such peak was interpreted as signalling the onset of ripples. The same problem was studied at zero temperature in Ref. [178], via a self-consistent evaluation of flexural phonon correlation function and it was found that for large values of the deformation potential, $g_1 \simeq 23.1$ eV, the effective bending rigidity vanishes at a finite momentum scale of the order of $q \sim 0.1$ Å. Similar conclusions were found in Ref. [179], where, by treating electrons and phonons on equal footing, it was found that electron-phonon interaction can drive the system towards an instability in the charge carrier density - Gaussian curvature channel at finite momentum, that was speculated to be associated with the spontaneous and simultaneous formation of structural ripples and charge puddles. This mechanism is suppressed by the presence of an electronic bandgap, and should therefore be more relevant in graphene than in semiconductor transition metal dichalcogenides or boron nitride. The nature of this electron induced instability was further studied in Ref. [184], by means of a self consistent calculation and a renormalization group calculation. It was found that the vanishing of the effective bending rigidity and the condensation of the mean curvature (which is given by $\partial^2 h$) are simultaneous and manifestations of the same transition at finite momentum. This transition should occur even in the absence of an external tension and does not involve an in-plane distortion. Nevertheless, the nature of the relevant operators at this critical point is still not clear, and a condensation of the Gaussian curvature could not be ruled out. Therefore, further analysis is needed to clearly identify the electron-phonon interaction as a candidate to the formation of ripples in graphene.

3.2. Mechanical properties

3.2.1. Structure of suspended two dimensional crystals

One of the most important quantities in the study of the structure of matter is the static structure factor $S(\mathbf{q}) = \sum_{n,m} \left\langle e^{i\mathbf{q}\cdot(\mathbf{R}_n - \mathbf{R}_m)} \right\rangle$, where $\mathbf{R}_n$ are the atomic positions (in 3D space), $\mathbf{q} = (q_x, q_y, q_z)$ is the transferred momentum and the average is to be understood as a time or ensemble average. As discussed in Sec. 3.1.1, in a crystalline membrane displacement-displacement correlation functions have an anomalous momentum dependence, which will affect the structure form factor. In a scattering experiment, Bragg peaks will no longer be sharp, but will instead be broadened with an algebraic decay. It is in this weaker sense, that a two dimensional crystal is defined [9, 185]. The structure factor of rough, self-affine membranes and surfaces [2], characterized by power law displacement variances: $\left\langle |h(\vec{x}) - h(\vec{x}')|^2 \right\rangle = A\,|\vec{x} - \vec{x}'|^{2\zeta}$ and $\left\langle |\vec{u}(\vec{x}) - \vec{u}(\vec{x}')|^2 \right\rangle = B\,|\vec{x} - \vec{x}'|^{\eta_u}$, has been theoretically studied in several works [186, 187, 164, 188, 189, 190]. A semi-analytical expression for the structure factor of flat membranes subject to thermal fluctuations was obtained in Refs. [187, 164, 188]. For $q = 0$, (with $q = \sqrt{q_x^2 + q_y^2}$) it was found that the structure factor has a power law behaviour $S(q = 0, q_z) \sim q_z^{-2/\zeta}$, while $S(q, q_z = 0)$ did not show a well defined power

[2] A surface is said to be self-affine if its roughness is described by a random variable with probability distribution that is invariant under anisotropic scaling transformations of the form $x \to bx$ and $z \to b^\zeta z$

law behaviour. In Ref. [189] the orientationally averaged structure factor, $S(|\mathbf{q}|)$, was studied in detail. It was found that for $1/L \ll q \ll 1/\ell$, where L is the membrane size and ℓ is the characteristic length scale of out-of-plane or in-plane fluctuations, one obtains $S(|\mathbf{q}|) \sim |\mathbf{q}|^{-2}$ as in a completely flat, non-fluctuating membrane [186]. For $1/\ell \ll q \ll 1/a$, where a is the lattice spacing, it was obtained $S(|\mathbf{q}|) \sim |\mathbf{q}|^{\zeta-3}$, for the case where in-plane fluctuations are small compared to out-of-plane, and $S(|\mathbf{q}|) \sim |\mathbf{q}|^{\eta_u/\zeta-2/\zeta-2}$, in the opposite case.

The roughness exponent, ζ, of red blood cell membrane skeletons was obtained from the structure factor measured with light and x-ray scattering [191]. The roughness exponent was extracted by fitting the orientationally averaged structure factor to the power law behaviour $S(|\mathbf{q}|) \sim |\mathbf{q}|^{\zeta-3}$, having been obtained a value of $\zeta = 0.65 \pm 0.10$, which is in good agreement with the theoretical prediction for thermal fluctuations in a flat crystalline membrane (see Eq. (51) and text below). The exponent η_h was also measured in amphiphilic films [192], by fitting the structure factor measured with x-ray scattering, with a continuous model that neglects in-plane fluctuations. The best fit was obtained for $\eta_h = 0.7 \pm 0.2$, once again in good agreement with the theory of thermal fluctuations in a flat membrane.

It was experimentally found that suspended samples of both graphene and bilayer graphene display roughness [176, 193]. Transmission electron microscopy revealed that samples with lateral sizes of $\sim$ 500 nm display broadened Bragg peaks with Gaussian shape. These roughness showed no preferred orientation, and is associated with static ripples. It was estimated that these ripples have a characteristic lateral size of 2 - 20 nm and a mean deviation of the normals of the membrane of 5% in single-layer and 2% in bilayer graphene. The typical height of the ripples was estimated to be of 1 nm. Similar corrugations have also been observed in suspended samples of MoS_2 [194]. The roughness of suspended graphene was further studied using low-energy electron microscopy and diffraction in Ref. [195]. It was found that at small length scales, suspended graphene appears to be a self-affine surface characterized by a correlation length of $\xi \simeq 24$ nm and a roughness exponent of $\zeta \simeq 0.5$. At larger length scales, graphene seemed to present a preferred ripple wavelength of $\lambda_{\text{ripple}} \simeq 60$ nm. Existence of the two length scales ξ and λ_{ripple} indicate that at large length scales graphene deviates from a purely self-affine surface and seems to be a mounded surface.[195] It was also found that the roughness exponent becomes smaller with increasing temperature and with increasing exposition time to an electron or photon beam. Furthermore, it was found that suspended bilayer and trilayer graphene present a roughness exponent of $\zeta \simeq 0.8$. Scanning tunnelling microscopy studies [196] further confirmed the static nature of ripples in suspended graphene. The ripples found in Ref. [196] had a characteristic lateral size of 5 nm and showed to be static for imaging times of about 5 minutes. The used samples were subject to annealing and reported to be free of contamination over areas of tens of nm^2. The amplitude of the corrugation of graphene was further studied in Ref. [177] with transmission electron microscopy, where, by analysing the width of diffraction peaks, it was obtained a height and normal variances of $\sqrt{\langle h^2 \rangle} = 1.7$ Å and $\sqrt{|\nabla h|^2} = 0.011$, with a characteristic length scale of 10 nm, for suspended samples with a size of 0.5-5 μm. It was also found that, at least for length scales smaller than 100 nm, the height fluctuation decreases with increasing temperature.

The exact origin of the static corrugation presented in graphene samples is still unclear. While the temperature dependence of the corrugation measured in Refs. [195, 177] indicates that thermal activation of phonons should play a role, the theory of flat anharmonic crystalline membranes alone is unable to explain the static nature of the observed ripples in [176, 193] and the non-universal roughness exponents measured in Ref. [195]. A possible origin of the ripples is that in a suspended graphene sample, its edges are constrained and therefore the membrane is unable to freely expand or contract, leading to buckling and the formation of ripples [165, 166]. Therefore, residual thermal or external stresses could lead to the formation of ripples. Thermal and external stresses have indeed been used to form ripples in graphene suspended over trenches as reported in Ref. [10]. This has been explained with the theory from Ref. [197] based on classical elasticity, but seems unrelated to the short wavelength corrugations reported in Refs. [176, 193, 195, 177]. Another possibility is that in the fabrication process of a suspended graphene sample, relaxation of a constrained graphene membrane after removal of the substrate could lead to rippling, or the ripples might themselves be inherited from the substrate [198]. Electron-phonon interaction in graphene might also lead to a crumpling instability of the membrane [182, 178, 179]. Disorder has also been proposed as a source

of ripples. Indeed, the numerical simulations from Ref. [172] show that a 20% adsorption of OH molecules leads to the crumpling of a graphene membrane compatible with amplitudes and typical sizes of corrugation observed in experiments. Scanning transmission electron microscopy also shows that the presence of point defects as vacancies and adatoms, such as hydrogen or carbon atoms, favours rippling [199, 200]. These disorder induced ripples might still display dynamics due to migration of the defects.

Scanning tunnelling microscopy studies were also capable of probing time-dependent height fluctuations of suspended graphene [201]. At small bias voltages ($\sim$ 0.01 V) and currents (0.2 nA), random on-site fluctuations were attributed to thermal fluctuations. These displayed a variance of $\sqrt{\langle h^2 \rangle} = 1.47$ nm, with a characteristic decay time of $\tau = 8s$ ($\langle h(t)h(0)\rangle \propto e^{-t/\tau}$). It was also found that for larger currents and gate voltages, effects of thermal expansion due to the local heating of graphene and the electrostatic forces induced by the tip can lead to periodic oscillations of the membrane and to mirror buckling [201, 202, 203].

3.2.2. Anomalous elasticity

The Young modulus of graphene was first measured using a blister test in Ref. [25], where an atomic force microscope is used to perform a nanoindentation in a graphene membrane suspended over a circular hole, with sizes of 1 and 1.5 μm in diameter. The two-dimensional Young modulus, $Y_{\rm eff}$, was determined by fitting the force–indentation curve by [204, 205, 206, 207]

$$F = \sigma_0 \pi \delta h + Y_{\rm eff} \vartheta^3 \frac{(\delta h)^3}{d^2}, \tag{55}$$

where F is the applied force, δh is the displacement of the membrane at its centre, σ_0 is a pretension, d is the membrane diameter and $\vartheta = \left(1.05 - 0.15\nu - 0.16\nu^2\right)^{-1}$, where ν is the Poisson ratio of the membrane [204, 206]. By taking $\nu = 0.165$, the obtained value for the Young modulus of graphene was 342 N/m [25], a value that makes graphene the stiffest material to have ever been measured.

Equation (55) is derived from the Föppl–von Kármán plate theory, which is described by a free energy of the form of Eq. (17) [21]. However, while the high bending rigidity of a plate strongly suppresses thermal fluctuations, which can therefore be neglected, on a membrane long wavelength vibrations are thermally excited and interact due to strong anharmonic effects. As discussed in Sec. 3.1.1 this leads to an anomalous dependence on momentum of the displacement correlation functions, which translate into a scale dependence of the elastic constants. As a matter of fact, while the starting potential energy that describes the membrane is a local functional of the displacements, the free energy will become non-local [161, 162]. Assuming that the strain induced by the indentation is nearly uniform over most of the sample, we can assume that Eq. (55) is still valid, but with a scale dependent Young modulus $Y_{\rm eff}(\ell) \propto \ell^{-\eta_u}$ (Eq. (47)), where ℓ is the characteristic length scale of the problem (which can be the size of the membrane, a length scale imposed by the induced strain, or a length scale due to disorder or an initial corrugation of the membrane). This justifies the use of Eq. (55).

It has been experimentally found that the Young modulus of graphene increases with the density of defects created by bombardment of Ar^+ ions [208], provided the density is not too high. The measured Young modulus, changed from 250 - 360 N/m for pristine graphene, to 550 N/m for graphene with an average defect distance of 5 nm (0.2 % coverage of defects). The increase of the Young modulus has been explained in terms of the classical theory of flat anharmonic crystalline membranes described in Sec. 3.1.1. According to it, the Young modulus becomes smaller at larger length scales. The creation of defects would introduce a new length scale, the average distance between defects, which acts as an effective membrane size from the point of view of the graphene phonons. Being smaller than the membrane size, this new scale would restore the value of graphene's Young modulus to a higher value than in the absence of defects. The Young modulus in Ref. [208] was measured with a nanoindentation technique and by fitting the obtained force-displacement curve to Eq. (55) for different graphene drums. In Fig. 3 the experimental value of the Young modulus obtained in this way is plotted versus the density of defects for the different drums. The Young modulus grows up to twice its pristine value for all the drums with the same law; the experimental curves then show a crossover to a decreasing regime as the density of defects is increased, as expected from first principle calculations[209, 210, 211]. These competing behaviours can be encoded in a qualitative fitting

to the experimental data

$$Y_{\rm eff} = K\left(b + \frac{1}{l_0^2} + n_i\right)^{\eta_u}\left(1 - c\left(\frac{1}{l_0^2} + n_i\right)\right), \tag{56}$$

where n_i is the density of defects, K and c are constants to be evaluated from the fit, b is a geometrical parameter of the order of the inverse of the area and l_0 is the localization length for the flexural phonons in pristine graphene. Best fitting with the experimental data, shown in Fig. 3 with the broken green line, is

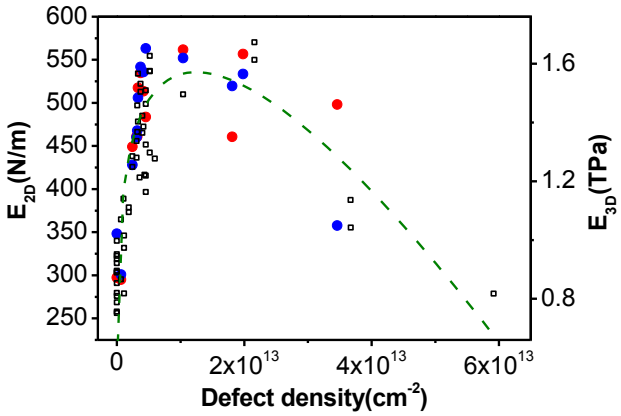

Figure 3: Young Modulus as a function of the defects density[208] (see main text). The broken green line represents the best fitting to the data via Eq.(56).

given by the value of the parameters $K = 1.5 \times 10^9$N m$^{\eta_u - 2}$, $l_0 = 70$ nm, $\eta_u = 0.36$ and $c = 1.2 \times 10^{-18}$ m^2. The localization length l_0 takes into account other sources of disorder that can introduce an effective length in the problem. The radii used in Ref. [208] vary from 500 nm to 3 μm and thus the estimated value is such that $1/l_0^2 \gg b$. This justifies the independence of the growth of the Young modulus observed. The above interpretation is supported by recent experimental measurements of the evolution of the Young modulus with external strain [212], where it was found that the in-plane elastic constant increases by a factor of 2 when the membranes are under tension. This effect is expected from the elastic theory of membranes, which predict that external strain suppresses thermal out-of-plane fluctuations, with the corresponding enhancement of the Young modulus [167]. Recent atomistic Monte Carlo simulations have shown that external tension can indeed cause an increase of the Young modulus in a factor of 2 [213], in agreement with the experiments [212]. However, the discrepancy between the Young modulus measured by indentation experiments on tensioned membranes, and that obtained by *ab initio* calculations is an open question. Another experimental evidence of the importance of anharmonicities on the elastic properties of atomically thin membranes has been reported by Blees *et al.* [214], who have shown that the bending rigidity of micro-ribbons of graphene is three order of magnitude larger than its microscopic value. These results have been studied theoretically in the framework of a renormalization group analysis of flexural phonons on elongated ribbons, which are enough to explain the qualitative behaviour [215]. Nevertheless, further studies, both experimental and theoretical, are required in order to fully understand the elastic behaviour of graphene.

3.3. Thermodynamic properties

3.3.1. Thermal expansion

Thermal expansion is an intrinsically anharmonic effect. In bulk three-dimensional crystals, thermal expansion is well described with the quasi-harmonic approximation. This is essentially a minimal mean field extension of the harmonic theory, where the phonon frequencies depend on the lattice expansion. The

dependence of the phonon frequencies on the expansion is encoded in the so called Grüneisen parameters. For crystalline membranes anharmonic effects will be too strong to treat in this matter. At not too high temperatures, thermal expansion will be controlled by the low energy out-of-plane phonons and can be studied using the elasticity model (17). In a quasi-harmonic approach, the Grüneisen parameter for out-of-plane phonons is given by [216]

$$\gamma(q) = -\frac{\lambda+\mu}{2\kappa q^2}, \tag{57}$$

which diverges for small momenta. The areal thermal expansion is defined as being the change with temperature of the membrane area projected onto the reference plane. Within elasticity theory the relative change of projected area is given by $\langle \partial_i u_i \rangle$. In terms of the out-of-plane mode Grüneisen, the thermal expansion in the quasi-harmonic approximation is given by [216, 9]

$$\alpha_A = \frac{k_B}{\lambda+\mu} \int \frac{d^2\vec{q}}{(2\pi)^2} \left(\frac{\hbar\omega_{\vec{q}}^F}{2k_B T} \right)^2 \frac{\gamma(q)}{\sinh^2\left(\frac{\hbar\omega_{\vec{q}}^F}{2k_B T}\right)}. \tag{58}$$

From the previous expression, it is clear that in the quasi-harmonic approximation the thermal expansion for an infinite membrane will be divergent at any finite temperature [216, 148]. Inclusion of anharmonic effects beyond the quasi-harmonic approximation corrects this unphysical result. In the context of the model described by Eq. (17), the areal thermal expansion can be exactly written as a normal-normal correlation function [216, 27, 148]

$$\alpha_A = -\frac{1}{2}\frac{\partial}{\partial T} \langle \partial_i h(x) \partial_i h(x) \rangle \,. \tag{59}$$

This is the formal expression of the membrane effect [217]: the intuitive picture that the thermal excitation of out-of-plane vibrations should lead to a reduction of the area of the membrane. Equation (59) always predicts a negative thermal expansion, being a limitation of the model (17). Higher order anharmonic effects, such as cubic terms in $\partial_i u_j$, would give origin to competing terms, that at high enough temperature, could change the sign of the thermal expansion. Nevertheless, at low temperature, Eq. (59) is the main contribution. If the average in Eq. (59) is taken with respect to the harmonic theory, one recovers the result from the quasi-harmonic approximation. Going one step beyond the quasi-harmonic approximation, one can estimate the contribution due to strong anharmonic effects at low momentum by taking the Ginzburg momentum scale (43) as a low momentum cutoff, obtaining [216]

$$\alpha_A \sim -\frac{k_B}{4\pi\kappa} \log\left(\Lambda/q^*\right), \tag{60}$$

where Λ is a large momentum cutoff, which one takes to be the thermal wavelength for flexural phonons at intermediate temperatures and the Debye momentum at high temperatures. Using typical values for graphene one obtains a thermal expansion of $\alpha_A \sim -10^{-5}$ K^{-1}. This estimation is in agreement with more involved calculations using a quasi-harmonic approximation based on *ab initio* calculations [218], classical Monte Carlo simulations [26], non-equilibrium Green's functions method [219], *ab initio* molecular dynamics [12, 220] and self-consistent-field methods [181]. The thermal expansion at very low temperature is dominated by flexural phonons, and it was found that in the quantum limit, inclusion of anharmonic effects renders the thermal expansion finite in the thermodynamic limit, behaving with temperature as $\alpha_A \propto -T^{2\eta_h/(4-\eta_h)}$, for flexural phonons with dispersion relation of the form $\omega_{\vec{q}}^F \propto q^{2-\eta_h/2}$ [148, 149].

There is a debate regarding the behaviour of the thermal expansion coefficient of graphene with temperature. From the theoretical point of view, while Refs. [218] and [12] predict an always negative thermal expansion (Ref. [12] predicts this only for large enough samples, while for small samples there is a change of sign), Refs. [26, 219, 220] predict a change of sign in the thermal expansion for temperatures in the range $600 - 900$ K. This possible change of sign occurs due to a competition of thermal contraction due to the anharmonic effects involving the out-of-plane mode and thermal expansion due to the in-plane modes. It is very important to emphasize that the thermal expansion of graphene greatly depends on whether it is free

or if it is supported on a substrate [12, 27, 220]. It was also found that the calculated thermal expansion is dependent on the size of the simulated system [12, 220], which can be understood since the anharmonic coupling between out-of-plane and in-plane vibrations lead to long range interactions [3] which might be difficult to simulate numerically. The discrepancy of results can be attributed to the different approximations involved in the calculation. An accurate description of the physics would have to take into account quantum effects, anharmonic effects in a non-perturbative way and should be extensible to the thermodynamic limit (a non-trivial task, from the numerical point of view, since anharmonic effects are stronger at larger length scales).

Experimentally, the thermal expansion coefficient of graphene has been measured in suspended samples [10], and was found out to be negative up to 350 K with a value of $\alpha_A \simeq -7 \times 10^{-6}\ \mathrm{K}^{-1}$ at 300 K. The thermal expansion coefficient was also measured in supported samples by Raman spectroscopy[11] and was found to be negative in the range $200 - 400$ K, with an obtained value of $\alpha_A \simeq -8 \times 10^{-6}\ \mathrm{K}^{-1}$ at room temperature. The data from Ref. [10] was successfully described by the theory of Ref. [181], which is formulated in the thermodynamic limit, taking into account anharmonic effects in a self-consistent way and including lowest order quantum corrections to the classical result.

The areal thermal expansion discussed so far, being a change of the project area of the membrane, is related to the change of the lattice parameter. Another interesting quantity is the change in nearest neighbours carbon-carbon distance. There is also no consensus regarding the behaviour of this quantity with temperature. Monte Carlo simulations indicate that for small temperatures there is also a reduction in the carbon-carbon distance, reaching a minimum at a temperature of $T \simeq 700$ K [26]. On the other hand, *ab initio* molecular dynamics simulations show that the carbon-carbon distance always increases with temperature up to $T = 1000$K, even when the lattice parameter contracts [12]. Experimentally it is verified that the carbon-carbon distance increases in graphene supported by an iridium substrate over the temperature range of $300 - 1200$ K [12]. However, one must point out, that theoretically it is also expected that the carbon-carbon distance should increase for supported graphene [12] and therefore, it is not clear if the experimental result on supported graphene can be extrapolated to the suspended case.

3.3.2. Specific heat

Another thermodynamic quantity that is affected by anharmonic effects is the specific heat. Anharmonic effects are significant both in the high and low temperature limits. At high temperature, anharmonic effects lead to a violation of the Dulong–Petit law: instead of a saturation of the specific heat to a value of k_B per degree of freedom, one obtains a linear correction on temperature for high enough temperature. This was investigated via Monte Carlo simulations in Ref. [26], where it was found that the specific heat at constant volume in graphene per carbon atom for temperatures $T > 800$ K is approximately given by

$$c_A = 3k_B \left(1 + \frac{k_B T}{E_0}\right), \tag{61}$$

with $E_0 = 1.3$ eV. Inclusion of quantum effects to lowest order [181] leads to a specific heat of the form

$$c_A = 3k_B \left(1 - \frac{k_B T}{E_1} - \left(\frac{E_2}{k_B T}\right)^2\right), \tag{62}$$

with $E_1 \simeq 0.053$ eV and $E_2 \simeq 0.022$ eV. The second term of the previous expression corresponds to the first quantum correction to the classical anharmonic result.

At low temperatures, anharmonic effects also lead to a correction to the power law dependence of the specific heat with temperature, since the low energy acoustic phonons acquire a renormalized dispersion relation. This was studied in Ref. [148, 149], where it was found that at very low temperatures, where the main contribution to the specific heat is given by the flexural phonons, the harmonic result for the specific heat, $c_p \propto T$, is corrected to $c_p \propto T^{4/(4-\eta_h)}$, for flexural phonons characterized by a dispersion relation of the form $\omega_q^F \propto q^{2-\eta_h/2}$.

3.4. Topological defects

A closely related problem to strain in graphene is the presence of topological defects in the otherwise perfect crystalline system. The literature of topological defects in graphene is so vast that one can consider that this topic might deserve a review by itself. However, there are several reasons that motivate the inclusion of a section about these defects in the present review. If we think on a graphene layer as a crystalline membrane, structural defects play an important role in the way a membrane melts. Just as elastic deformations affect the electronic properties of graphene at low energies, so will topological defects, but in a different way.

The role of topological defects in the melting and crumpling thermal phase transitions in two dimensional membranes was envisaged and developed long time before the appearance of graphene[221, 222]. In the melting scenario of Refs. [221, 222] for strictly two dimensional crystals, the positional quasi-long range order is destroyed at high enough temperature by the sequential release, first of dislocations and, at higher temperature, of disclinations. The possibility of buckling in the out-of-plane direction leads to a reduction of the formation energy of defects such as dislocations and disclinations [3, 2, 223].

In graphene, due to the covalent nature of the σ bonds, responsible of the structural properties, the melting transition shows some differences both at qualitative and quantitative levels. Although in graphene the presence of topological defects made of a single heptagon-pentagon pair (dislocations) is allowed, it is the presence of Stone-Wales defects (formed by two pentagons and two heptagons) that plays a crucial role according to Monte Carlo simulations, since they are the structural defects with smallest formation energy (in practical terms, the Stone-Wales defect consists in just rotating one carbon-carbon link by 90 degrees). The melting transition temperature has been estimated to lie in the range $T_c \sim 4500 - 5800K$[224, 225]. At the transition temperature, the system starts to form an amorphous network of one dimensional carbon chains. The same effect has been studied in carbon systems with small number of carbon atoms[226]. We should have in mind that the mentioned Monte Carlo simulations are performed keeping constant the number of carbon atoms during the simulation. It is quite likely that at lower temperatures than the ones mentioned above something more drastic, such as burning, will take place.

At low temperatures (well below any melting transition) topological defects still have an effect in the elastic properties of graphene. Early signatures of the role played by defects on the elastic and plastic properties of carbon-based structures appeared in the literature of nanotubes[227, 228]. It was explained that the way a carbon nanotube releases tension is to form Stone-Wales defects when the strain exceeds the critical value of five per cent. Quite remarkably, the Stone-Wales defects act as nucleation centres for the formation of dislocations, in the sense that when more tension is applied, the Stone-Wales defect splits and the two pentagon-heptagon pairs start to separate, and even to form more complex defects.

Back to graphene, it has recently been observed through high-resolution transmission electron microscopy that dislocations carry with them sizeable elastic deformations[229]. Interestingly, the dislocations and the associated elastic distortion are dynamical, that is, they can move with time in order to release stress. The time scales of these movements are of the order of seconds, too slow to have any impact in the electronic dynamics, but this defect movement might have an impact in the elastic dynamics of graphene as a membrane. Also, understanding the way these defects evolve constitutes an interesting problem on its own. In Ref. [229] it has been observed that, as happens in nanotubes, under stress the plastic deformations start with the formation of Stone-Wales defects[230]. Increasing the applied stress, the two pentagon-heptagon pairs split apart[231]. In the experiments shown in Ref. [229], the two heptagon-pentagon defects are separated by several lattice spacings. It has also been found experimentally that the dislocation movement is accompanied by the removal of carbon atoms (activation energy of the order of 5 eV) to accommodate the energy irradiated by the transmission electron microscope. It has been also observed[232] that buckling has a profound impact in the dynamics of a dislocation from its origin, since for a membrane, distortions along the third dimension are allowed and graphene samples might also release elastic energy via buckling. This buckling process induces a long-ranged interaction between the heptagon-pentagon pairs, and the relative direction of the associated Burgers vectors determines the buckling profile, indicating an unexpected large feedback between the dislocation configuration, its associated buckling and the way the pentagon-heptagon pairs mutually interact through this buckling.

From the theoretical side, the dislocation dynamics in graphene is still an open problem. Significant advances have been achieved with discrete[231] and continuous[233, 234] modelling. Nevertheless, the fact that the defect dynamics seems not to be well described by the standard theory of dislocation dynamics indicates that the particular lattice topology of the honeycomb lattice might play an important role.

In the previous discussion, we only gave a small glimpse of the role of small topological defects on the elastic properties of a graphene membrane. However, it is by now apparent that in realistic samples extended defects are also present and they possibly have a more unexpected impact on the elastic properties of graphene. One-dimensional extended topological defects usually appear in chemically vapour deposited samples grown over metallic substrates, due to the fact that small graphene grains with different crystalline orientation serve as nucleation points and form large-area samples[235, 236, 237].

Usually, the structure of such grain boundaries consists on heptagon-pentagon pairs along the grain boundary [238]. In Ref. [238] it was stated that if the borders of adjacent graphene flakes are of zig-zag type, the Burgers vectors associated to each heptagon-pentagon pair are parallel, while if the borders are of armchair type, the associated Burgers vectors lose this constraint. Also, depending on the relative mismatch between the crystalline orders, the grain boundaries will be made of well separated heptagon-pentagon pairs (low tilt angles) or a dense array of them (high tilt angles). By using molecular dynamics plus *ab initio* calculations, it has theoretically observed that the strength of the graphene sample counterintuitively increases with the number of defects in the grain boundary, with the critical strain needed to break the sample growing with the number of pentagon-heptagon pairs present in the grain boundaries)[238]. Interestingly, calculations based on continuum mechanics fail to explain this behaviour, indicating that it is the microscopic lattice structure of these grain boundaries the ultimate responsible of the obtained behaviour. The reason behind this is that what controls the failure under strain (which carbon bonds start to break first) is the way the strain is not uniformly accommodated along all the carbon bonds, and it tends to concentrate in the carbon bonds on the heptagon rings, being then the first to break. This indicates that the system releases strain by breaking carbon bonds around the heptagonal defects, leaving the rest of hexagonal rings much more free of strain.

This scenario has been partially questioned due to the fact that graphene can also release strain by buckling (or warping) as it has been mentioned previously. Other groups employing similar numerical techniques find that actually the stress-strain curve is not monotonic with the increase of defects, meaning that not always the strength of the sample increases with the number of defects at the grain boundaries[237]. In previous paragraphs we mentioned that the buckling around two close pentagon-heptagon pairs strongly depended on the relative orientation of their Burgers vectors, and the same applies here. The relevant point here is then to know if the relative orientation between the Burgers vectors plays the same role when the distance between heptagon-pentagon pairs is smaller than in the previous cases of a dilute density of dislocations. While for zig-zag borders this constraint seems to be quite general, we have much more freedom to choose the way the Burgers vectors are not parallel to each other. In this way, for armchair grain boundaries, many possible defect configurations with different Burgers vectors can be found, and accepting that the buckling profile depends on the Burgers vectors orientation, it is reasonable, at least qualitatively, to expect that the way the graphene sample will release strain by buckling (and the behaviour of the strength of the graphene sample) is not as uniform and universal as one might initially think.

4. Electronic properties

4.1. Strains and the mobility of carriers in graphene

Graphene is an excellent conductor, with carrier mobilities similar, or higher, than those found in good metals, like copper or silver. The lack of dependence of the mobility on carrier concentration in graphene strongly limits scattering mechanisms. Defects which induce a short range potential lead to a mobility proportional to the *inverse* of the concentration, which is incompatible with observations. Static strains are a possible source of disorder, and limit the mobility of the carriers. Other proposed mechanisms which lead to the correct dependence of mobility on carrier concentration are charged impurities in the substrate, and resonant scatterers[239]. It is worth noting that thermally excited phonons lead to random strain

distributions which can scatter electrons. The in-plane acoustic phonons of graphene are only relevant at high temperatures [240], but out-of-plane flexural modes in suspended samples change significantly the mobility, being the primary electron scattering mechanism at room temperature [150], giving origin to a T^2 dependence of resistivity [241]. In supported samples, out-of-plane phonons become quenched and their contribution to resistivity is severely reduced [27].

4.1.1. Strains and mobility.

In order for strains to give the correct (in)dependence of the mobility on carrier concentration, they should be correlated over long distances, as initially proposed in [242]. In the following, we analyse the influence of strains in electronic transport, following recent experimental and theoretical work reported in [243]. As discussed there, it is natural to expect long range correlations in the strain distribution, and strains are the only mechanism compatible with weak localization experiments and the observed correlation between the mobility and the strength of puddles near the neutrality point.

The carrier mobility μ_c is defined as the conductivity per carrier,

$$\mu_c = \frac{\sigma}{en}, \tag{63}$$

where σ denotes the conductivity, e is the electric charge, and n the carrier density. The highest mobilities are found in exfoliated flakes, which are single crystals. They lie in the range 10^3-10^5 cm^2/(V s), and are independent of the carrier concentration [244, 245, 246]. Different substrates lead to different mobilities, and the highest values are found in samples on boron nitride substrates and in suspended samples, where mean free paths can be of the order of few microns.

If we describe the scattering of carriers by disorder in terms of an effective scattering time τ, we can write

$$\mu_c = \frac{e}{h}\frac{2\pi v_F \tau}{k_F}, \tag{64}$$

where h is Planck's constant, v_F is the Fermi velocity, and k_F is the Fermi wavevector. Below, we review some properties of the mobility [7, 247, 248], and (following the work in [243]) present arguments which suggest that the dominant mechanism which determines the mobility is the presence of random strains in the system.

4.1.2. Form of the disorder potential

The internal structure of the wavefunctions of carriers in graphene implies that, within states in a given valley, an internal degree of freedom, the pseudospin, can be defined. The value of the pseudospin is determined by the carrier's momentum, and a variation of the pseudospin affects the phase of the wavefunction in a similar way as that of a real spin in a material with strong spin-orbit coupling. The effect of the pseudospin can be measured in weak localization experiments, as they probe interference effects by applying a small magnetic field which breaks the effective time-reversal symmetry of electronic states around each K-point. These experiments allow for the definition of three different scattering times [249, 250]: (i) τ_0, a scattering time which changes momentum but does not influence the phase of the wavefunction, (ii) τ_*, which describes the suppression of interference associated to random fluctuations of the pseudospin, and (iii) τ_i, which gives the strength of the inter-valley scattering processes (we neglect here the effect of the real spin-orbit coupling in graphene, which is very small). The total scattering time, τ, which enters in the mobility is given by $\tau^{-1} = \tau_0^{-1} + \tau_*^{-1} + \tau_i^{-1}$.

Weak localization experiments [251, 252, 253] show that $\tau_*^{-1} \approx \tau^{-1} \gg \tau_i^{-1}$. Thus, the random potential $V(\vec{q})$ responsible for the scattering processes in graphene must be described by a long range potential, which does not allow for inter-valley scattering. In addition, this potential should couple to the pseudospin of the wavefunction.

Further, the experimental observation of a mobility which is independent of carrier concentration implies that the effective scattering time $\tau \propto k_F$ [see Eq. (64)]. The scattering time is due to processes which transfer a carrier from one position on the Fermi surface to another. We assume that the Fermi surface is a

circle, and that the scattering mechanism is isotropic. Then, a scattering process by an angle θ involves a momentum transfer $\vec{q}$ such that $|\vec{q}| = 2k_F \sin(\theta)$, and the inverse of the scattering time (according to Fermi's golden rule) can be written as

$$\frac{1}{\tau} = \frac{2\pi}{\hbar^2}\frac{N(E_F)}{4\pi^2}\times \\ \times \int_0^{\pi} d\theta\,[1-\cos(\theta)]\,\langle V(\vec{q})V(-\vec{q})\rangle|_{|\vec{q}|=2k_F\sin(\theta/2)}\,, \tag{65}$$

where $N(E_F) \propto k_F/v_F$ is the density of states at the Fermi energy E_F and $\langle\,\rangle$ denotes average over disorder. The $\tau \propto k_F$ dependence mentioned above implies that

$$\langle V(\vec{q})V(-\vec{q})\rangle|_{|\vec{q}|=2k_F\sin(\theta/2)} \propto \frac{1}{k_F^2}. \tag{66}$$

Hence, the potential which scatters the carriers has to diverge like $|\vec{q}|^{-1}$ as $k_F \to 0$.

4.1.3. Correlation between mobilities and puddles at the Dirac point

Experiments show a linear correlation between the mobility at high carrier concentration and the minimum carrier density which can be measured near the neutrality point [243]. Defects can shift locally the position of the Dirac energy, so that, for nominal zero concentration, the carrier density fluctuates, with a non zero absolute average. This effect (typically referred to as the existence of puddles [254]) leads to a lower bound in the resolution of the carrier density, n^*, near neutrality.

The observed dependence is $1/\mu_c = Cn^*$, where C is a constant which does not depend on the type of substrate or amount of disorder.

4.1.4. Carrier scattering by defects and impurities

Apart from the aforementioned random strains, there are various theoretical models describing the charge scattering in graphene. The different microscopic mechanisms relate to different scattering times τ and carrier mobilities μ:

(i) *Weak defects:* The simplest scattering mechanism is given by local scatterers which perturb weakly the band structure of graphene. Each of these scatterers can be described by a momentum independent potential $\bar{V}$, resulting in

$$\tau^{-1} \propto N(E_F)\bar{V}^2 \propto k_F. \tag{67}$$

(ii) *Charged impurities:* The electrostatic potential induced by a point charge,

$$V(\vec{q}) = V_C(\vec{q})/\varepsilon(\vec{q}), \tag{68}$$

where $V_C(\vec{q}) = e^2/(2\varepsilon_0|\vec{q}|)$ is the 2D Coulomb potential (in SI units), ε_0 is vacuum permittivity and $\varepsilon(\vec{q}) = 1 + V_C(\vec{q})N(E_F) = 1 + (e^2k_F)/(2\pi v_F\varepsilon_0|\vec{q}|)$ is the static dielectric function in graphene, satisfies the scaling law Eq. (66). The resulting scattering time τ and mobility are

$$\tau^{-1} \propto \frac{c_{ch}v_F}{k_F}, \\ \mu_c \propto \frac{e}{h}\frac{1}{c_{ch}}, \tag{69}$$

where c_{ch} is the concentration of charged impurities, independent of the carrier density[255, 256, 257]. This mechanism can be consistent with the correlation between μ_c and n^* described in Sec. 4.1.3.

(iii) *Resonant scattering:* A strong local potential, like the one induced by a vacancy or an adatom covalently bonded to a neighbouring carbon atom, induces a strong resonance near the Dirac energy[258, 259]. A potential of this type also satisfies the scaling behaviour in Eq. (66), and leads to a mobility

$$\mu_c \propto \frac{e}{h}\frac{1}{c_{res}}, \tag{70}$$

where c_{res} is the concentration of resonant scatterers.

The scattering time Eq. (67) for weak defects is inconsistent with the observed independence of the mobility on carrier density. On the other hand, the long range potential induced by charged impurities, Eq. (68), does not modify the pseudospin, while resonant scatterers have dimensions comparable to the lattice spacing, and can thus be expected to induce inter-valley scattering. This leaves mechanisms (ii) and (iii) at odds with the results of weak localization experiments described in Sec. 4.1.2.

4.2. Carrier scattering by random strain fluctuations

The effect of strains on electrons and holes in graphene can be divided into a scalar potential, $V_s(\vec{r}) = g_1\left(u_{xx}(\vec{r}) + u_{yy}(\vec{r})\right)$, and a gauge potential, $\vec{\mathcal{A}}^{el}(\vec{r}) = g_2\left(u_{xx}(\vec{r}) - u_{yy}(\vec{r}), -2u_{xy}(\vec{r})\right)$, see Eqs. (19),(20), where u_{ij} is the strain tensor, and g_1 and g_2 are constants [8] discussed in Sec. 2.3. Random strains will give rise to a potential which satisfies the scaling in Eq. (66) if

$$\langle u_{ij}(\vec{q})u_{kl}(-\vec{q})\rangle|_{|\vec{q}|=k_F} \propto \frac{1}{k_F^2} \tag{71}$$

While the gauge field $\vec{\mathcal{A}}^{el}$ does not break the electron-hole symmetry of the graphene bands, so that it cannot induce density fluctuations near the neutrality point, the scalar potential V_s does break this symmetry, and can therefore lead to the formation of puddles [55]. On the other hand, the scalar potential does not couple to the pseudospin of the wavefunction, while the gauge potential does, and hence can explain the weak localization experiments. The two contributions to the potential lead to the scattering times

$$\begin{aligned}\frac{1}{\tau_s} &= \frac{2\pi}{\hbar^2}\frac{N(E_F)}{4\pi^2} \\ &\times \int_0^\pi d\theta\, \frac{1-\cos^2(\theta)}{2}\frac{\langle V_s(\vec{q})V_s(-\vec{q})\rangle}{\varepsilon^2(\vec{q})}\Big|_{|\vec{q}|=2k_F\sin(\theta/2)}\end{aligned} \tag{72}$$

$$\begin{aligned}\frac{1}{\tau_g} &= \frac{2\pi}{\hbar^2}\frac{N(E_F)}{4\pi^2} \\ &\times \int_0^\pi d\theta\, [1-\cos(\theta)]\langle \vec{\mathcal{A}}^{el}_\perp(\vec{q})\vec{\mathcal{A}}^{el}_\perp(-\vec{q})\rangle\Big|_{|\vec{q}|=2k_F\sin(\theta/2)},\end{aligned} \tag{73}$$

where $\vec{\mathcal{A}}^{el}_\perp(\vec{q})$ is the component of $\vec{\mathcal{A}}^{el}$ perpendicular to $\vec{q}$, as $\vec{\mathcal{A}}^{el}_\parallel(\vec{q})$ can be gauged away. The average puddle density due to the scalar potential is

$$n^* = \frac{1}{\pi}\frac{\langle V_s(\vec{r})^2\rangle}{(\hbar v_F)^2} = \frac{1}{4\pi^3\hbar^2 v_F^2}\int d^2\vec{q}\frac{\langle V_s(\vec{q})V_s(-\vec{q})\rangle}{\varepsilon^2(\vec{q})}. \tag{74}$$

The scalar potential is screened by the static dielectric function, $\varepsilon(\vec{q})$, while the gauge potential is not. That implies that $\tau_g^{-1} \ll \tau_s^{-1}$. Hence, when the scattering is induced by strains, $\tau \sim \tau^* \sim \tau_g$, in agreement with the weak localization experiments described above.

In the following, we discuss strain due to out-of-plane corrugations and to in-plane displacements. Their effect on spectral properties will be discussed in Sec. 5. Both types of strain lead to potentials consistent with the scaling behaviour in Eq. (66), and with the observed correlation between mobility and puddle density.

4.2.1. Random out-of-plane corrugations

Random out-of-plane corrugations have been observed in graphene on different substrates (where it is assumed that they follow the corrugations of the substrate) [245] as well as in suspended samples [176]. The fluctuations in the height of the graphene layer, $h(\vec{r})$, give rise to strains $u_{ij} \propto \partial_i h \partial_j h$. For the relation (71) to hold, we have

$$\left\langle \partial_i h \partial_j h|_{\vec{q}}\, \partial_k h \partial_l h|_{-\vec{q}} \right\rangle \propto \frac{1}{|\vec{q}|^2}. \tag{75}$$

This momentum dependence can be obtained if [242]

$$\langle h(\vec{q}) h(-\vec{q}) \rangle \propto \frac{1}{|\vec{q}|^4}. \tag{76}$$

The correlation function (76) describes the thermal distribution of classical flexural modes in the harmonic approximation (see Section 3.1). Hence, if we assume that the corrugations in a graphene flake are given by the quenched shape of that flake at some high temperature, we obtain a mobility which is independent of the carrier concentration.

Assuming a height scaling as in Eq. (76), the relation between mobility and average puddle density satisfies

$$\frac{1}{\mu_c} = n^* \frac{h}{4e} \left[\frac{\hbar^2 v_F^2}{8e^4} + \frac{g_2^2 (\lambda+\mu)^2}{g_1^2 \mu^2} \right] \frac{1}{\log[1/(k_F(n^*)a)]}, \tag{77}$$

which, neglecting the last logarithmic factor, only depends on parameters defined in the absence of disorder. For reasonable values of g_1 and g_2 this relation is in close agreement with the experimentally observed one [243].

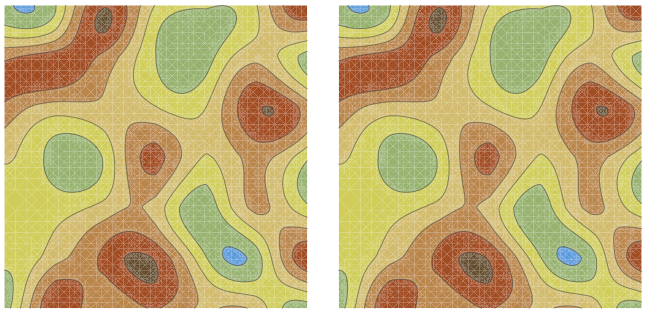

Figure 4: (Colour online). Sketch of the potential (left) and forces (right) induced by the substrate on a graphene layer. To compare with a floating phase configuration, cf. Fig. 12.

4.2.2. In-plane random displacements

The substrate induces in-plane forces on the carbon atoms that constitute the graphene layer, such that the atoms will be displaced towards positions which lower the potential energy. This effect is responsible for the formation of Moiré patterns in graphene on BN substrates [260, 261, 262]. A sketch of a possible random potential induced by the substrate, and the resulting displacements, is given in Fig. 4. A detailed analysis of this issue concerning periodic deformations is carried out in Sec. 5, where a floating phase is assumed. (See in particular the discussion in Section 5.2.)

Forces $\vec{F}$ with a modulation $\vec{K}$ similar to the reciprocal vectors of the graphene lattice, $\vec{G}$, lead to smooth displacement distributions, modulated by the wavevector $\vec{k} = \vec{K} - \vec{G}$:

$$\vec{u}(\vec{k}) \propto \frac{\vec{F}_\parallel(\vec{k})}{(\lambda+2\mu)|\vec{k}|^2} + \frac{\vec{F}_\perp(\vec{k})}{\mu|\vec{k}|^2}, \tag{78}$$

where $\vec{F}_{\parallel}(\vec{k})$ and $\vec{F}_{\perp}(\vec{k})$ denote the components of $\vec{F}(\vec{k})$ parallel and normal to $\vec{k}$, respectively, and λ and μ are elastic Lamé coefficients, as discussed in Sec. 2.2. The linear strain tensor is given by $u_{(i,j)}(\vec{k}) = i\left(k_i u_j(\vec{k}) + k_j u_i(\vec{k})\right)/2$.

The forces can be written as a function of the potential between the substrate and the graphene layer

$$\vec{F}(\vec{K}) = i\vec{K}V_{\vec{K}}. \tag{79}$$

Hence, for $\vec{K} \approx \vec{G}$, we find

$$\left\langle u_{(i,j)}(\vec{k})u_{(l,m)}(-\vec{k})\right\rangle \propto \frac{|\vec{G}|^2\left\langle V_{\vec{G}-\vec{k}}V_{-\vec{G}+\vec{k}}\right\rangle}{|\vec{k}|^2}. \tag{80}$$

We assume that the potential $V_{\vec{G}-\vec{k}}$ has random correlations for $|\vec{k}| \ll |\vec{G}|$. Then $\lim_{|\vec{k}|\to 0}\left\langle V_{\vec{G}-\vec{k}}V_{-\vec{G}+\vec{k}}\right\rangle =$ constant, and the correlation between strains follows the scaling in Eq. (71). This mechanism gives a mobility which is independent of the carrier concentration. The relation between the mobility and the puddles' density is, similar to that in Eq. (77),

$$\frac{1}{\mu_c} = n^*\frac{h}{4e}\left[\frac{\hbar^2 v_F^2}{16e^4} + \frac{g_2^2}{g_1^2}\left(1 + \frac{(\lambda+2\mu)^2}{\mu^2}\right)\right] \times \frac{1}{\log[1/(k_F(n^*)a)]}. \tag{81}$$

As in Eq. (77), for reasonable values of the parameters of g_1 and g_2, the relation between μ_c and n^* agrees with experiments [243].

Thus, scattering of charge carriers by random strains, as detailed in Sections 4.2.1 and 4.2.2 above, fulfils the experimental constraints which a microscopic charge scattering mechanisms in graphene must satisfy. Moreover, these constraints, namely (i) the existence of a mobility independent of carrier concentration, (ii) the dominance of long range intra-valley scattering processes coupled to the wavefunction's pseudospin, and (iii) the correlation between mobility and puddles' density near the neutrality point, are not consistent with the other models for scattering discussed in Section 4.1.4 [243]. Furthermore, spatially resolved Raman measurements show a good correlation between carrier mobilities and amplitudes of strain distributions [243].

4.3. Electron pumping through mechanical resonance in graphene

While electron scattering from random microscopic strain configurations or from thermally excited phonons contributes to the resistivity of graphene sheets, macroscopic deformations (with amplitudes of a few nanometres in samples of micrometres in size) produced in graphene based nano-electromechanical systems (GNEMS) can generate electrical current by moving electrons coherently[263]. A typical setting for a GNEMS is made up of a graphene flake of length L suspended over a pre-patterned trench. The suspended flake serves as a mechanical resonator, which can be actuated via a radiofrequency gate-voltage applied between graphene and the substrate[264, 265]. In alternative, optical actuation can be achieved by modulating the intensity of a diode laser shone over the flake[264]. Since their first experimental realization [264], GNEMS have been fabricated in various ways: graphene flakes produced by mechanical exfoliation[264], CVD[266], or by epitaxial growth on SiC[267], have been suspended on differently shaped substrates.

In the miniaturization of NEMS to the nanoscale, which calls for low oscillator masses and high resonance frequencies [268, 269, 270], graphene with its low mass density, high stiffness, high electronic mobility, and its chemical inertness is a promising material [263, 271]. Furthermore, graphene allows tunability of the resonance frequency ω_0 on a wide range by means of strain: Modelling the graphene membrane as a beam, ϵ scales with the square root of the applied strain ϵ,

$$\omega_0 = \frac{1}{2L}\sqrt{\frac{Y}{\rho}\epsilon}, \tag{82}$$

where Y denotes the Young modulus of graphene. Eq. (82) takes into account only the effect of tension on the fundamental frequency. A realistic model of a graphene resonator must also further consider the electrostatic force between graphene and the substrate, the elastic restoring force and possible dissipative effects[263, 272].

Read-out of GNEMS can be performed through electrical or optical means[271]. It has been shown that, due to the long wave-length strains induced by vibrations, a GNEM close to resonance can work as an adiabatic quantum charge pump[263]. If inversion symmetry is broken by maintaining different chemical potentials at graphene contacts on opposite ends of the trench, one obtains a nonzero pumping current such that the transport of a single charge per cycle is feasible. Coulomb blockade in such a device would result in the transport of an integer number of charges per cycle, so that the ratio between current and frequency will be quantized. This paves the way to the application of GNEMS as prototypical standards for current and resistance.

4.4. Other effects of strains on the electronic structure of graphene.

Strains modify the hoppings between carbon π orbitals. As mentioned in the introduction, this effect shifts the Dirac point from the corners of the Brillouin Zone, and leads to the appearance of effective gauge fields[8]. When the strains are spatially modulated, an effective magnetic field s induced. A smoothly increasing strain leads to an effective constant magnetic field[57]. This effect was confirmed by observing the local density of states of highly strained triangular graphene bubbles on platinum[59]. The combination of large strains, $\epsilon \sim 10\%$, which change over a small scale, $\ell \sim 15$ nm, and a triangular shape favour the formation of large effective fields. Numerous experiments have confirmed the existence of significant effective magnetic fields in strained graphene, see, for instance[273, 61, 274].

4.5. Effects of electron-electron interactions in strained graphene

The effect of electron-electron interactions in graphene has been a central research area in the field since the early days [275]. At half-filling, and unlike in typical metallic systems, Coulomb interactions have a long-range character due to the vanishing density of states at the Dirac point, resulting in an enhancement of the Fermi velocity at low energies [276, 277, 278]. On the other hand interactions in doped graphene are screened, but can nevertheless lead to remarkable phenomena. For instance, a particularly appealing scenario occurs when graphene is doped up to the van Hove singularity, where the divergent density of states makes it prone to a number of interesting weak coupling instabilities including d-wave superconductivity [279, 280, 281, 282, 283, 284].

The interplay between strain and interaction effects opens a different avenue to explore and enhance novel interaction related phenomena. For instance, by applying uniaxial strain, it is possible to alter the electronic spectrum and bring the van Hove singularity to lower energies [89] and rippled disorder can also enhance interactions [198]. In what follows, we focus on how electron-electron interactions of different kinds can affect strained graphene and the different phenomena they induce.

4.5.1. Topological phases induced from the interplay between strain and interactions

Unlike symmetry broken phases, topological states of matter are described and classified by topological invariants [106, 107]. This rapidly expanding and multidisciplinary field was boosted by and largely benefited from research in graphene itself [109, 110], cf. Sec. 2.5 .

An exciting alternative to access topological phases is through the interplay between strain and electron-electron interactions. For instance, an early example was motivated by the magnetic catalysis scenario for real magnetic fields in graphene [285]. This mechanism, identified first in high-energy physics, refers to the enhancement of the dynamical symmetry breaking by an external magnetic field [286]. In the context of graphene it is responsible for the opening of a gap catalyzed by the strong magnetic field, which favours the electron-hole pairing formation. For pseudo-magnetic fields, it was shown [287, 288, 289] that strained graphene is similarly unstable towards an interaction induced gap, but in this case the ground state breaks time reversal symmetry and has a finite Hall conductivity [109].

An experimentally plausible scenario emerges when considering strain configurations that result in strong

uniform pseudo-magnetic fields [57, 290]. In this set-up, the uniform pseudo-magnetic field splits the spectrum into pseudo Landau levels (PLL)

$$E_n = \mathrm{sgn}(n)\sqrt{2n}\hbar v_F/l_B \qquad \psi^{\vec{K}}_{n,m} = \psi^{\vec{K}'}_{n,m} = \begin{cases} \frac{1}{\sqrt{2}}(\phi_{|n|-1,m}(z), \mathrm{sgn}(n)\phi_{|n|,m}(z)) & \text{if } n \neq 0, \\ (0, \phi_{0,m}) & \text{if} n = 0. \end{cases} \tag{83}$$

with $l_B = \sqrt{\hbar/(eB)}$ being the standard magnetic length corresponding to the pseudo-magnetic field strength, B, and $\phi_{n,m}$ are the wave functions of the n-th level of the non-relativistic Landau level problem with angular momentum eigenvalue m. The states are four-fold (spin and valley) degenerate. They enjoy a $\mathbb{Z}_2 \times SU(2)$ symmetry, where $\mathbb{Z}_2$ represents the time-reversal symmetry while $SU(2)$ are the spin-rotations. Note that this is in sharp contrast to the $SU(4)$ symmetry in an external real magnetic field where also the wave functions are different for different $\vec{K}$ and $\vec{K}'$ points; $\psi^{\vec{K}}_{n,m} \neq \psi^{\vec{K}'}_{n,m}$.

Long-range electronic interactions can lift the large degeneracy of a PLL defined in Eq. (83) and lead to interesting ordered states, including topologically non-trivial phases. To tackle this many-body problem, it is generally assumed that interactions are not strong enough to mix different PLL. In this case it is possible to distinguish the two cases in (83), i.e. $n \neq 0$ and $n = 0$. Considering $n \neq 0$, the projected Hamiltonian describing long-range interactions can be written as [291]

$$\mathcal{H}_{\mathrm{int}} = \sum_{\vec{q}} V_C(\vec{q}) n(\vec{q}) n(-\vec{q}). \tag{84}$$

Here $V_C(\vec{q})$ is the Fourier transform of the long-range Coulomb interaction and the projection is encoded in the definition of the density operator $n(\vec{q}) = \sum_{\kappa,\sigma} \bar{n}_{\kappa,\sigma}(\vec{q})$, where $\bar{n}_{\kappa,\sigma}(\vec{q})$ are density operators projected to the n-th PLL that depend on the valley $\kappa = \vec{K}, \vec{K}'$ and spin $\sigma = \uparrow, \downarrow$ degrees of freedom. In particular, the pseudo magnetic field has opposite signs at the $\vec{K}$ and $\vec{K}'$ points, a fact that is reflected through the dependence on κ.
Within the Hartree-Fock approximation the leading instability for a 1/4 or 3/4 filled $n \neq 0$ PLL is a state with broken $\mathbb{Z}_2$ valley symmetry. Such a state is not time-reversal symmetric and has a quantized $\sigma_{xy} = e^2/h$. In turn, for a half-filled $n \neq 0$ PLL with spin-orbit coupling a similar analysis shows that interactions drive the system to a quantum spin-Hall effect with a quantized spin Hall response [291].
Interestingly, the possibility of realizing the elusive fractional Chern insulators (FCI) (for a review see [292]), zero-magnetic field analogues of the fractional quantum Hall effect, has also been proposed within this scenario [293, 291]. Via exact diagonalization it was shown that a partially filled $n = 0$ PLL stabilizes a valley polarized fractional quantum Hall state at 2/3 filling through long-range Coulomb interactions that is robust to repulsive nearest neighbour interactions [293]. By further tuning the latter to attractive interactions, a time-reversal symmetric fractional topological insulator state is stable as well as a spin-triplet superconducting state. Motivated by these findings, the stability of the former against different interactions was also further addressed [294].

Inhomogeneous pseudo-magnetic field configurations can also lead to topological insulating phases. For instance, consider a site dependent hopping amplitude of the form [288]

$$t_{ij} = e^{\chi(i)} t e^{-\chi(j)} \tag{85}$$

with $i \in A$ and $j \in B$ and t a constant hopping amplitude. The function $\chi(\mathcal{R})$, with $\mathcal{R}$ defined as a radial coordinate from a central hexagon (see Fig. 5) models a lattice gauge potential that can interpolate between an approximately uniform pseudo magnetic field ($\chi(\mathcal{R}) \propto \mathcal{R}^2$) to a bell-shaped field ($\chi(\mathcal{R}) \propto \ln \mathcal{R}$) while preserving C_3 rotational symmetry. In analogy to the pristine unstrained graphene [295] fermions at half filling subjected to a strain pattern and repulsive interactions can realize topological Chern and spin Hall insulator phases. The starting point is the Hamiltonian

$$\mathcal{H} = \sum_{\langle i,j \rangle} t_{ij} \left(c_i^\dagger c_j + \mathrm{h.c.} \right) + U \sum_{i,\sigma,\sigma'} n_{i,\sigma} n_{i,\sigma'} + V_1 \sum_{\langle\langle i,j \rangle\rangle,\sigma,\sigma'} n_{i,\sigma} n_{j,\sigma'} + V_2 \sum_{\langle\langle i,j \rangle\rangle,\sigma,\sigma'} n_{i,\sigma} n_{j,\sigma'} \tag{86}$$

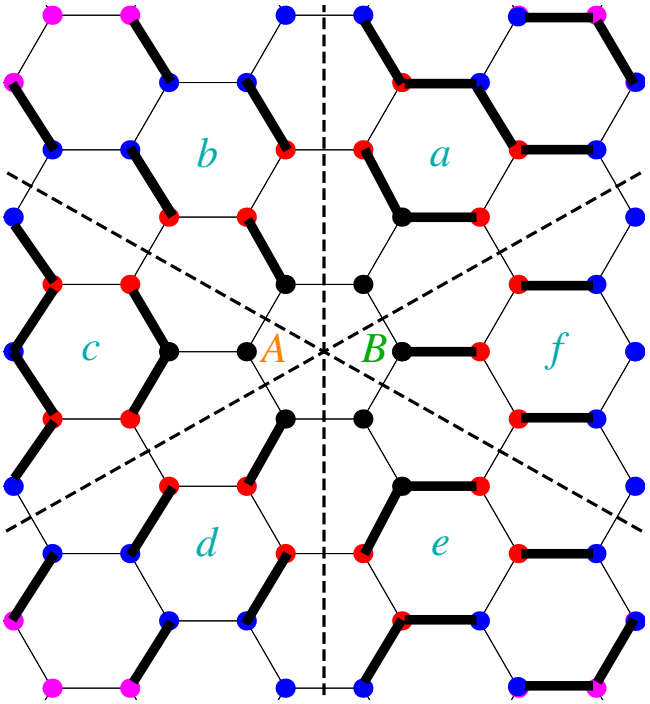

Figure 5: Pictorial representations of the hopping amplitudes defined by $\chi(\mathcal{R})$, an increasing of the minimal number of bonds $\mathcal{R}$ to reach a central hexagon. The bond strength is such that if $\mathcal{R}$ is odd then $\chi(A) > \chi(B)$ else $\chi(A) = \chi(B)$, a strain configuration that can interpolate between approximately homogeneous to inhomogeneous magnetic fields [288]. Sections (a,c,e) and (b,d,f) map into each other under a $2\pi/3$ rotation.

where t_{ij} encodes the strain pattern and $\{U, V_1, V_2\}$ represent the Hubbard on-site, nearest neighbour and next-nearest neighbour repulsion strengths respectively. For spinless fermions at half-filling, inducing a topological phase can be achieved by developing a complex bond expectation value

$$\eta_{\langle\langle i,j\rangle\rangle} = \left\langle c_i^\dagger c_j \right\rangle \in \mathbb{C} \tag{87}$$

that breaks time-reversal symmetry and acts like an order parameter of the Chern insulator state [109, 295]. Being an effective second-neighbour hopping strength, it is the term proportional to V_2 in (86) that it is expected to drive the transition. Indeed, under a mean field decomposition of V_2 and with $U = V_1 = 0$, it was shown that the strain in Fig. 5 and defined by (87) develops $\eta_{ij} \neq 0$ for sufficiently strong $V_2 > V_c \sim t$ [288]. In the cases with non-uniform strains the order parameter is finite in the vicinity of regions with finite pseudo-magnetic field flux.
Spinful fermions allow for other competing orders to emerge, including the spin Hall effect. In this case the on-site Hubbard interaction U favours a spin-polarized ferromagnetic state for small V_2 [293, 296] that can turn, upon increasing V_2, into spin-Hall effect [288, 291]. A nearest neighbour interaction V_1, on the other hand, favours a charge density wave order which restricts the anomalous Hall phase to appear only when U is sufficiently small and $V_2 > V_1$ [296], a situation resembling unstrained half-filled graphene [295, 297, 298]. An interesting open question is whether these topological phases survive to quantum fluctuations [299, 300, 301].

It is worth noting that the effect of including both the pseudo (b) and external (B) uniform magnetic fields on the integer quantum Hall effect in graphene has also been addressed, including the effect of on site U and nearest neighbour V_1 interactions [302, 303]. For $B > b$ and at half-filling, the Freeman splitting due to the real magnetic field will lift the spin degeneracy while interactions are left with the task of lifting the valley degeneracy (either forming a charge density wave or ferrimagnetic order) triggered by the pseudo

flux [287]. The physical effect is a standard quantum Hall conductivity sequence $\sigma_{xy} = ne^2/h$, in sharp contrast with the non-interacting result $\sigma_{xy} = (4n + 2)e^2/h$ with $n \in \mathbb{Z}$ that is a consequence of the valley and spin symmetry of non-interacting electrons. In the strain dominated regime ($b > B$) an alternating sequence between $\sigma_{xy} = 0$ and $\sigma_{xy} = \mp 2e^2/h$ occurs as a function of electron or hole doping. In this case, and similar to the $B = 0$ case discussed above, short range interactions can stabilize quantum spin Hall and anomalous Hall insulators among other ordered phases depending on their relative strengths [303].

4.5.2. Interaction induced magnetic and non-magnetic phenomena in strained graphene

Competing with the topological states described in Sec. 4.5.1, other important interaction induced orders can emerge in different strained graphene configurations.

An important case is that of uniaxial strain [90]. Moderate uniaxial strain is known to deform the low energy graphene spectrum into an anisotropic Dirac cone resulting in an elliptical Fermi surface [8]. The effect of long-range Coulomb interactions in anisotropic Dirac models has been studied (prior to the experimental realization of graphene) in QED_3 theories relevant for cuprate superconductors [304, 305], and was revisited recently within the strain context [306]. The Dirac anisotropy can be parameterized by the ratio of the Fermi velocities along the x and y directions

$$v_y/v_x = 1 + \delta. \tag{88}$$

Within a renormalization group approach, the anisotropy is found to be *irrelevant* in the renormalization group sense if $\delta \ll 1$, i.e. the isotropic Dirac cone is a stable fixed point [304, 305, 306]. When δ is sufficiently strong a quasi one-dimensional excitonic insulator with

$$\langle \psi_A^\dagger \psi_A - \psi_B^\dagger \psi_B \rangle \neq 0 \tag{89}$$

appears to be the leading instability [306]. Furthermore, uniaxial strain can also affect the onset of the ferromagnetic instability of neutral unstrained graphene under the long range Coulomb interaction [307], driving the instability to smaller couplings within the range of those expected for suspended graphene [308].

Due to its possible experimental relevance, it is important to note that uniaxial strain also alters the screening properties of graphene that are encoded in the dielectric function $\varepsilon(\vec{q}, i\omega)$ at finite frequency (ω) and momentum ($\vec{q}$). In the random phase approximation it is given by

$$\varepsilon(\vec{q}, i\omega) = 1 - V_C(\vec{q})\Pi^{(1)}(\vec{q}, i\omega) \tag{90}$$

Here $V_C(\mathbf{q}) \propto 1/q$ is the bare Coulomb interaction and $\Pi^{(1)}(\mathbf{q}, i\omega)$ is the one loop polarization function. For all $(\mathbf{q}, i\omega)$, the latter quantity can be read off from the result in massless quantum electrodynamics (c.f. Eq. (2.14) in [275]). The effect of uniaxial strain is apparent by restoring the dependence on the anisotropic Fermi velocities

$$\Pi^{(1)}(\vec{q}, i\omega) = -\frac{N}{16 v_x v_y} \frac{v_x^2 q_x^2 + v_y^2 q_y^2}{\sqrt{v_x^2 q_x + v_y^2 q_y + \omega^2}} \tag{91}$$

where $N = 4$ is the number of fermion flavours (one for each spin and valley). The effect of such strain on $\varepsilon(\vec{q}, i\omega)$ permeates into the behaviour of the van der Waals forces between strained graphene sheets, that can be shown to increase with increasing strain anisotropy [309]. Through a renormalization group calculation it was shown that, for large separations between undoped strained graphene sheets, the inclusion of electron–electron interactions reduces the van der Waals interaction between graphene sheets [309].

For interacting graphene in a uniform pseudo-magnetic field, the different ordered phases resulting from Coulomb long-range interaction, on-site U, nearest neighbour V_1 and next nearest neighbour interaction V_2 have been extensively studied [293, 296, 288, 291, 310] and discussed in Sec. 4.5.1. From first principles however, [311] it is estimated that U is the largest energy scale, which, if strong enough would in principle favour a spin-ferromagnet [293, 291, 296]. However, with mean-field theory and Monte-Carlo simulations

it was found that, for finite samples, the system develops a global anti-ferromagnet with zero magnetization [310]. Although locally this state is ferromagnetically ordered, it displays a magnetization that changes sign between the bulk and the edges precisely to deliver a zero total magnetization. This is ultimately tied to the fact that although in an infinite system the support of the zero-modes is restricted to one sub-lattice (say A), in a finite system there is support for these also in sub-lattice B but only at the edges. The magnetization, being tied to the zero modes, changes sign as the support of the modes changes from A (bulk) to B (edge) keeping the total magnetization zero.
To conclude this part we note that long-range Coulomb interactions can reduce the stability of edge states resulting from strain [312]. On the other hand an on-site repulsion together with uniaxial strain can lead to edge-ferromagnetism [313].

4.5.3. Superconductivity in interacting strained graphene

We finish this section devoted to interactions with a note regarding superconducting states in strained graphene induced by attractive interactions. As mentioned above, a spin-triplet superconducting state was shown to exist via exact diagonalization in strained graphene [293] with a finite superfluid density

$$n_s = \frac{1}{2}\frac{\partial^2 E_g}{\partial \theta^2},$$

calculated from the variation of the energy of the ground-state E_g upon twisting the boundary conditions an angle θ [314]. Moreover, strain can lead to interesting superconducting states in graphene [315, 316]. In particular, an exotic $f + is$ superconducting state that spontaneously breaks time-reversal symmetry is expected to occur when attractive on site U and second nearest neighbours interactions V_2 are comparable ($U \sim V_2$) [316]. This state ultimately originates from the competition between the U favoured singlet s-wave pairing and the V_2 favoured triplet f-wave pairing.

4.6. Optical properties of strained graphene

The analysis of light scattered inelastically by graphene by means of Raman spectroscopy has long since become one of the standard characterization techniques in graphene research [317]. We give a brief account of the effect of strain on graphene's Raman spectrum in Sec. 4.6.1. However – and not surprisingly for an atomically thin structure – the interaction between graphene and light is weak within a broad band of frequencies, and elastic scattering is the by far dominant process underlying most of the potential applications of graphene in optical devices [14, 16, 318, 319]. Thus the optical properties of graphene are mainly determined by its electronic structure, which is sensitive to strain. In particular, it has been proposed to use uniaxial strain to break the optical anisotropy of two-dimensional graphene, thus converting it into a dichroic material (see Sec. 4.6.2). Finally, graphene's magneto-optical properties, of which, in particular, a large Faraday effect has attracted attention recently [15, 16], are determined by the nonlinear Landau level spectrum of massless Dirac Fermions. As a zero-field quantum Hall effect and Landau level formation in graphene can be realized with strain-induced pseudomagnetic fields [57, 59], the interplay between real and pseudomagnetic fields in graphene based optical devices seems to offer interesting possibilities for future applications, on which we comment in Sec. 4.6.3.

4.6.1. Strain monitoring with Raman spectroscopy

Raman spectroscopy typically uses light in the infrared (IR) or near ultraviolet (UV) spectral range. Because the laser energy is large compared to the phonon energy, the scattering mechanism involves electronic excitations in intermediate states, rather than direct photon-phonon coupling. Thus, apart from providing information about the phonon spectrum, Raman spectroscopy can also shed light on the behaviour of electrons [320] and complement transport measurements. As tensile strain usually results in phonon softening (and the opposite for compressive strain), Raman spectroscopy provides a tool for strain monitoring.

The Raman spectrum of defect-free single layer graphene is characterized by two peaks: The G peak, which corresponds to the excitation of a phonon in the doubly degenerate in-plane optical mode E_2 (see

Table 2), and the 2D peak, due to a two-phonon process which involves scattering of electron-hole pairs between neighbouring Dirac cones [321].

Under uniaxial strain, graphene's E_2 mode splits into two components $E_2^{\pm}$, which are perpendicular and parallel to the strain axis, respectively. As the E_2^+ mode experiences less softening due to tensile strain, the Raman G peak is seen to split into a G^+ and a G^- band [322, 317]. Both redshift with increasing strain, and their splitting increases. Polarized measurements of the $G^{\pm}$ intensities allow the determination of the crystallographic orientation with respect to a known strain axis. If the uniaxial strain is applied along zigzag or armchair directions, the 2D peak likewise splits into two distinct submodes [320]. Magnitude and polarization dependence of the mode splitting was found to be consistent with the strain-induced motion of the Dirac cones predicted by tight binding calculations [90].

In surface enhanced Raman spectroscopy, photonic structures supporting plasmon resonances (such as arrays of metallic nanoparticles), are deposited on graphene. The strong electromagnetic nearfield associated with the plasmon can increase the intensities of graphene's Raman spectrum by several orders of magnitude [323]. In turn, the Raman spectrum of graphene serves as a detection channel for plasmonic field enhancement. With graphene placed on top of a photonic cavity structure, the slight sagging in the suspended areas locally strains the graphene membrane. The resulting phonon mode softening allows to distinguish between enhanced Raman signals originating from strained and unstrained areas. Thus the strained graphene membrane can be used as a probe that locally resolves the plasmonic field enhancement of photonic structures [324].

4.6.2. Optical properties of uniaxially strained graphene

Elastic (Rayleigh) scattering of light by graphene can be described by the Fresnel equations for a thin film with an appropriate sheet conductivity $\sigma(\omega)$ [325, 326]. For normal incident light of frequency ω, this yields

$$A(\omega) = 1 - |t(\omega)|^2 - |r(\omega)|^2 = \frac{4\sigma(\omega)/(\varepsilon_0 c)}{[2 + \sigma(\omega)/(\varepsilon_0 c)]^2} \tag{92}$$

for the absorbance $A(\omega)$ of free standing graphene, where r and t denote the Fresnel coefficients for reflection and transmission, respectively, c is the speed of light and ε_0 the vacuum permittivity.

Modelling the graphene charge carriers as non-interacting, massless fermions in the Dirac-cone approximation yields a universal conductivity of $\sigma = e^2/(4\hbar)$ for all $\omega > 2E_F/\hbar$ [327, 328]. When inserted into Eq. (92), this results in $A = \pi\alpha + \mathcal{O}(\alpha^2) \simeq 2.3$ (where $\alpha = e^2/(4\pi\varepsilon_0\hbar c)$ is the fine-structure constant) which corresponds to the experimental value observed at wavelengths between 450 nm and 4.2 μm [329, 330]. At energies below $2E_F$, graphene supports collective plasmon oscillations, which can be described by treating electron-electron interactions within the random phase approximation (RPA) [331]. In the long wavelength limit $\hbar\omega \ll 2E_F$, the plasmon dispersion reads

$$\omega(\vec{k}) = \left(2\alpha c k E_F/\hbar\right)^{1/2} \tag{93}$$

[332, 333, 13]. For typical graphene-on-substrate samples, E_F is of the order of 0.5 eV or lower. This fixes the application range of graphene plasmonics to the THz and mid-IR band (wavelengths $\geq 1\,\mu$m), while graphene based optical broadband applications can operate in in the near-IR and most of the visible spectrum (wavelengths between 450 and 1 μm) [14].

The effect of uniaxial strain on graphene's optical conductivity can be described by introducing strain dependent hopping parameters into the standard tight binding Hamiltonian [91, 90], which deforms the Fermi surface into an ellipse (see also Sec. 2.3). This defines a fast and a slow optical axis, with the latter (and, correspondingly, a lowered conductivity) oriented closely along the direction of strain. The frequency independence of absorption in the near-IR and visible range stays intact under uniaxial strain, but the absorbance of linearly polarized light now depends on the polarization direction ϕ_I with respect to the slow optical axis [89],

$$A \approx \pi\alpha[1 - 2a|\delta k_D| \cos 2\phi_I], \tag{94}$$

and the degree of polarization dependence is determined by the strain-induced shift $\delta k_D = \epsilon\lambda_s(1+\nu)/2$ of the Dirac points from their position at $\vec{K}, \vec{K}'$ in the Brillouin zone. Here ϵ denotes the magnitude of applied strain, $\nu \approx 0.16$ is graphene's Poisson ratio, and $a\lambda_s \approx$ 3-4 [91]. The periodic modulation (94), measured in the transmission of visible light through bended graphene [334], allows for an optical detection of magnitude and orientation of uniaxial strain, with possible applications in passive, atomically thin, and flexible strain sensors. A reduced optical absorption along the direction of strain was likewise observed in the Drude response of uniaxially strained graphene at far-IR wavelengths of $\lambda =$ 30-300 μm [335]. Importantly, the conductivity modulations resulting from tensile strain up to nearly 20% have been shown to be reversible [336, 334].

The square root character of the plasmon branch [Eq. (93)] as well as its $n^{1/4}$ dependence on the charge density are not changed by uniaxial strain. However, corresponding to the strain dependence obtained for the optical conductivity and the resulting absorption in Eq. (94), the plasmon dispersion gets steeper for $\vec{k}$ perpendicular to the direction of strain and is flattened for wavevectors along the strain direction, with the amplitude of the modification proportional to ϵ [337]. In a similar fashion, the effect of scalar and vector potentials with one-dimensional periodicity [that is, $V_s = V_s(x)$, $\vec{\mathcal{A}}^{el} = \vec{\mathcal{A}}^{el}(x)$], induced by periodic strain waves, was found to render the low-energy part of the plasmon dispersion anisotropic [338]. Further, uniaxial strain (via its effect on the electron-electron interaction) is expected to modify the electron-plasmon scattering structures which are visible near the Dirac points in ARPES studies [339].

For realistic values of $\epsilon \leq 20\,\%$, and in contrast to non-uniform strain configurations (as discussed in Secs. 2.3 and 5), uniaxial strain is not expected to open a gap (resulting in a vanishing optical conductivity) in extended two-dimensional graphene [90]. However, tight binding calculations for graphene nanoribbons predict that realistically small uniaxial strain results in a periodic modulation of the bandgap in armchair ribbons, while in zigzag ribbons it creates a band gap proportional to the magnitude of applied tensile strain [340]. As the band-structure is modified, the optical transition energies between maxima of occupied bands and minima of unoccupied bands change, resulting in a shift of the maxima in the optical loss-function $Z(\omega) = [\mathrm{Im}\,\varepsilon(\omega)]^{-1}$ [341].

4.6.3. Magneto-optics with strained graphene

As in the magnetically unbiased case, the transmission of light through a graphene layer in the presence of a uniform external magnetic field can be described within the Fresnel formalism [342], with the Fresnel coefficients for reflected and transmitted amplitudes now being functions of both graphene's diagonal and Hall conductivity. Analytical expressions for σ_{xy} and σ_{xx} as functions of frequency and magnetic field have been derived in Refs. [343, 344]. Due to the action of the magnetic field on the conduction electrons, an incident beam of linear polarization along the x-direction will, after passing the graphene layer, consist of both x and y components. The total transmission T through biased graphene is a sum of the intensities in both polarizations, and for an incident beam oriented normal to the surface of suspended graphene, we arrive at [345, 16]

$$T(\omega) = |t_{xx}|^2 + |t_{xy}|^2 = 1 - \frac{\mathrm{Re}\,\sigma_{xx}(\omega)}{\varepsilon_0 c} + \mathcal{O}(\alpha^2). \tag{95}$$

Due to the non-equidistant spacing of graphene's Landau levels, the transmission spectrum Eq. (95), as observed by IR spectroscopy [346, 347], displays resonant dips at frequencies where the incident light can excite electronic transitions between Landau levels $E_n = \pm v_F\sqrt{2e\hbar Bn}$ (where $n = 0, 1, 2, \dots$). Calculations using density-functional theory based tight-binding theory (DFTB) predict that the same Landau level spectrum can be obtained at zero external field by twisting graphene nanoribbons with several hundreds of nanometres width [348]. The strain produced by twisting the ribbon around its axis results in a pseudomagnetic field $\vec{B}_s^K = -\vec{B}_s^{K'} \simeq \gamma^2 x$ (where γ denotes the twist rate, and $|x| \leq W/2$ the coordinate perpendicular to the ribbon axis) that changes sign when going from one ribbon edge to the other. The resulting electronic DOS for zig-zag as well as armchair ribbons is predicted to mimic Landau quantization of Dirac fermions in magnetic fields up to 160 T.

For graphene, the Faraday effect (and the related Kerr effect), in which linearly polarized light transmitted through (or reflected by) a material in the presence of a magnetic field has its polarization plane rotated, is surprisingly strong: monolayer graphene in modest fields has been found to turn the polarization by several degrees [15, 16, 345, 342]. With the incident beam as well as the external magnetic field oriented perpendicular to the surface of suspended graphene, we arrive at a Faraday rotation angle [15, 345]

$$\theta_F(\omega) = -\frac{1}{2}\frac{\mathrm{Re}\,\sigma_{xy}(\omega)}{\varepsilon_0 c} + \mathcal{O}(\alpha^2). \tag{96}$$

θ_F is large for frequencies where σ_{xy} shows resonances. In the classical cyclotron resonance regime, this occurs for $\omega \simeq v_F^2|eB/E_F|$, while in the quantum Hall regime, laser frequencies matching the transition energies between two Landau levels lead to large Faraday angles [15].

The Faraday and Kerr effects are of technological importance in the development of optical diodes and other non-reciprocal optical elements [349]. For these magneto-optical applications, graphene offers a great potential because Landau-level formation and a nondiagonal optical conductivity in graphene can be obtained either by applying an external magnetic field or through strain-induced pseudomagnetic fields [350, 303]. With an additional strain-induced pseudomagnetic field B_s, electrons in the $\vec{K}$ and $\vec{K}'$ valleys are exposed to an effective field $B_{\mathrm{eff}} = B \pm B_s$, respectively [350, 303]. An effect of pseudomagnetic fields on the Faraday rotation is thus possible at frequencies where the contributions to σ_{xy} resulting from the two inequivalent valleys do not cancel out in Eq. (96). For $\hbar\omega \ll E_F$, the overall dependence of $\sigma_{xy}(\omega)$ on the effective field scales as B_{eff}^{-1} [343, 344], which opens possibilities for a strain-induced Faraday rotation in the THz band.

5. Superlattices

The properties of misaligned graphene multilayers and graphene deposited on other two-dimensional crystals have been the subject of intense research recently. The simplest of these, twisted bilayer graphene, exhibits different stackings (local atomic alignments between layers) when the two layers are rotated relative to each other by a finite angle θ [351, 352, 353]. Such a rotation gives rise to a periodic spatial modulation of the stacking, known as a Moiré pattern or stacking superlattice, with a period that goes as $\sim a/\theta$ at small θ. All sorts of interesting electronic reconstructions arise from the stacking modulation, including low-energy van-Hove singularities, secondary Dirac points away from charge neutrality and Hofstadter butterflies [354, 355, 356, 357, 358, 359]. These reconstructions can be understood as the consequence of non-Abelian gauge fields that emerge in the low energy sector of the system [360], similarly to the Abelian pseudogauge fields associated to strains in a graphene monolayer.

Together with the modulated stacking, a rather strong modulation of the local inter-layer adhesion energy density develops in the twisted bilayer. The inhomogeneous adhesion creates a surprisingly strong strain modulation in the system, whereby the areas with the preferred stackings (AB, or Bernal stacking, with higher adhesion) become expanded at the expense of other regions. This transforms the Moiré patterns into a characteristic hexagonal mesh of stacking solitons (linear stacking faults, around ~ 10 nm wide), usually with the same period as the original (unrelaxed) Moiré [351]. Once more, a range of intriguing electronic effects emerge from the soliton strain fields, e.g. the development of a helical network of states carrying valley currents along the solitons when the bilayer is placed under a perpendicular electric field [361], or the suppression of conductance close to neutrality due to scattering on the solitons [362, 363].

More complicated Moiré structures and inhomogeneous adhesion-induced strains are possible, and even ubiquitous in more complex multilayers [355, 208]. Graphene trilayers, for example, can exhibit ABA and ABC stacking domains, visible with Raman spectroscopy [364], and separated by compressed stacking solitons. Unlike in the bilayer, these two types of stackings, despite being very close in energy, are electronically very different. In particular, ABA domains remain metallic under large out-of-plane electric fields, while ABC domains develop a sizeable gap. This enables all-electric manipulation of stacking domains in the trilayer, and of their elastic soliton boundaries, using a biased STM tip [365]. These examples clearly show that the spatial modulation of stacking alignment in graphene multilayers creates a fascinating playground

where elasticity and electronic structure become strongly coupled, and where quite a few problems remain open [366, 367].

But stacking Moiré superlattices are not restricted to graphene multilayers. A simple graphene monolayer grown or deposited over different insulating crystals such as SiC and hBN also exhibits Moiré patterns, stacking solitons and a remarkable electronic structure. High quality samples with outstanding transport properties are provided by these setups (cf. Sec. 4.1), and other heterostructures, with [17, 368] or without [369] graphene as one of their building blocks. Due to their current interest, we will now review in more detail the physics of graphene/hBN structures, as a representative of this class of hybrid Moiré superlattices.

Superlattices arise in this context due to the superposition of 2D crystals with different periodicities, stackings and/or alignments. To study their electronic band structure, at least two aspects must be considered. First, the deformation of the layers' pristine periodicity that may take place spontaneously due to Van der Waals adhesion potentials, which drives the multilayer into a non-trivial equilibrium configuration. Second, the electronic coupling between layers in this new scenario, usually regarding the derivation of an effective description.

The Frenkel-Kontorova model addresses the first issue, namely to study the ground state of a system where a substrate potential and the elastic energy of a 1D or 2D lattice compete.[370, 371, 372, 22] It exhibits three possible ground state phases, depending on the relative periodicities of the lattices and the ratio of adhesion versus elastic energy: (i) a generalized floating phase, where there are only local deformations due to a weak interaction with the substrate, the Moiré pattern preserving its undeformed periodicity; (ii) a commensurate phase, where there is a modified overall periodicity of the Moiré pattern, resulting from a finite global deformation; (iii) an incommensurate phase, characterized by the presence of aperiodic solitons, and separating two commensurate phases as a function of lattice mismatch.

These three phases have been experimentally encountered in a variety of heterostructures containing graphene. For a twisted bilayer, Ref. [351] observed, in different regions of the sample, both commensurate structures with hexagonal symmetry and the structural solitons. For graphene over hBN, Ref. [260] reported a phase transition between a commensurate structure and a floating phase as the Moiré period exceeds $\sim 10\,\mathrm{nm}$.[3] Fig. 6 is a reproduction of this experimental evidence, with the Young modulus FWHM over the Moiré wavelength as the order parameter.

Determining the strain field that carries the system to its ground state is the first issue to be addressed. The application of the Frenkel-Kontorova model to two dimensions is not trivial, since it demands the use of a complex mathematical machinery,[371, 370] as well as an accurate knowledge of the shape of the adhesion potential. To predict theoretically the deformation in this framework is, therefore, a difficult task.

A first strategy to tackle this problem consists on focusing solely on floating-phase deformations, namely strain superlattices with the same periodicity as the Moiré pattern. We consider here the simple case of a bilayer. Then, such deformations conform minimal commensurate configurations with reciprocal superlattice generating vectors[373, 374, 375, 376]

$$\vec{G}_j = \vec{g}_j - \vec{g}'_j. \tag{97}$$

Vectors $\vec{g}_j$ and $\vec{g}'_j$ are the reciprocal lattice generating vectors of each of the two crystals, chosen such that the $|\vec{G}_j|$ are minimal. A sketch of this construction for graphene on hBN (honeycomb lattices with a finite mismatch and a relative rotation) is shown in Fig. 7. $\vec{G}_j$ are often referred to as "first star" vectors when dealing with hexagonal symmetry.

The reciprocal vectors $\vec{G}_j$ and the corresponding superlattice vectors $\vec{A}_j$ define a superlattice that may or may not be commensurate with each of the two layers. In the incommensurate case, no true periodicity of the bilayer exists, and the basic tenet of Bloch's theorem cannot be invoked when considering electronic structure. It has been shown, however, that for a small value of the graphene lattice constant a over the interlayer distance d, incommensurability and exact commensurability yield the same observable electronic

[3] The notation in Ref. [260] differs from the customary denominations in the Frenkel-Kontorova framework: they refer to the floating phase as incommensurate, in the sense that the top layer does not conform to the substrate. They disregard what in this review we call incommensurate phases, since no aperiodic solitons are observed.

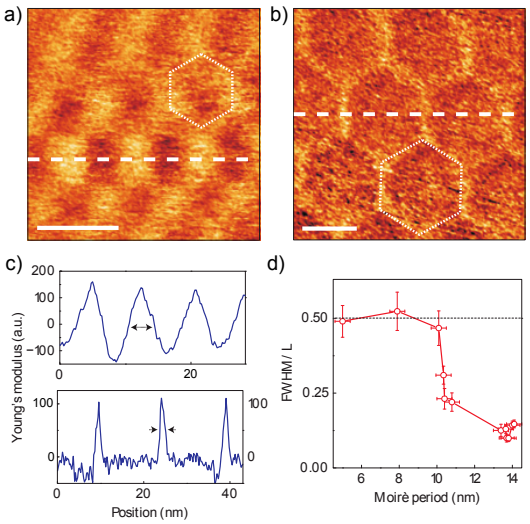

Figure 6: (a) and (b): the Young modulus distribution, measured by AFM, for structures with 8 and 14nm Moiré patterns, respectively. Scale bars are 10 nm long. (c): Cross-sections of the Young modulus distribution taken along the dashed lines in (a) (top) and (b) (bottom). (d): Ratio between the full width half maximum (FWHM) of the peak in the Young modulus distribution (as marked by arrows in (c)) and the period of the Moiré structure L, as a function of the period of the Moiré structure for several samples. Reproduced from Ref. [260] with permission of the authors.

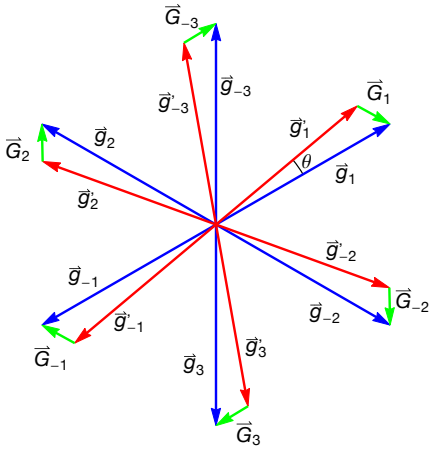

Figure 7: Shortest reciprocal lattice generating vectors of two misaligned honeycomb lattices (red and blue) and of the resulting superlattice (green).

properties.[377] It is then legitimate to approximate any system with $a/d \to 0$ as a commensurate structure with a reciprocal superlattice generated by Eq. (97). This is known as the continuum approximation, and allows one to consider the concept of a low energy band structure assuming an effectively periodic superlattice, even though Bloch's theorem does not apply at the smallest length scales. Considering in-plane deformations $\vec{u}(\vec{r})$ with the same periodicity (floating phase approximation, with purely local deformations), one arrives at the simplest nontrivial description of the coupled electronic and elastic properties of these Moiré crystals. In subsequent sections we focus on the continuum approximation approach, which turns out to be enough to describe a number of systems, such as graphene on hBN.

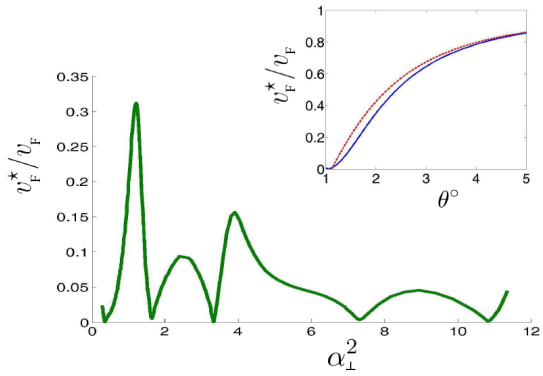

Figure 8: Renormalization of the Fermi velocity in bilayer graphene for small twist angles θ (strong coupling). $\alpha_\perp$ is given in the main text. The inset depicts v_F^*/v_F in the weak coupling regime. Red is respective to Eq. (99), whereas the blue curve corresponds to more accurate numerical calculations. Reproduced from Ref. [373] with permission of the authors.

5.1. Undeformed Moiré superlattices

The first studies of graphene superlattices were restricted to floating phases with zero deformations, very particularly for the case of twisted graphene bilayers. An effective continuum model for unstrained twisted bilayer graphene can be found in Refs. [373, 378, 379]. The Dirac cone structure is preserved, although with a renormalized Fermi velocity v_F^*. For large enough twist angles θ, and at low enough energies, a Dirac model remains valid for carriers in each of the two monolayers, which behave as if decoupled,

$$\mathcal{H}_{\text{eff}} = v_F^* \sum_{\vec{k}} \psi_{\vec{k}}^\dagger \, \vec{\sigma} \cdot \vec{k} \, \psi_{\vec{k}}, \tag{98}$$

Here $\psi_{\vec{k}}^\dagger = (a_{\vec{k}}^\dagger, b_{\vec{k}}^\dagger)$, while $a_{\vec{k}}^\dagger$ ($b_{\vec{k}}^\dagger$) are the creation operator of the $\vec{k}$ Bloch state in the A (B) sublattice. The correction to the Fermi velocity v_F^*/v_F as a function of the twist angle is plotted in Fig. 8. In the weak coupling regime (large relative rotation angles $\theta \gtrsim 1^\circ$),

$$v_F^* \simeq v_F \frac{1 - 3\alpha_\perp^2}{1 + 6\alpha_\perp^2}; \tag{99}$$

where $\alpha_\perp = \frac{t_\perp}{3 v_F k_\theta}$, $t_\perp$ is the nearest neighbour interlayer hopping ($t_\perp \simeq 330\,\text{meV}$), $k_\theta = 2K \sin(\theta/2)$ and $K = 4\pi/3a$ is the modulus of the K-point wavevector.[373] At energies around $v_F^* k_\theta/2$, the decoupled monolayer description breaks down. Carriers from different layers hybridize, giving rise to a θ-dependent van-Hove singularity in the density of states. In contrast with unrotated bilayer graphene, a gap does not open in its twisted counterpart when applying a potential difference between the layers.[379]

As the relative rotation angle θ falls below 1°, the system enters a more complicated strong coupling regime. When neglecting deformations, Dirac cones survive in this regime. However, the corresponding renormalized Fermi velocity becomes much smaller and is even completely suppressed for a set of 'magic' rotation angles, implying a strong enhancement of the density of states at the neutrality point. Ref. [378] also points out the possibility of annihilation and regeneration of Dirac nodes based on the ratios of the Slonczewski-Weiss-McClure parameters, as well as encountering a quadratic dispersion relation near the Fermi energy.

As for graphene over hBN, a floating phase analysis was conducted in Refs. [380, 381]. Not including in plane deformations, *ab initio* calculations suggest a modulation in the distance between layer and substrate (Fig. 9), which in turn results in a gap opening. Interaction between electrons has been shown to enhance this gap to the extent of experimentally measured values ($\sim 30\,\text{meV}$).[380, 382, 383] If, on the other hand, the interlayer distance is assumed constant throughout the system and interactions are neglected, the gap averages to zero without deformations.

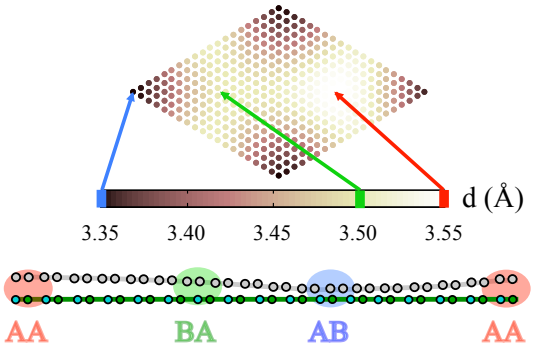

Figure 9: Modulation of the graphene distance to hBN as a function of the stacking according to *ab initio* calculations. With AB (BA) stacking, we refer to one sublattice of graphene overlapping exactly with boron (nitrogen) atoms. Reproduced from Ref. [380] with permission of the authors.

5.2. Spontaneous deformations in the continuum approximation

Strains, such as the spontaneous deformations expected from adhesion interactions with a crystalline substrate, induce significant changes in the electronic structure of graphene.[59, 57] Let us assume a certain purely in-plane deformation, described at $\vec{r}$ by an in-plane displacement $\vec{u}(\vec{r}) = (u_x(\vec{r}), u_y(\vec{r}))$ with respect to its unstrained configuration. The change in hopping integrals arising from said deformations can be recast into the scalar (V_s) and pseudogauge ($\vec{\mathcal{A}}^{el}$) potentials[36] discussed in Sec. 2.3, with the symmetry described by Eq. (8) and yielding the Hamiltonian of Eq. (25).

In the continuum approximation, the influence of the substrate on the electronic structure acts via two mechanisms. First, as pseudopotentials ($V_s, \vec{\mathcal{A}}^{el}$) associated to strains, induced in turn by the adhesion potential. Second, through the electronic coupling with the substrate. To obtain an effective model out of these ingredients one must add the pseudopotentials of Eqs. (19), (20) to a pristine layer, and also integrate out the electronic degrees of freedom of its substrate, which creates a self-energy in the form of a local potential in graphene for strongly insulating substrates.

We will focus on the case of small rotation angles between graphene and a hBN substrate, as it has caught the attention of most part of the recent literature due to the high quality of the ensemble. Since in the continuum approximation we may consider the superlattice to be minimally commensurate for any rotation angle, the deformation field $\vec{u}(\vec{r})$ will be assumed to have the same periodicity as the graphene/hBN Moiré, encoded in $\vec{G}_j$. Furthermore, the bulk substrate will be treated henceforth as undeformable (hBN is assumed to be a thick and rigid crystal). The smoothest possible deformation field $\vec{u}(\vec{r})$ in the superlattice unitary cell thus reads

$$\vec{u}(\vec{r}) = \sum_j \vec{u}_{\vec{G}_j} e^{i\vec{G}_j\cdot\vec{r}}. \tag{100}$$

Since $\vec{u}(\vec{r})$ is real, its harmonics satisfy $\vec{u}_{\vec{G}_j} = \vec{u}^*_{-\vec{G}_j}$. Moreover, the symmetry point group S of the superlattice imposes some more constraints, namely $\mathcal{S}\vec{u}_{\vec{G}_j} = \vec{u}_{\mathcal{S}^{-1}\vec{G}_j}\ \forall \mathcal{S} \in S$. For example, when dealing with $S = C_3$, only the vector $\vec{u}_{\vec{G}_1}$ ($\vec{G}_1$ belonging to the superlattice basis) will be independent in Eq. (100).

Symmetry-based analysis.— Under the foregoing considerations, effective theories dependent on the deformation $\vec{u}(\vec{r})$ have been formulated. A first foray into the computation of the Moiré band structure in the continuum approximation, including deformations, was based on symmetry principles.[375]

For monolayer graphene over a hBN substrate, the Dirac cone at the Fermi energy is preserved. Moreover, due to the folding of the single layer bands over the superlattice 1st Brillouin zone, minibands were predicted to exhibit a combination of three possible features: (i) three mini Dirac points (mDPs) in the conduction or valence band, located at the superlattice 1st Brillouin zone edge with momentum $\hbar v_F G_j/2$; (ii) a single mDP at the $\pm\kappa_{\text{super}}$ point (which is analogous to graphene's K point but respective to the superlattice);

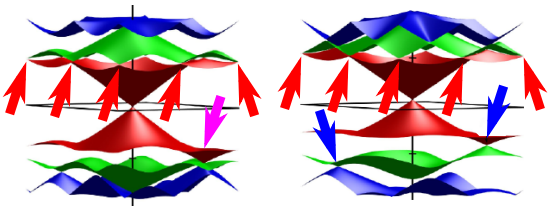

Figure 10: Band structure for different choices of the parameters calculated in Ref. [375]. Red, blue and magenta arrows point to multiple, single mDPs and triple degenerate band crossings, respectively. Reproduced with permission of the authors.

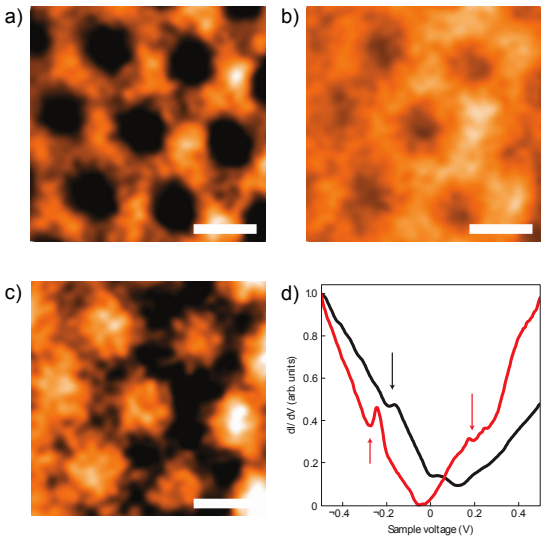

Figure 11: Experimental LDOS for energies close to valence mDPs (a), to the main Dirac point (b) and to conduction mDPs (c) in a sample with a 13.4 nm period. The scale bars in all images are 10 nm long. (d): Measured dI/dV (proportional to the DOS) with arrows pointing to the dips respective to mDPs. Red (black) corresponds to a 13.4 nm (9.0 nm) Moiré wavelength. Plots were extracted from Ref. [376] with permission of the authors.

(iii) a triple degenerate band crossing. Examples of band structures where (i)-(iii) are encountered appear in Fig. 10.

In agreement with these calculations, mDPs were observed in Ref. [376] at energies between 0.2 and 1 eV by means of STM measurements. Dips in dI/dV curves like the ones reproduced in Fig. 11 are their main signature. The predicted electron hole asymmetry comes from the interaction with the substrate, although next-nearest neighbour hopping could also contribute to it. Further experimental evidence of mDPs could be extracted from (far) infrared spectra, where dissimilarities with respect to suspended graphene's constant conductivity would show up; or by Hall coefficient measurements, which would vary non monotonically upon doping with electrons or holes.

As for the dispersion relation pinned to mDPs described in (i), further analysis shows that it is anisotropic with a new Fermi velocity[376]

$$v_F(\theta) = \sqrt{\left(v_F \cos\delta\theta\right)^2 + \left[V \sin\delta\theta/(2\hbar G_j)\right]^2}. \tag{101}$$

Here, $\delta\theta$ is the angle between $\vec{G}_j/2$ and $\delta\vec{k} = \vec{k} - \vec{G}_j/2$, and V is the first star amplitude of the adhesion potential Fourier expansion.

Bilayer graphene over hBN was featured in Ref. [374] using a similar approach. mDPs also appear

in this system, although the presence of a single cone is rare. As a new feature, gaps between the first Moiré miniband and the rest of the spectrum are common in this case. The dependence of the spectra on the rotation angle is now enhanced with respect to single layer graphene due to higher trigonal warping corrections.

Microscopic derivations of spontaneous deformations.— A step beyond the symmetry-based approaches described above was recently taken,[262] and specific values for the spontaneous deformations $\vec{u}_{\vec{G}_j}$ were predicted as a function of the relative rotation angle between layers. From this, the specific form of the low energy electronic model was also computed.[384] This program requires the knowledge of the adhesion potential V_S, whose spatial periodicity is given by that of the substrate, and its amplitude modulation is parameterized by adhesion energy differences $\Delta\epsilon_{AB} = \epsilon_{AB} - \epsilon_{AA}$ and $\Delta\epsilon_{BA} = \epsilon_{BA} - \epsilon_{AA}$. Here ϵ_{ij} denotes the adhesion energy per graphene unit cell for local ij stacking. The stacking notation is AA for perfectly aligned hexagonal lattices, AB for Carbon-on-Boron and BA for Carbon-on-Nitrogen Bernal stackings. The values of the different adhesion energies ϵ_{ij} can be extracted from *ab initio* calculations,[380, 385, 381, 386] which almost invariably predict a stronger adhesion for AB-stacking. Ref. [262] constructs a first star adhesion potential corresponding to a given $\Delta\epsilon_{BA}$ and $\Delta\epsilon_{AB}$

$$V_S(\vec{r}) = \sum_{j=\pm1}^{\pm3} v_j\, e^{i\vec{g}'_j\cdot\vec{r}} + v_0; \tag{102}$$

$$v_{j>0} = v^*_{j<0} = -\frac{\Delta\epsilon_{AB} + \Delta\epsilon_{BA}}{18} + i\frac{\Delta\epsilon_{AB} - \Delta\epsilon_{BA}}{6\sqrt{3}}; \tag{103}$$

$\vec{g}'$ belonging to the reciprocal lattice of hBN. The uniform offset $v_0 = (\epsilon_{AB}+\epsilon_{BA}+\epsilon_{AA})/3$ may be disregarded in the following. In the continuum limit, the total adhesion energy can be written as

$$U_S = \frac{1}{\Omega_S}\int_{\Omega_S} d^2\vec{r}\,\tilde{V}_S[\vec{r},\vec{u}(\vec{r})]; \tag{104}$$

$$\tilde{V}_S[\vec{r},\vec{u}(\vec{r})] = \sum_{j=\pm1}^{\pm3} v_j\, e^{-i\vec{G}_j\cdot\vec{r}} e^{i\vec{g}'_j\cdot\vec{u}(\vec{r})}. \tag{105}$$

Ω_S is the area of the superlattice unit cell. The linear distortion regime may be considered,

$$\tilde{V}_S[\vec{r},\vec{u}(\vec{r})] \simeq \tilde{V}_S[\vec{r},0] + \vec{u}(\vec{r})\cdot\partial_{\vec{u}}\tilde{V}_S[\vec{r},\vec{u}(\vec{r})]\big|_{\vec{u}=0}, \tag{106}$$

This approximation allows us to compute analytically an equilibrium deformation by minimizing the adhesion energy U_S plus the elastic energy due to in-plane distortions $F_{\rm st}^{\text{in-plane}}$ (see below), and can be shown to be legitimate, since the inclusion in Eq. (106) of higher order terms in $\vec{u}(\vec{r})$ does not significantly modify the result.[262]

The elastic energy $F_{\rm st}^{\text{in-plane}}$ prevents the layer from conforming completely to V_S. According to continuum elasticity theory, the elastic energy due to in-plane stretching, $F_{\rm st}^{\text{in-plane}}$, for an isotropic medium is obtained from Eq. (10) by replacing the strain tensor u_{ij} by the linear strain tensor $u_{(i,j)}$,

$$\begin{aligned} F_{\rm st}^{\text{in-plane}} &= \frac{1}{2}\int d^2\vec{r}\left(\lambda u_{(i,i)}^2 + 2\mu u_{(i,j)}u_{(i,j)}\right) \\ &= \frac{1}{2}\sum_{\vec{q}} \vec{u}_{-\vec{q}}\cdot\underline{W}_{\vec{q}}\cdot\vec{u}_{\vec{q}}, \end{aligned} \tag{107}$$

with

$$\underline{W}_{\vec{q}} = (\lambda+2\mu)\Omega_g\underline{W}^{\parallel}_{\vec{q}} + \mu\,\Omega_g\underline{W}^{\perp}_{\vec{q}}, \tag{108}$$

$$\underline{W}^{\parallel}_{\vec{q}} = \begin{pmatrix} q_x^2 & q_xq_y \\ q_xq_y & q_y^2 \end{pmatrix},\ \underline{W}^{\perp}_{\vec{q}} = \begin{pmatrix} q_x^2 & -q_xq_y \\ -q_xq_y & q_y^2 \end{pmatrix}. \tag{109}$$

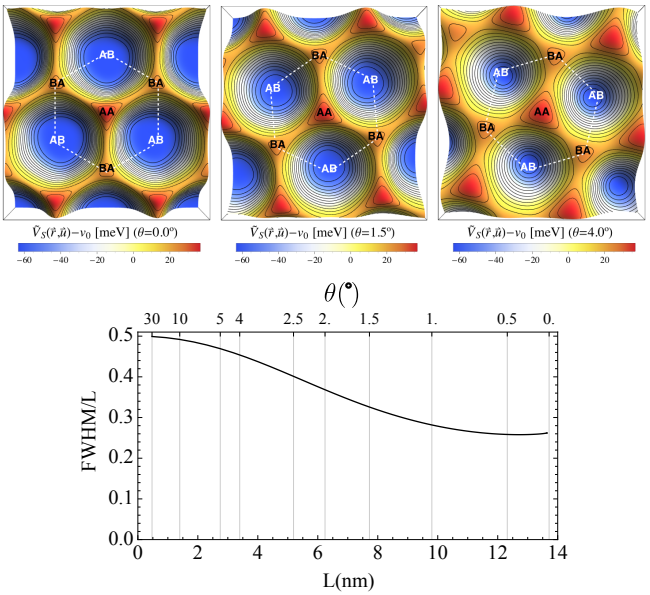

Figure 12: TOP: Adhesion energy density $\tilde{V}_S[\vec{r},\vec{u}(\vec{r})]$ in real space, relative to the average adhesion ν_0. The rotation angles are $\theta = 0$ (left), $\theta = 1.5°$ (middle) and $\theta = 4°$ (right). BOTTOM: Theoretical FWHM of a section of the deformation profile as a function of the rotation angle or Moiré period.

Ω_g, analogous to Ω_S, corresponds to the area of the graphene unit cell. λ and μ are the Lamé constants.

The minimization of the total energy of the lattice, $U = F_{\rm st}^{\text{in-plane}} + U_S$, with respect to the parameters $\vec{u}_{\vec{G}_j}$ yields the equilibrium configuration,

$$\vec{u}_{\vec{G}_j} = iv_j^* \underline{W}_{\vec{G}_j}^{-1} \cdot \vec{g}'_j. \tag{110}$$

Fig. (12) plots the resulting adhesion energy $\tilde{V}_S[\vec{r},\vec{u}(\vec{r})]$ for different relative rotation angles. It is expected to be representative of the Young modulus measured in Ref. [260]. A good qualitative agreement is achieved with experiments (see Fig. 6): greater angles give rise to configurations close to an undeformed floating phase, whereas a small twist drives the system to sharper deformations without a global expansion or contraction (a 'generalized' floating phase). The inclusion of e.g. global deformations as additional degrees of freedom could be considered, but remain unexplored. Other works have studied also the role of out of plane instabilities.[382] These could account for quantitative differences with experimental results, noticeable in particular in the normalized width of stacking solitons FWHM/L for long Moiré periods. In fact, an abrupt jump at $L \sim 10\,$nm was reported therein that is not reproduced by the linear deformation model described here. Interestingly, however, some conflicting results exist in this regard, with e.g. Ref. [387] reporting no evidence of such discontinuity in electronic observables.

Microscopic derivations of effective electronic model.— Once an equilibrium deformation solution such as Eq. (110) has been established, and bearing also Eqs. (19),(20) in mind, an effective low energy Hamiltonian may be derived microscopically for graphene on the crystalline substrate, which has the advantage over symmetry-based approaches of predicting specific values of all model parameters. The first step involves writing a low energy model including graphene and hBN degrees of freedom,

$$\boldsymbol{H} = \begin{pmatrix} \boldsymbol{H}_{\rm gr}\left[\vec{k} - \frac{1}{2}\Delta\vec{K} - \frac{e}{\hbar}\vec{\mathcal{A}}^{el}(\vec{r})\right] + \boldsymbol{V}_s(\vec{r}) & \tilde{\boldsymbol{T}}^{\dagger}(\vec{r}) \\ \tilde{\boldsymbol{T}}(\vec{r}) & \boldsymbol{H}_{\rm hBN}\left(\vec{k} + \frac{1}{2}\Delta\vec{K}\right) \end{pmatrix}; \quad \boldsymbol{H}_{\rm hBN} \simeq \boldsymbol{\Delta}_{\rm hBN} = \begin{pmatrix} \epsilon_v & 0 \\ 0 & \epsilon_c \end{pmatrix}. \tag{111}$$

$\boldsymbol{H}_{\rm gr}$ denotes the Hamiltonian of monolayer graphene and $\boldsymbol{H}_{\rm hBN}$ corresponds to a single layer of hBN, that is approximated by a perfect insulator. ϵ_v (ϵ_c) are the energies of its valence (conduction) band. $\tilde{\boldsymbol{T}}(\vec{r})$ is the interlayer hopping taking deformations in the linear regime into account,[384] and $\Delta\vec{K}$ joins the Dirac point of pristine graphene with the analogous in hBN. hBN orbitals can then be integrated out of Eq. (111) exactly, which results in a local self energy,

$$\boldsymbol{\Sigma}(\vec{r}) \approx -\tilde{\boldsymbol{T}}^{\dagger}(\vec{r})\boldsymbol{\Delta}_{\rm hBN}^{-1}\tilde{\boldsymbol{T}}(\vec{r}) \tag{112}$$

that must be added to $\boldsymbol{H}_{\rm gr}$. Together with the induced pseudopotentials $(V_s, \vec{\mathcal{A}}^{el})$, the final effective Hamiltonian reads[384]

$$\boldsymbol{H}_{\rm eff} = \boldsymbol{H}_{\rm gr}\left[\vec{k} - \frac{e}{\hbar}\vec{\mathcal{A}}^{el}(\vec{r})\right] + \boldsymbol{V}_s(\vec{r}) + \boldsymbol{\Sigma}(\vec{r}). \tag{113}$$

Ref. [384] focuses on unrotated graphene over hBN, explicitly spelling out Eq. (113) after decomposing all contributions in terms of $\vec{\sigma}$ matrices, and into spatially symmetric and antisymmetric components. Every harmonic beyond the first star may be neglected in the model. The solution depends solely on dimensionless parameters z_u (maximum difference in local relative expansion between different regions, see Ref. [384]), $m_{\pm}$ (associated to the hBN gap and the interlayer hopping $t_{\perp}$), g_1 [energy scale of the deformation potential, Eq. (19)] and g_2 [relating strains to pseudomagnetic fields, Eq. (20)].

The electronic spectrum, density of states (DOS) and local density of states (LDOS) were analysed as a function of strains, hopping to hBN, V_s and $\vec{\mathcal{A}}^{el}$. The most notable conclusions are: (i) V_s and $\vec{\mathcal{A}}^{el}$ do not generate a gap by themselves (i.e., when the interlayer hopping $t_{\perp} \to 0$), and in fact tend to cancel each other's contribution when $t_{\perp} \neq 0$; (ii) the spectral gap at the primary Dirac point, that can be calculated analytically, is linear in the distortions z_u to leading order; (iii) new Dirac Points emerge in the valence and conduction bands, in agreement with the symmetry-based analysis; (iv) LDOS homogeneity is strongly broken by $(V_s, \vec{\mathcal{A}}^{el})$; (v) the overall electronic structure at finite energies shows a strong sensitivity to the values of $(z_u, m_{\pm}, g_1, g_2)$ within their realistic range. As an example, the spectral gap can range from 0 to $\sim 10\,$meV depending on their choice. Fig. 13 illustrates these results. Therefore, a direct measurement of electronic structure properties, such as the DOS, could allow to obtain accurate values of $(z_u, m_{\pm}, g_1, g_2)$, to be contrasted with the theoretical predictions.

Ref. [384] uses the values $z_u = -0.18$ (which corresponds to $u_{kk}/2 = 2.8\%$, with a graphene lattice parameter of $a = 2.4$ Å, lattice mismatch between hBN ($a_{\rm hBN}$) and graphene of $\delta = a_{\rm hBN}/a - 1 = 0.018$, $\lambda + 2\mu = 19.1$ eV/Å^2 and $\Delta\epsilon_{AB} = -100$ meV/unit cell), $t_{\perp} = 0.3$ eV and $g_2 = 4.8\text{nm}^{-1}$. Moreover, $t = 3.16$ eV, $\epsilon_c = 3.34$ eV and $\epsilon_v = -1.4$ eV. As recent works have shown that electronic screening makes graphene's deformation potential g_1 negligible in practice,[38, 39] $g_1 = 0$ was assumed here. Intriguingly, this choice of parameters achieves the best fit to LDOS experimental data[376] when switching off $\vec{\mathcal{A}}^{el}$ but taking into account in plane deformations and hoppings to hBN (see Figs. 11b and 13d).

6. Strain in the new families of 2D crystals beyond graphene

The progresses in the fabrication and characterization of graphene have been successfully applied to the isolation of single layers of other 2D materials with properties complementary to graphene [388]. Atomically thin 2D crystals of boron nitride, transition metal dichalcogenides (TMDs) like MoS_2 or WS_2, black phosphorus, etc, have been recently obtained by means of mechanical exfoliation [389, 244, 390], chemical vapour deposition (CVD) [391, 392] or laser thinning [393]. Similar to graphene, these other families of 2D crystals are extremely strong materials with high elasticity and Young modulus, and they can withstand non-hydrostatic (e.g., tensile or shear) stresses up to a significant fraction of their ideal strength without inelastic relaxation by plasticity or fracture[394]. Furthermore, the techniques to apply strain in graphene can also be applied to other 2D materials, and strain engineering has been proposed as an effective approach to continuously tune their electronic and optical properties [395]. In this section, we provide a brief overview of the effect of strain in other layered materials different from graphene, with special focus on TMDs and black phosphorus. For a comprehensive review on strain engineering in semiconducting 2D crystals, we refer the reader to Ref. [66].

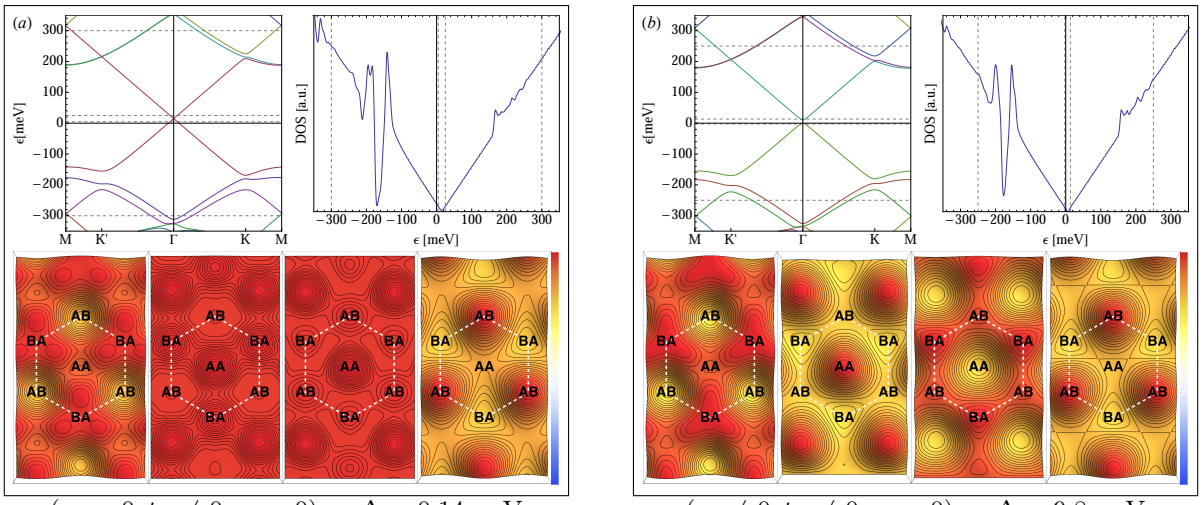

$(z_u = 0, t_\perp \neq 0, g_2 = 0) \to \Delta \approx 0.14\,\mathrm{meV}$

$(z_u \neq 0, t_\perp \neq 0, g_2 = 0) \to \Delta \approx 9.8\,\mathrm{meV}$

$(z_u \neq 0, t_\perp = 0, g_2 \neq 0) \to \Delta = 0$

$(z_u \neq 0, t_\perp \neq 0, g_2 \neq 0) \to \Delta \approx 9.6\,\mathrm{meV}$

Figure 13: Electronic structure given by the model of Eq. (113) for unrotated graphene over hBN. Different combinations of physical ingredients have been considered: unstrained graphene on hBN (a), strained graphene on hBN without pseudogauge potential (b), strained graphene electronically decoupled from hBN (c), and the complete model of a strained graphene on hBN including pseudogauge field (d). Represented are the low-energy band structure, the corresponding total DOS, and the LDOS in real space for four energies shown as dashed lines in the band structure and DOS. In the LDOS the colouring corresponds to blue for zero, and red for the maximum. We have included the value for the (non-perturbative) gap Δ at the primary Dirac point in each case.

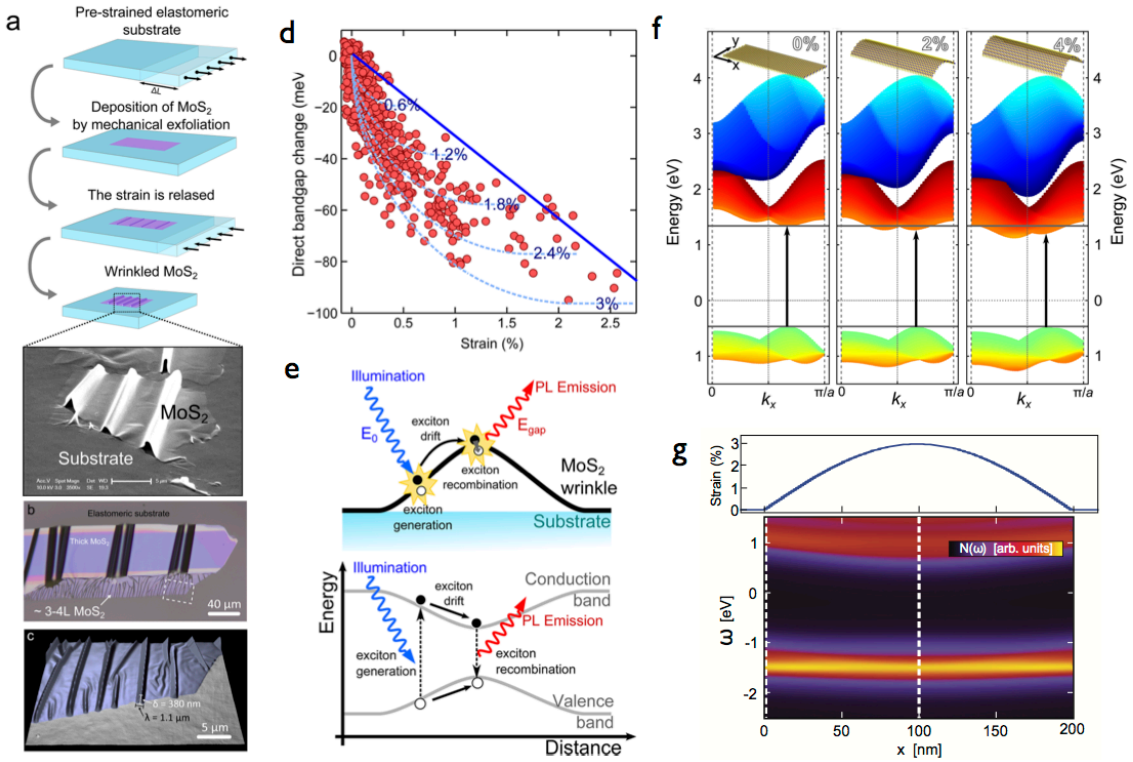

Figure 14: (a) Schematic diagram of the fabrication process of wrinkled MoS_2 nanolayers. An elastomeric substrate is stretched prior depositing MoS_2 by mechanical exfoliation. The strain is released afterwards, producing buckling-induced delamination of the MoS_2 flakes. (b) Optical microscopy image of a wrinkled MoS_2 flake fabricated by buckling-induced delamination. (c) Atomic force microscopy (AFM) topography image of the region marked by the dashed rectangle in (b). (d) Change in the energy of the direct bandgap transition as a function of the strain. The dashed lines show the expected bandgap vs strain relationship after accounting for the effect of the finite laser spot size and the funnel effect. (e) Schematic diagram explaining the funnel effect due to the nonhomogeneous strain in the wrinkled MoS_2. (f) Theoretical band structure for nonuniform strained MoS_2 calculated for a zigzag ribbon. The different panels correspond, from left to right, to the band structure for the case of an unstrained ribbon, and for wrinkled ribbons with a 2% and 4% maximum tensile strain, respectively. In the photoluminescence experiments, the wavelength of the emitted light is determined by the direct bandgap transition energy, indicated in each panel by a vertical arrow. (g) Colour map of the local density of states as a function of the position along the wrinkle profile, calculated theoretically for a wrinkle under non-uniform uniaxial strain. (Figures with permission from Ref. [396])

6.1. Transition Metal Dichalcogenides

Among the new families of 2D layered materials, TMDs are recently object of special attention. They are semiconductors with a gap in the visible range of the electromagnetic spectrum, present a strong spin-orbit coupling, and offer the possibility to control quantum degrees of freedom as the electron spin, and the valley and layer pseudospin, among other interesting features[397, 398, 399, 400]. Semiconducting TMDs have the form MX_2, where $M = \mathrm{Mo, W}$ is a transition metal and $X = \mathrm{S, Se}$ is a chalcogen atom. In their bulk configuration, they are composed of two-dimensional $X-M-X$ layers stacked on top of each other, coupled by weak van der Waals forces. The metal atoms are ordered in a triangular lattice, each of them bonded to six chalcogen atoms located in the top and bottom layers. The electronic band structure of MX_2 changes from an indirect band gap for multilayer samples to a direct gap semiconductor for single layers [389].

TMDs have a phonon structure highly sensitive to strain. This is revealed by the shift of the Raman peaks corresponding to the A_{1g} out-of-plane mode (where the top and bottom X atoms are moving out of plane in opposite directions while M is fixed), and the E^1_{2g} in-plane mode (where the M and X atoms are moving in-plane in opposite directions) [401]. In particular, applying uniaxial strain lifts the degeneracy of

the E^1_{2g} mode, leading to red shifting and splitting into two distinct peaks for strain of just 1% [396, 402, 403]. Strain in the samples can be induced by the application of forces across specific axes of the crystal structure. This effect can be used to modify the band structure of TMDs, and in fact a reduction of the band gap can be achieved under uniaxial compressive strain across the c-axis of the crystal structure of MX_2.[404] On the other hand, tensile strain is expected to lower the electron effective mass[405] and consequently improve electron mobility. A semiconductor to metal transition in single layer MoS_2 has been predicted for compressive (tensile) biaxial strain of about 15% (8%) [406], which are strengths achievable for these kind of 2D crystals [394]. First principle calculations have predicted that strain can be induced by depositing MoS_2 on hexagonal boron nitride, which can lead to a direct-to-indirect gap transition [407]. See Fig. 12 and Sec. V for a discussion on how superlattices may also induce local variations of the LDOS that is seen experimentally by STM.

Within the framework of the effective mass theory, the effect of strain in the low energy electronic spectrum can be easily incorporated by means of group theory. Similarly to the case of graphene, Eq. (8), strain tensor components can be arranged in a scalar (A'_1) and vectorial (E') irreducible representations of $D_{3h} = D_3 \otimes \sigma_h$, the point group of TMDs monolayers of the hexagonal polytype. This vector may be interpreted as a pseudo-gauge field that, together with the large spin-orbit coupling provided by M atoms and the lack of a centre of inversion in the unit cell (note that D_{3h} cannot be decomposed into a direct product of the inversion group and the group of rotations of the crystal) can lead to a quantum spin Hall effect and time-reversal invariant topological phases in these single-layer materials. For low carrier densities, as suggested in Ref. [408], semiconducting TMDs under shear strain will develop spin-polarized Landau levels residing in different valleys. For the case of MoS_2, gaps between Landau levels have been estimated to scale as $\hbar\omega_c/k_B \sim 2.7B_0[\mathrm{T}]$ K, where $\omega_c = eB_0/m^*$ is the cyclotron frequency in terms of the effective mass m^*, and $B_0[\mathrm{T}]$ is the strength of the pseudomagnetic field in Tesla. Considering that, in the case of graphene, pseudomagnetic fields of $B_0[\mathrm{T}] \sim 10 - 10^2$ T have been experimentally demonstrated [59], and taking into account the intrinsic limitations imposed by the value of the shear modulus and the maximum tensile strength of these materials, Landau level gaps of up to $\approx$ 20 K are within experimental reach. Other proposals for different polytypes have appeared in the recent literature [409]. In Ref. [410] it has been calculated a low energy $\mathbf{k}\cdot\mathbf{p}$ Hamiltonian that goes beyond the simple Dirac-like model and captures some of the main features of the electronic band dispersion of TMDs under strain, such as the shift of the conduction and valence band edges of MX_2 in the presence of homogeneous strain, with the corresponding transition from direct to indirect gap, as well as the coupling between spin degrees of freedom and strain.

Some of the aforementioned theoretical results have been confirmed experimentally, and a change in the direct band gap up to $\sim$ 45 meV per 1% applied strain has been measured [402, 403, 411, 412]. Strain engineering has been proposed as a powerful tool to create a broad-band optical funnel in layered 2D crystalline semiconductors [413]. Recent experimental observations have shown that, a continuous change in strain across an atomically thin sheet of MoS_2, leads to a continuous variation of the optical band gap [396]. This could allow not only to capture photons across a wide range of the solar spectrum, but also can guide the resulting generated excitons towards the contacts. As sketched in Fig. 14 (a)-(c), buckling induced delamination can be used to obtain samples of TMDs with a non-uniform profile of strain, up to 2.5% tensile strain. The reduction of the direct band gap with strain, shown in Fig. 14 (d), makes that the photo-induced excitons, in order to minimize their energy, move to lower bandgap regions before recombining. The nonuniform bandgap profile induced by the local strain of the wrinkles therefore generates a trap for photogenerated excitons (*funnel effect*) with a depth of up to 90 meV, as sketched in Fig. 14 (e). The effect of non-uniform strain in the band structure and in the local density of states of MoS_2, shown in Fig. 14 (f) and (g), has been theoretically studied with a tight-binding model that properly accounts for both, d-orbital contribution from the metal as well as p-orbital contribution from the chalcogen, which are relevant for the valence and conduction bands [414, 396, 415]. Recently it has been demonstrated that an optoelectronic crystal consisting of a superlattice of *artificial atoms* can be made from biaxially strained single layer MoS_2 deposited on a patterned nanocone substrate [416].

The large mechanical stretchability and flexibility of single layer TMDs together with the absence of inversion symmetry makes them good candidates for high-performance piezoelectric materials. This has been recently demonstrated experimentally by Wu et al., Ref. [417], who have shown that cyclic stretching

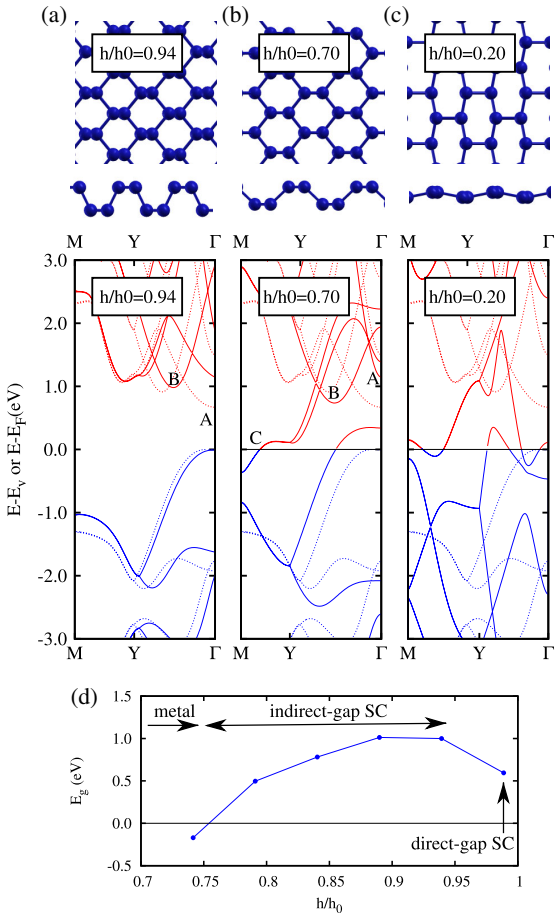

Figure 15: Single layer BP under uniaxial compression along the out-of-plane direction. Results corresponding to three values of $h = h_0$ are shown (solid line), along with the electronic band dispersion of the unstrained material (dotted lines). Top and side views represent the respective relaxed structure. (d) Change of band gap with height. The original layer thickness used in the calculations is $2h_0$. (Reproduced with permission from Ref. [418])

and releasing of thin MoS_2 flakes with an odd number of atomic layers produces oscillating piezoelectric voltage and current outputs, converting mechanical energy into electricity. On the other hand, no output is observed for flakes with an even number of layers, which possess inversion symmetry [417]. The strain-induced polarization charges in single layer MoS_2 can modulate charge carrier transport at a MoS_2-metal barrier and enable enhanced strain sensing. This demonstrates the potential of 2D crystals in powering nanodevices and tunable/stretchable electronics/optoelectronics.

6.2. Black Phosphorus

Black phosphorus (BP) is another layered material that has been recently synthesized in its single layer form, also known as *phosphorene* [419]. BP is a stable allotrope of phosphorus and an elemental semiconductor. At ambient conditions, orthorhombic BP forms puckered layers which are stacked together by weak Van der Waals forces (see Fig. 15). Similarly to graphite and TMDs, the layered structure allows for mechanical exfoliation to prepare thin layers on a substrate. The band gap is direct, located at the Γ point of the rectangular Brillouin zone, and its size highly depends on the number of layers, suggesting that multi-layer BP optical devices could allow photo-detection over a broad spectral range. Furthermore, BP is another promising material in nanoelectronics applications since the first field-effect transistors fabricated

with few layer samples show drain current modulation on the order of 10^5 (four orders of magnitude larger than that in graphene) and high charge-carrier mobilities [420].

Before the isolation of single layer BP, the effect of pressure on bulk samples was studied experimentally [421] and theoretically [422]. The stability of BP nanotubes was studied with density function tight-binding methods [423], and a Young modulus of about 300 GPa was estimated. Recent *ab initio* calculations have shown that single layer phosphorene can withstand strain up to 30%, and stress up to 18 GPa and 8 GPa in the zigzag and armchair directions, respectively [424, 425]. Furthermore, uniaxial stress along the direction perpendicular to the layer can be used to change the gap size in the system, eventually driving this semiconducting material into a 2D metal [418]. DFT calculations of Ref. [418] considered the effect of strain by including in the monolayer unit cell and corresponding atomic positions the constraint $z = \pm h$ for all the atoms (see Fig. 15). Therefore an in-plane expansion of the unit cell appears under compressive strain ($h < h_0$, where $2h_0$ is the thickness of the free layer). The structure of the BP bonds remains until $h/h_0 \sim 0.4$, leading to a lattice structure similar to that of a puckered graphene layer. The electronic band structure in BP is highly sensitive to strain, suffering a direct to indirect gap transition as we increase the compression, and a transition from indirect gap semiconductor to metal is expected for $h/h_0 \sim 0.75$, as shown in Fig. 15. The application of normal compression on bilayer samples of BP can lead to a direct-to-indirect gap transition for $\sim 3\%$ of strain, and to a fully reversible semiconductor to metal transition at $\sim 13\%$ of applied compression [426].

The peculiar puckered structure of BP layers leads to highly anisotropic in-plane optical and electronic properties [427, 428]. By applying appropriate uniaxial or biaxial strain in single layer and few-layer BP, it has been shown that the anisotropy of the electron effective mass and corresponding mobility direction can be rotated by 90° while the anisotropy of holes is not affected by the strain [429]. External strain has been shown to drive a Dirac-like dispersion in BP, which differs from the previously reported for graphene, silicene, and germanene, in the fact that the anisotropic dispersion of BP allows carriers to behave as either massless Dirac or massive carriers, depending on the transport direction along the armchair or zigzag axes, respectively [430]. This strain-engineered anisotropic conductance makes BP a promising material for mechanical and electronic applications, such as stretchable electrical devices and mechanically controlled logical devices. A huge modulation of the gap, up to ~ 1 eV, has been reported in rippled BP samples under inhomogeneous strain, suggesting that this material is an excellent candidate to create exciton funnels. In this work it has been theoretically predicted that strong confinement of carriers is possible into narrow one-dimensional ~ 150 nm wide quantum wires formed along the valleys of the sample ripples, where the sample is under compression and the gap is minimum [431].

6.3. Other 2D crystals

Whereas graphene, hBN, TMDs and BP are the most studied 2D crystals due to their demonstrated stability, there are other 2D crystals which present interesting features that deserve to be mentioned. *Silicene*, a single layer of Silicon whose atoms are ordered in a low-buckled crystalline structure, is a 2D material with non-trivial topological properties. It has been suggested that strain can be used to experimentally observe quantum spin Hall effect in this compound [432]. A single layer of Germanium, *Germanane*, is a 2D semiconductor with a (irrespective of stacking pattern and thickness) direct band gap and strain can be used to drive the membrane into its metallic phase [433]. Two-dimensional layers of Arsenic or *arsenene* have been predicted to be stable in two types of honeycomb structures: buckled and puckered [434]. Both forms present an indirect gap, that can be tuned into a direct gap by applying strain. Strain induced tuning of the band gap has been proven in the transition metal trichalcogenide TiS_3 [435], where it was found that single layer and bilayer samples undergo a direct-to-indirect band gap transition when compressive strain is induced along the preferred transport axis.

In summary, we have seen that all the experimental and theoretical techniques developed to study and control the effect of strain in graphene are being applied and adapted to other 2D crystals which have electronic and optical properties highly sensitive to mechanical deformations. This is broadening a field of research which is interesting not only from a fundamental point of view, but also because of potential applications in flexible and stretchable electronics and optoelectronics nanodevices.

Acknowledgements

We acknowledge the financial support of the following institutions: Fundação para a Ciência e a Tecnologia, Portugal, through Grant No. SFRH/BD/78987/2011 (BA); European Union through ESF funded-JAE doc program (AC); JAE-Pre (CSIC, Spain) (AGR); Juan de la Cierva Program (MINECO, Spain) and FCT-Portugal through grant no. EXPL/FIS-NAN/1720/2013 (RR); ERC Advanced Grant 290846 (FG, VP); Spanish Ministry of Economy (MINECO) through Grant No. FIS2011-23713 (PSJ) and FIS2014-58445-JIN (RR); CONICET (PIP 0747) and ANPCyT (PICT 2012-1724) (MS); Spanish MECD grant PIB2010BZ-00512, and the European Union Seventh Framework Programme under Grant Agreement No. 604391 Graphene Flagship (MV, JS).

References

[1] A. K. Geim, Graphene: Status and prospects, Science 324 (5934) (2009) 1530–1534.
[2] H. S. Seung, D. R. Nelson, Defects in flexible membranes with crystalline order, Phys. Rev. A 38 (1988) 1005–1018. doi:10.1103/PhysRevA.38.1005.
URL http://link.aps.org/doi/10.1103/PhysRevA.38.1005
[3] D. Nelson, L. Peliti, Fluctuations in membranes with crystalline and hexatic order, J. Phys. Paris 48 (1987) 1085. doi:10.1051/jphys:019870048070108500.
URL http://dx.doi.org/10.1051/jphys:019870048070108500
[4] D. Nelson, T. Piran, S. Weinberg (Eds.), Statistical Mechanics of Membranes and Surfaces, World Scientific, Singapore, 2004.
[5] N. D. Birrell, P. C. W. Davis, Quantum fields in curved space, Cambridge University Press, 1982.
[6] F. Guinea, Strain engineering in graphene, Solid State Comm. 152 (2009) 1437.
[7] A. H. Castro Neto, F. Guinea, N. M. R. Peres, K. S. Novoselov, A. K. Geim, The electronic properties of graphene, Rev. Mod. Phys. 81 (2009) 109.
[8] M. A. H. Vozmediano, M. I. Katsnelson, F. Guinea, Gauge fields in graphene, Physics Reports 496 (2010) 109.
[9] M. Katsnelson, Graphene: Carbon in Two Dimensions, Cambridge University Press, Cambridge, 2012.
[10] W. Bao, F. Miao, Z. Chen, H. Zhang, W. Jang, C. Dames, C. N. Lau, Controlled ripple texturing of suspended graphene and ultrathin graphite membranes, Nat Nano 4 (2009) 562 – 566. doi:10.1038/nnano.2009.191.
URL http://dx.doi.org/10.1038/nnano.2009.191
[11] D. Yoon, Y.-W. Son, H. Cheong, Negative thermal expansion coefficient of graphene measured by raman spectroscopy, Nano Letters 11 (8) (2011) 3227–3231. arXiv:http://pubs.acs.org/doi/pdf/10.1021/nl201488g, doi:10.1021/nl201488g.
URL http://pubs.acs.org/doi/abs/10.1021/nl201488g
[12] M. Pozzo, D. Alfè, P. Lacovig, P. Hofmann, S. Lizzit, A. Baraldi, Thermal expansion of supported and freestanding graphene: Lattice constant versus interatomic distance, Phys. Rev. Lett. 106 (2011) 135501. doi:10.1103/PhysRevLett.106.135501.
URL http://link.aps.org/doi/10.1103/PhysRevLett.106.135501
[13] A. N. Grigorenko, M. Polini, K. S. Novoselov, Graphene plasmonics, Nature Photonics 6 (11) (2012) 749–758. doi:10.1038/nphoton.2012.262.
[14] F. Bonaccorso, Z. Sun, T. Hasan, A. C. Ferrari, Graphene photonics and optoelectronics, Nature Photonics 4 (9) (2010) 611–622. doi:10.1038/nphoton.2010.186.
[15] I. Crassee, J. Levallois, A. L. Walter, M. Ostler, A. Bostwick, E. Rotenberg, T. Seyller, D. van der Marel, A. B. Kuzmenko, Giant faraday rotation in single- and multilayer graphene, Nature Physics 7 (2011) 48–51. doi:10.1038/nphys1816.
[16] R. Shimano, G. Yumoto, J. Y. Yoo, R. Matsunaga, S. Tanabe, H. Hibino, T. Morimoto, H. Aoki, Quantum faraday and kerr rotations in graphene, Nat Commun 4 (2013) 1841. doi:10.1038/ncomms2866.
[17] A. Geim, I. Grigorieva, Van der waals heterostructures, Nature 499 (7459) (2013) 419–425.
[18] S. Barraza-Lopez, A. a. P. Sanjuan, Z. Wang, M. Vanević, Strain-engineering of graphene's electronic structure beyond continuum elasticity, Solid State Commun. 166 (2013) 70–75. arXiv:1310.3622, doi:10.1016/j.ssc.2013.05.002.
[19] M. S. Dresselhaus, G. Dresselhaus, A. Jorio, Group Theory: Application to the Physics of Condensed Matter, Springer, 2008.
[20] D. M. Basko, Theory of resonant multiphonon raman scattering in graphene, Physical Review B 78 (12) (2008) 125418. doi:10.1103/PhysRevB.78.125418.
[21] L. Landau, E. Lifshitz, Course of Theoretical Physics vol. 7: "Theory of Elasticity", Pergamon Press, Oxford, 1959.
[22] P. M. Chaikin, T. C. Lubensky, Principles of condensed matter physics, Vol. 1, Cambridge Univ Press, 2000.
[23] J. A. Aronovitz, T. C. Lubensky, Fluctuations of solid membranes, Phys. Rev. Lett. 60 (1988) 2634–2637. doi:10.1103/PhysRevLett.60.2634.
URL http://link.aps.org/doi/10.1103/PhysRevLett.60.2634
[24] K. Kudin, G. E. Scuseria, B. I. Yakobson, C_2f, bn, and c nanoshell elasticity from ab initio computations, Physical Review B 64 (23) (2001) 235406. doi:10.1103/PhysRevB.64.235406.

[25] C. Lee, X. Wei, J. W. Kysar, J. Hone, Measurement of the elastic properties and intrinsic strength of monolayer graphene, Science 321 (5887) (2008) 385–388. arXiv:http://www.sciencemag.org/content/321/5887/385.full.pdf, doi:10.1126/science.1157996.
URL http://www.sciencemag.org/content/321/5887/385.abstract
[26] K. V. Zakharchenko, M. I. Katsnelson, A. Fasolino, Finite temperature lattice properties of graphene beyond the quasi-harmonic approximation, Phys. Rev. Lett. 102 (2009) 046808. doi:10.1103/PhysRevLett.102.046808.
URL http://link.aps.org/doi/10.1103/PhysRevLett.102.046808
[27] B. Amorim, F. Guinea, Flexural mode of graphene on a substrate, Phys. Rev. B 88 (2013) 115418. doi:10.1103/PhysRevB.88.115418.
URL http://link.aps.org/doi/10.1103/PhysRevB.88.115418
[28] J. L. Mañes, Symmetry-based approach to electron-phonon interactions in graphene, Phys. Rev. B 76 (2007) 045430. doi:10.1103/PhysRevB.76.045430.
URL http://link.aps.org/doi/10.1103/PhysRevB.76.045430
[29] R. Winkler, U. Zülicke, Invariant expansion for the trigonal band structure of graphene, Phys. Rev. B 82 (2010) 245313. doi:10.1103/PhysRevB.82.245313.
URL http://link.aps.org/doi/10.1103/PhysRevB.82.245313
[30] T. L. Linnik, Effective Hamiltonian of strained graphene, J. Phys.: Condens. Matter 24 (20) (2012) 205302. doi:10.1088/0953-8984/24/20/205302.
[31] H. Ochoa, A. H. C. Neto, F. Guinea, V. I. Fal'ko, Spin-orbit coupling assisted by flexural phonons in graphene, Physical Review B 86 (24) (2012) 245411. doi:10.1103/PhysRevB.86.245411.
[32] H. Ochoa, F. Guinea, V. I. Fal'ko, Spin memory and spin-lattice relaxation in two-dimensional hexagonal crystals, Physical Review B 88 (19) (2013) 195417. doi:10.1103/PhysRevB.88.195417.
[33] C. Bradley, A. Cracknell, The Mathematical Theory of Symmetry in Solids, Oxford University Press, 2010.
[34] J. Mañes, F. de Juan, M. Sturla, M. A. H. Vozmediano, Generalized effective hamiltonian for graphene under nonuniform strain, Physical Review B 88 (15) (2013) 155405. doi:10.1103/PhysRevB.88.155405.
[35] D. Cabra, N. E. Grandi, G. A. Silva, M. B. Sturla, Low-energy electron-phonon effective action from symmetry analysis, Physical Review B 88 (4) (2013) 045126. doi:10.1103/PhysRevB.88.045126.
[36] H. Suzuura, T. Ando, Phonons and electron-phonon scattering in carbon nanotubes, Physical review B 65 (23) (2002) 235412.
[37] S.-M. Choi, S.-H. Jhi, Y.-W. Son, Effects of strain on electronic properties of graphene, Phys. Rev. B 81 (8) (2010) 081407. doi:10.1103/PhysRevB.81.081407.
URL http://link.aps.org/doi/10.1103/PhysRevB.81.081407
[38] C.-H. Park, N. Bonini, T. Sohier, G. Samsonidze, B. Kozinsky, M. Calandra, F. Mauri, N. Marzari, Electron–phonon interactions and the intrinsic electrical resistivity of graphene, Nano letters 14 (3) (2014) 1113–1119.
[39] T. Sohier, M. Calandra, C.-H. Park, N. Bonini, N. Marzari, F. Mauri, Phonon-limited resistivity of graphene by first-principle calculations: electron-phonon interactions, strain-induced gauge field and boltzmann equation, arXiv preprint arXiv:1407.0830.
[40] T. Low, F. Guinea, M. I. Katsnelson, Gaps tunable by electrostatic gates in strained graphene, Physical Review B 83 (19) (2011) 195436. doi:10.1103/PhysRevB.83.195436.
[41] K. K. Gomes, W. K. W. Mar, F. Guinea, H. C. Manoharan, Designer dirac fermions and topological phases in molecular graphene, Nature 483 (2007) 306.
[42] A. Kobayashi, S. Katayama, Y. Suzumura, H. Fukuyama, Massless fermions in organic conductor, J. Phys. Soc. Jpn. 76 (2007) 034711.
[43] M. Goerbig, J.-N. Fuchs, G. Montambaux, F. Piechon, Tilted anisotropic dirac cones in quinoid-type graphene and α-(bedt-ttf)$_2$i$_3$, Physical Review B 78 (4) (2008) 045415. doi:10.1103/PhysRevB.78.045415.
[44] B. Wunsch, F. Guinea, F. Sols, Dirac-point engineering and topological phase transitions in honeycomb optical lattices, New Journal of Physics 10 (2008) 103027.
[45] G. Montambaux, F. Piechon, J.-N. Fuchs, M. O. Goerbig, Merging of dirac points in a two-dimensional crystal, Physical Review B 80 (15) (2009) 153412. doi:10.1103/PhysRevB.80.153412.
[46] T. L. Linnik, Photoinduced valley currents in strained graphene, Phys. Rev. B 90 (7) (2014) 075406. doi:10.1103/PhysRevB.90.075406.
URL http://link.aps.org/doi/10.1103/PhysRevB.90.075406
[47] F. de Juan, M. Sturla, M. A. H. Vozmediano, Space dependent fermi velocity in strained graphene, Physical Review Letters 108 (22) (2012) 227205. doi:10.1103/PhysRevLett.108.227205.
[48] F. de Juan, A. Cortijo, M. A. H. Vozmediano, Charge inhomogeneities due to smooth ripples in graphene sheets, Physical Review B 76 (16) (2007) 165409. doi:10.1103/PhysRevB.76.165409.
[49] F. de Juan, J. L. Mañes, M. A. H. Vozmediano, Gauge fields from strain in graphene, Phys. Rev. B 87 (16) (2013) 165131. doi:10.1103/PhysRevB.87.165131.
URL http://link.aps.org/doi/10.1103/PhysRevB.87.165131
[50] F. Guinea, M. I. Katsnelson, M. A. H. Vozmediano, Midgap states and charge inhomogeneities in corrugated graphene, Physical Review B 77 (7) (2008) 075422. doi:10.1103/PhysRevB.77.075422.
[51] L. Brey, J. J. Palacios, Exchange-induced charge inhomogeneities in rippled neutral graphene, Physical Review B 77 (4) (2008) 041403. doi:10.1103/PhysRevB.77.041403.
[52] Y. Zhang, V. W. Brar, C. Girit, A. Zettl, M. F. Crommie, Origin of spatial charge inhomogeneity in graphene, Nature Physics 5 (2009) 722.

[53] D. Gazit, Correlation between charge inhomogeneities and structure in graphene and other electronic crystalline membranes, Phys. Rev. B 80 (2009) 161406. doi:10.1103/PhysRevB.80.161406.
URL http://link.aps.org/doi/10.1103/PhysRevB.80.161406
[54] F. M. D. Pellegrino, G. G. N. Angilella, R. Pucci, Transport properties of graphene across strain-induced nonuniform velocity profiles, Physical Review B 84 (19) (2011) 195404. doi:10.1103/PhysRevB.84.195404.
[55] M. Gibertini, A. Tomadin, F. Guinea, M. I. Katsnelson, M. Polini, Electron-hole puddles in the absence of charged impurities, Physical Review B 85 (20) (2012) 201405. doi:10.1103/PhysRevB.85.201405.
[56] Y. Zhang, C. Luo, W. Lia, C. Pan, Strain induced chemical potential difference between monolayer graphene sheets, Nanoscale 5 (2013) 2616.
[57] F. Guinea, M. I. Katsnelson, A. K. Geim, Energy gaps and a zero-field quantum hall effect in graphene by strain engineering, Nat Phys 6 (1) (2010) 30–33.
URL http://dx.doi.org/10.1038/nphys1420
[58] F. Guinea, A. K. Geim, M. I. Katsnelson, K. S. Novoselov, Generating quantizing pseudomagnetic fields by bending graphene ribbons, Phys. Rev. B 81 (2010) 035408. doi:10.1103/PhysRevB.81.035408.
URL http://link.aps.org/doi/10.1103/PhysRevB.81.035408
[59] N. Levy, S. A. Burke, K. L. Meaker, M. Panlasigui, A. Zettl, F. Guinea, A. H. C. Neto, M. F. Crommie, Strain-induced pseudomagnetic fields greater than 300 tesla in graphene nanobubbles, Science 329 (5991) (2010) 544–547. arXiv:http://www.sciencemag.org/content/329/5991/544.full.pdf, doi:10.1126/science.1191700.
URL http://www.sciencemag.org/content/329/5991/544.abstract
[60] N. Abedpour, R. Asgari, F. Guinea, Strains and pseudomagnetic fields in circular graphene rings, Phys. Rev. B 84 (2011) 115437.
[61] N. N. Klimov, S. Jung, S. Zhu, T. Li, C. A. Wright, S. D. Solares, D. B. Newell, N. B. Zhitenev, J. A. Stroscio, Electromechanical properties of graphene drumheads, Science 336 (6088) (2012) 1557–1561. arXiv:http://www.sciencemag.org/content/336/6088/1557.full.pdf, doi:10.1126/science.1220335.
URL http://www.sciencemag.org/content/336/6088/1557.abstract
[62] L. Meng, W.-Y. He, H. Zheng, M. Liu, H. Yan, W. Yan, Z.-D. Chu, K. Bai, R.-F. Dou, Y. Zhang, Z. Liu, J.-C. Nie, L. He, Strain-induced one-dimensional landau level quantization in corrugated graphene, Phys. Rev. B 87 (2013) 205405. doi:10.1103/PhysRevB.87.205405.
URL http://link.aps.org/doi/10.1103/PhysRevB.87.205405
[63] L. Tarruell, D. Greif, T. Uehlinger, G. Jotzu, T. Esslinger, Creating, moving and merging dirac points with a fermi gas in a tunable honeycomb lattice, Nature 483 (2012) 302. doi:10.1038/nature10871.
URL http://dx.doi.org/10.1038/nature10871
[64] M. Polini, F. Guinea, M. Lewenstein, H. C. Manoharan, V. Pellegrini, Artificial honeycomb lattices for electrons, atoms and photons, Nat. Nano 8 (2013) 625.
[65] E. Mariani, A. J. Pearce, F. von Oppen, Fictitious gauge fields in bilayer graphene, Phys. Rev. B 86 (2012) 165448. doi:10.1103/PhysRevB.86.165448.
URL http://link.aps.org/doi/10.1103/PhysRevB.86.165448
[66] R. Roldán, A. Castellanos-Gomez, E. Cappelluti, F. Guinea, Strain engineering in semiconducting two-dimensional crystals, Journal of Physics: Condensed Matter 27 (31) (2015) 313201.
URL http://stacks.iop.org/0953-8984/27/i=31/a=313201
[67] A. Cortijo, Y. Ferreiros, K. Landsteiner, M. A. H. Vozmediano, Hall viscosity from elastic gauge fields in dirac crystals, arXiv:1506.05136.
[68] D. A. Gradinar, H. Schomerus, V. I. Fal'ko, Conductance anomaly near the lifshitz transition in strained bilayer graphene, Phys. Rev. B 85 (2012) 165429.
[69] D. A. Cosma, M. Mucha-Kruczyński, H. Schomerus, V. I. Fal'ko, Strain-induced modifications of transport in gated graphene nanoribbons, Phys. Rev. B 90 (2014) 245409.
[70] E. Prada, P. San-Jose, G. León, M. M. Fogler, F. Guinea, Singular elastic strains and magnetoconductance of suspended graphene, Phys. Rev. B 81 (16) (2010) 161402.
[71] H. Yan, Z.-D. Chu, W. Yan, M. Liu, L. Meng, M. Yang, Y. Fan, J. Wang, R.-F. Dou, Y. Zhang, Z. Liu, J.-C. Nie, L. He, Superlattice Dirac points and space-dependent Fermi velocity in a corrugated graphene monolayer, Phys. Rev. B 87 (7) (2013) 075405. doi:10.1103/PhysRevB.87.075405.
URL http://link.aps.org/doi/10.1103/PhysRevB.87.075405
[72] W.-J. Jang, H. Kim, Y.-R. Shin, M. Wang, S. K. Jang, M. Kim, S. Lee, S.-W. Kim, Y. J. Song, S.-J. Kahng, Observation of spatially-varying Fermi velocity in strained-graphene directly grown on hexagonal boron nitride, Carbon N. Y. 74 (2014) 139–145. doi:10.1016/j.carbon.2014.03.015.
URL http://linkinghub.elsevier.com/retrieve/pii/S0008622314002619
[73] A. Luican, G. Li, E. Y. Andrei, Quantized Landau level spectrum and its density dependence in graphene, Phys. Rev. B 83 (4) (2011) 041405. doi:10.1103/PhysRevB.83.041405.
URL http://link.aps.org/doi/10.1103/PhysRevB.83.041405
[74] J. González, F. Guinea, M. Vozmediano, The electronic spectrum of fullerenes from the Dirac equation, Nucl. Phys. B 406 (1993) 771–794.
URL http://www.sciencedirect.com/science/article/pii/055032139390009E
[75] A. Cortijo, M. A. H. Vozmediano, Electronic properties of curved graphene sheets, Europhys. Lett. 77 (4) (2007) 47002. doi:10.1209/0295-5075/77/47002.
URL http://stacks.iop.org/0295-5075/77/i=4/a=47002?key=crossref.9072831c4087484deb331afbccf84426

[76] A. Cortijo, M. A. H. Vozmediano, Effects of topological defects and local curvature on the electronic properties of planar graphene, Nucl. Phys. B 763 (3) (2007) 293–308. doi:10.1016/j.nuclphysb.2006.10.031.
URL http://linkinghub.elsevier.com/retrieve/pii/S055032130600856X
[77] J. González, J. Herrero, Graphene wormholes: A condensed matter illustration of Dirac fermions in curved space, Nucl. Phys. B 825 (3) (2010) 426–443. doi:10.1016/j.nuclphysb.2009.09.028.
URL http://linkinghub.elsevier.com/retrieve/pii/S0550321309005112
[78] O. Boada, A. Celi, J. I. Latorre, M. Lewenstein, Dirac equation for cold atoms in artificial curved spacetimes, New J. Phys. 13 (3) (2011) 035002. doi:10.1088/1367-2630/13/3/035002.
URL http://stacks.iop.org/1367-2630/13/i=3/a=035002?key=crossref.5d16f7ffe9195519e09a597998695098
[79] D. V. Khveshchenko, Simulating analogue holography in flexible Dirac metals, EPL (Europhysics Lett. 104 (4) (2013) 47002. doi:10.1209/0295-5075/104/47002.
URL http://stacks.iop.org/0295-5075/104/i=4/a=47002?key=crossref.e23ab362ec95645029301c52fc9c5fad
[80] A. Iorio, G. Lambiase, The Hawking–Unruh phenomenon on graphene, Phys. Lett. B 716 (2) (2012) 334–337. doi:10.1016/j.physletb.2012.08.023.
URL http://linkinghub.elsevier.com/retrieve/pii/S037026931200860X
[81] M. Cvetič, G. Gibbons, Graphene and the Zermelo optical metric of the BTZ black hole, Ann. Phys. (N. Y). 327 (11) (2012) 2617–2626. doi:10.1016/j.aop.2012.05.013.
URL http://linkinghub.elsevier.com/retrieve/pii/S0003491612000814
[82] A. Iorio, G. Lambiase, Quantum field theory in curved graphene spacetimes, Lobachevsky geometry, Weyl symmetry, Hawking effect, and all that, Phys. Rev. D 90 (2) (2014) 025006. doi:10.1103/PhysRevD.90.025006.
URL http://link.aps.org/doi/10.1103/PhysRevD.90.025006
[83] A. Sinner, A. Sedrakyan, K. Ziegler, Optical conductivity of graphene in the presence of random lattice deformations, Phys. Rev. B 83 (15) (2011) 155115. doi:10.1103/PhysRevB.83.155115.
URL http://link.aps.org/doi/10.1103/PhysRevB.83.155115
[84] A. J. Chaves, T. Frederico, O. Oliveira, W. de Paula, M. C. Santos, Optical conductivity of curved graphene., J. Phys. Condens. Matter 26 (18) (2014) 185301. doi:10.1088/0953-8984/26/18/185301.
URL http://www.ncbi.nlm.nih.gov/pubmed/24759188
[85] J. P. Dahlhaus, C.-Y. Hou, A. R. Akhmerov, C. W. J. Beenakker, Geodesic scattering by surface deformations of a topological insulator, Phys. Rev. B 82 (8) (2010) 085312. doi:10.1103/PhysRevB.82.085312.
URL http://link.aps.org/doi/10.1103/PhysRevB.82.085312
[86] V. Parente, P. Lucignano, P. Vitale, A. Tagliacozzo, F. Guinea, Spin connection and boundary states in a topological insulator, Phys. Rev. B 83 (7) (2011) 075424. doi:10.1103/PhysRevB.83.075424.
URL http://link.aps.org/doi/10.1103/PhysRevB.83.075424
[87] D.-H. Lee, Surface States of Topological Insulators: The Dirac Fermion in Curved Two-Dimensional Spaces, Phys. Rev. Lett. 103 (19) (2009) 196804. doi:10.1103/PhysRevLett.103.196804.
URL http://link.aps.org/doi/10.1103/PhysRevLett.103.196804
[88] B. Yang, Dirac cone metric and the origin of the spin connections in monolayer graphene, Phys. Rev. B 91 (2015) 241403. doi:10.1103/PhysRevB.91.241403.
URL http://link.aps.org/doi/10.1103/PhysRevB.91.241403
[89] V. M. Pereira, R. M. Ribeiro, N. M. R. Peres, a. H. Castro Neto, Optical properties of strained graphene, EPL (Europhysics Lett. 92 (6) (2010) 67001. doi:10.1209/0295-5075/92/67001.
URL http://stacks.iop.org/0295-5075/92/i=6/a=67001?key=crossref.650a319f52e8e981076e2ac47927ff1b
[90] V. Pereira, A. Castro Neto, N. Peres, Tight-binding approach to uniaxial strain in graphene, Phys. Rev. B 80 (4) (2009) 045401. doi:10.1103/PhysRevB.80.045401.
URL http://link.aps.org/doi/10.1103/PhysRevB.80.045401
[91] F. M. D. Pellegrino, G. G. N. Angilella, R. Pucci, Strain effect on the optical conductivity of graphene, Phys. Rev. B 81 (3) (2010) 035411. doi:10.1103/PhysRevB.81.035411.
URL http://link.aps.org/doi/10.1103/PhysRevB.81.035411
[92] M. Ramezani Masir, D. Moldovan, F. Peeters, Pseudo magnetic field in strained graphene: Revisited, Solid State Commun. 175-176 (2013) 76–82. doi:10.1016/j.ssc.2013.04.001.
URL http://linkinghub.elsevier.com/retrieve/pii/S0038109813001555
[93] M. Oliva-Leyva, G. G. Naumis, Understanding electron behavior in strained graphene as a reciprocal space distortion, Phys. Rev. B - Condens. Matter Mater. Phys. 88 (2013) 1–7. arXiv:1304.6682, doi:10.1103/PhysRevB.88.085430.
[94] G. Volovik, M. Zubkov, Emergent Horava gravity in graphene, Ann. Phys. (N. Y). 340 (1) (2014) 352–368. doi:10.1016/j.aop.2013.11.003.
URL http://linkinghub.elsevier.com/retrieve/pii/S0003491613002558
[95] F. M. D. Pellegrino, G. G. N. Angilella, R. Pucci, Resonant modes in strain-induced graphene superlattices, Phys. Rev. B 85 (19) (2012) 195409. doi:10.1103/PhysRevB.85.195409.
URL http://link.aps.org/doi/10.1103/PhysRevB.85.195409
[96] D. Faria, A. Latgé, S. E. Ulloa, N. Sandler, Currents and pseudomagnetic fields in strained graphene rings, Phys. Rev. B 87 (24) (2013) 241403. doi:10.1103/PhysRevB.87.241403.
URL http://link.aps.org/doi/10.1103/PhysRevB.87.241403
[97] G. W. Jones, V. M. Pereira, Designing electronic properties of two-dimensional crystals through optimization of deformations, New J. Phys. 16 (9) (2014) 093044. doi:10.1088/1367-2630/16/9/093044.
URL http://stacks.iop.org/1367-2630/16/i=9/a=093044?key=crossref.2f42fe3f6242d1dc85500ddc3f77303d

[98] N. M. R. Peres, Scattering in one-dimensional heterostructures described by the Dirac equation., J. Phys. Condens. Matter 21 (9) (2009) 095501. doi:10.1088/0953-8984/21/9/095501.
URL http://www.ncbi.nlm.nih.gov/pubmed/21817398
[99] A. Raoux, M. Polini, R. Asgari, a. R. Hamilton, R. Fazio, a. H. MacDonald, Velocity-modulation control of electron-wave propagation in graphene, Phys. Rev. B 81 (7) (2010) 073407. doi:10.1103/PhysRevB.81.073407.
URL http://link.aps.org/doi/10.1103/PhysRevB.81.073407
[100] A. Concha, Z. Tešanović, Effect of a velocity barrier on the ballistic transport of Dirac fermions, Phys. Rev. B 82 (3) (2010) 033413. doi:10.1103/PhysRevB.82.033413.
URL http://link.aps.org/doi/10.1103/PhysRevB.82.033413
[101] J.-H. Yuan, Z. Cheng, Q.-J. Zeng, J.-P. Zhang, J.-J. Zhang, Velocity-controlled guiding of electron in graphene: Analogy of optical waveguides, J. Appl. Phys. 110 (10) (2011) 103706. doi:10.1063/1.3660748.
URL http://scitation.aip.org/content/aip/journal/jap/110/10/10.1063/1.3660748
[102] J. R. Lima, F. Moraes, Indirect band gap in graphene from modulation of the Fermi velocity, Solid State Commun. 201 (2015) 82–87. doi:10.1016/j.ssc.2014.10.020.
URL http://linkinghub.elsevier.com/retrieve/pii/S0038109814004396
[103] J. M. Luttinger, Theory of thermal transport coefficients, Phys. Rev. 135 (1964) 1505.
[104] A. Gromov, A. G. Abanov, Thermal hall effect and geometry with torsion, arXiv:1407.2908.
[105] F. de Juan, A. Cortijo, M. A. H. Vozmediano, Dislocations and torsion in graphene and related systems, Nucl. Phys. B 828 (2010) 625.
[106] M. Z. Hasan, C. L. Kane, Topological insulators, Rev. Mod. Phys. 82 (2010) 3045.
[107] X.-L. Qi, S.-C. Zhang, Topological insulators and superconductors, Rev. Mod. Phys. 83 (2011) 1057–1110.
[108] G. V. Semenoff, Condensed matter simulation of a three-dimensional anomaly, Phys. Rev. Lett. 53 (1984) 2449.
[109] F. D. M. Haldane, Model for a quantum hall effect without landau levels: Condensed-matter realization of the parity anomaly., Phys. Rev. Lett. 61 (1988) 2015–2018.
[110] C. L. Kane, E. J. Mele, Quantum spin hall effect in graphene, Phys. Rev. Lett. 95 (2005) 226801.
[111] C. Kane, E. Mele, Z2 topological order and the quantum spin hall effect, Phys, Rev. Lett. 95 (2005) 146802.
[112] X. Wan, A. M. Turner, A. Vishwanath, S. Y. Savrasov, Topological semimetal and fermi-arc surface states in the electronic structure of pyrochlore iridates, Phys. Rev. B 83 (2011) 205101. doi:10.1103/PhysRevB.83.205101.
[113] A. A. Burkov, L. Balents, Weyl semimetal in a topological insulator multilayer, Phys. Rev. Lett. 107 (2011) 127205. doi:10.1103/PhysRevLett.107.127205.
[114] O. Vafek, A. Vishwanath, Dirac fermions in solids: From high-tc cuprates and graphene to topological insulators and weyl semimetals, Annual Review of Condensed Matter Physics 5 (2014) 83–112.
[115] M. Goerbig, G. Montambaux, Dirac fermions in condensed matter and beyond, arXiv:1410.4098.
[116] H. B. Nielsen, M. Ninomiya, Absence of neutrinos on a lattice: (i). proof by homotopy theory., Nuc. Phys. B 185 (1981) 20–40.
[117] J. L. Mañes, F. Guinea, M. A. H. Vozmediano, Existence and topological stability of fermi points in multilayered graphene, Phys. Rev. B 75 (2007) 155424.
[118] J. E. Avron, R. Seiler, P. G. Zograf, Viscosity of quantum hall fluids, Phys. Rev. Lett. 75 (1995) 697–700. doi:10.1103/PhysRevLett.75.697.
URL http://link.aps.org/doi/10.1103/PhysRevLett.75.697
[119] T. L. Hughes, R. G. Leigh, E. Fradkin, Torsional response and dissipationless viscosity in topological insulators, Phys. Rev. Lett. 107 (2011) 075502. doi:10.1103/PhysRevLett.107.075502.
URL http://link.aps.org/doi/10.1103/PhysRevLett.107.075502
[120] C. Hoyos, D. T. Son, Hall viscosity and electromagnetic response, Phys. Rev. Lett. 108 (2012) 066805. doi:10.1103/PhysRevLett.108.066805.
URL http://link.aps.org/doi/10.1103/PhysRevLett.108.066805
[121] B. Bradlyn, M. Goldstein, N. Read, Kubo formulas for viscosity: Hall viscosity, ward identities, and the relation with conductivity, Phys. Rev. B 86 (2012) 245309. doi:10.1103/PhysRevB.86.245309.
URL http://link.aps.org/doi/10.1103/PhysRevB.86.245309
[122] T. L. Hughes, R. G. Leigh, O. Parrikar, Torsional anomalies, hall viscosity, and bulk-boundary correspondence in topological states, Phys. Rev. D 88 (2013) 025040.
[123] G. Y. Cho, Y. You, E. Fradkin, Field theory of the geometry of fractional quantum hall fluids, arXiv:1406.2700.
[124] C. Hoyos, B. S. Kim, Y. Oz, Ward identities for hall transport, arXiv:1407.2616.
[125] X. G. Wen, A. Zee, Shift and spin vector: New topological quantum numbers for the hall fluids, Phys. Rev. Lett. 69 (1992) 953.
[126] H. Satz, The quark-gluon plasma. a short introduction, Nucl. Phys. A 862 (2011) 4.
[127] K. Fukushima, D. E. Kharzeev, H. J. Warringa, Chiral magnetic effect, Phys. Rev. D 85 (2008) 045104.
[128] M. N. Chernodub, A. Cortijo, A. G. Grushin, K. Landsteiner, M. A. H. Vozmediano, Condensed matter realization of the axial magnetic effect, Phys. Rev. B 89 (2014) 081407. doi:10.1103/PhysRevB.89.081407.
URL http://link.aps.org/doi/10.1103/PhysRevB.89.081407
[129] M. Stone, Gravitational anomalies and thermal hall effect in topological insulators, Phys. Rev. B 85 (2012) 184503.
[130] K. Landsteiner, E. Megías, F. Pena-Benitez, Gravitational anomaly and transport phenomena, Phys. Rev. Lett. 107 (2011) 021601. doi:10.1103/PhysRevLett.107.021601.
URL http://link.aps.org/doi/10.1103/PhysRevLett.107.021601
[131] A. Gromov, A. G. Abanov, Density-curvature response and gravitational anomaly, Phys.Rev.Lett. 113 (2014) 266702.

[132] A. Rycerz, J. Tworzydlo, C. W. J. Beenakker, Valley filter and valley valve in graphene, Nat. Phys. 3 (2007) 172.
[133] Y. Jiang, T. Low, K. Chang, M. I. Katsnelson, F. Guinea, Generation of pure bulk valley current in graphene, Phys. Rev. Lett. 110 (2013) 046601. doi:10.1103/PhysRevLett.110.046601.
URL http://link.aps.org/doi/10.1103/PhysRevLett.110.046601
[134] F. von Oppen, F. Guinea, E. Mariani, Synthetic electric fields and phonon damping in carbon nanotubes and graphene, Phys. Rev. B 80 (2009) 075420.
[135] A. Vaezi, N. Abedpour, R. Asgari, A. Cortijo, M. A. H. Vozmediano, Topological electric current from time-dependent elastic deformations in graphene, Phys. Rev. B 88 (2013) 125406. doi:10.1103/PhysRevB.88.125406.
URL http://link.aps.org/doi/10.1103/PhysRevB.88.125406
[136] A. Cortijo, A. G. Grushin, M. A. H. Vozmediano, Topological insulating phases in monolayer and bilayer graphene: An effective action approach, Phys. Rev. B 82 (2010) 195438.
[137] M. Trif, P. Upadhyaya, Y. Tserkovnyak, Theory of electromechanical coupling in dynamical graphene, Phys. Rev. B 88 (2013) 245423.
[138] Y. A. Firsov, N. E. Firsova, Surface corrugations influence monolayer graphene electromagnetic response, Physica E 62 (2014) 36.
[139] S. A. Yang, H. Pan, F. Zhang, Buckled honeycomb lattice materials and unconventional magnetic responses, RSC Adv. 5 (2015) 83350–83360. doi:10.1039/C5RA13699G.
URL http://dx.doi.org/10.1039/C5RA13699G
[140] R. V. Gorbachev, J. C. W. Song, G. L. Yu, A. V. Kretinin, F. Withers, Y. Cao, A. Mishchenko, I. V. Grigorieva, K. S. Novoselov, L. S. Levitov, A. K. Geim1, Detecting topological currents in graphene superlattices, Science 346 (2014) 448.
[141] R. Peierls, Bemerkungten über umwandlungstemperaturen, Helv. Phys. Acta 7 (1934) 81 – 83.
[142] L. D. Landau, Zur theorie der phasenumwandlungten ii, Phys. Z. Sowjetunion 11 (1937) 26 – 35.
[143] N. D. Mermin, Crystalline order in two dimensions, Phys. Rev. 176 (1968) 250–254. doi:10.1103/PhysRev.176.250.
URL http://link.aps.org/doi/10.1103/PhysRev.176.250
[144] G. Gompper, D. M. Kroll, Network models of fluid, hexatic and polymerized membranes, Journal of Physics: Condensed Matter 9 (42) (1997) 8795.
URL http://stacks.iop.org/0953-8984/9/i=42/a=001
[145] M. J. Bowick, A. Travesset, The statistical mechanics of membranes, Physics Reports 344 (4–6) (2001) 255 – 308, renormalization group theory in the new millennium. doi:http://dx.doi.org/10.1016/S0370-1573(00)00128-9.
URL http://www.sciencedirect.com/science/article/pii/S0370157300001289
[146] J. Aronovitz, L. Golubovic, T. Lubensky, Fluctuations and lower critical dimensions of crystalline membranes, J. Phys. France 50 (6) (1989) 609–631. doi:10.1051/jphys:01989005006060900.
URL http://dx.doi.org/10.1051/jphys:01989005006060900
[147] K. V. Zakharchenko, R. Roldán, A. Fasolino, M. I. , Self-consistent screening approximation for flexible membranes: Application to graphene, Phys. Rev. B 82 (2010) 125435. doi:10.1103/PhysRevB.82.125435.
URL http://link.aps.org/doi/10.1103/PhysRevB.82.125435
[148] B. Amorim, R. Roldán, E. Cappelluti, A. Fasolino, F. Guinea, M. I. Katsnelson, Thermodynamics of quantum crystalline membranes, Phys. Rev. B 89 (2014) 224307. doi:10.1103/PhysRevB.89.224307.
URL http://link.aps.org/doi/10.1103/PhysRevB.89.224307
[149] B. Amorim, R. Roldán, E. Cappelluti, A. Fasolino, F. Guinea, M. I. Katsnelson, Thermodynamical properties and stability of crystalline membranes in the quantum regime, in: Symposium K Graphene and Graphene Nanocomposites, Vol. 1727 of MRS Proceedings, 2015. doi:10.1557/opl.2015.67.
URL http://journals.cambridge.org/article_S1946427415000676
[150] E. Mariani, F. von Oppen, Flexural phonons in free-standing graphene, Phys. Rev. Lett. 100 (2008) 076801. doi:10.1103/PhysRevLett.100.076801.
URL http://link.aps.org/doi/10.1103/PhysRevLett.100.076801
[151] F. David, E. Guitter, Crumpling transition in elastic membranes: Renormalization group treatment, EPL (Europhysics Letters) 5 (8) (1988) 709.
URL http://stacks.iop.org/0295-5075/5/i=8/a=008
[152] P. Le Doussal, L. Radzihovsky, Self-consistent theory of polymerized membranes, Phys. Rev. Lett. 69 (1992) 1209–1212. doi:10.1103/PhysRevLett.69.1209.
URL http://link.aps.org/doi/10.1103/PhysRevLett.69.1209
[153] D. Gazit, Structure of physical crystalline membranes within the self-consistent screening approximation, Phys. Rev. E 80 (2009) 041117. doi:10.1103/PhysRevE.80.041117.
URL http://link.aps.org/doi/10.1103/PhysRevE.80.041117
[154] Z. Zhang, H. T. Davis, D. M. Kroll, Scaling behavior of self-avoiding tethered vesicles, Phys. Rev. E 48 (1993) R651–R654. doi:10.1103/PhysRevE.48.R651.
URL http://link.aps.org/doi/10.1103/PhysRevE.48.R651
[155] M. J. Bowick, S. M. Catterall, M. Falcioni, G. Thorleifsson, K. N. Anagnostopoulos, The flat phase of crystalline membranes, Journal de Physique I 6 (10) (1996) 1321–1345. doi:10.1051/jp1:1996139.
URL http://dx.doi.org/10.1051/jp1:1996139
[156] M. Bowick, S. Catterall, M. Falcioni, G. Thorleifsson, K. Anagnostopoulos, The flat phase of fixed-connectivity membranes, Nuclear Physics B Proceedings Supplements 53 (1-3) (1997) 746–752. doi:10.1016/S0920-5632(96)00771-2.
URL http://dx.doi.org/10.1016/S0920-5632(96)00771-2
[157] J. H. Los, M. I. Katsnelson, O. V. Yazyev, K. V. Zakharchenko, A. Fasolino, Scaling properties of flexible membranes

from atomistic simulations: Application to graphene, Phys. Rev. B 80 (2009) 121405. doi:10.1103/PhysRevB.80.121405.
URL http://link.aps.org/doi/10.1103/PhysRevB.80.121405
[158] A. Tröster, High-precision fourier monte carlo simulation of crystalline membranes, Phys. Rev. B 87 (2013) 104112. doi:10.1103/PhysRevB.87.104112.
URL http://link.aps.org/doi/10.1103/PhysRevB.87.104112
[159] A. Tröster, Fourier monte carlo renormalization-group approach to crystalline membranes, Phys. Rev. E 91 (2015) 022132. doi:10.1103/PhysRevE.91.022132.
URL http://link.aps.org/doi/10.1103/PhysRevE.91.022132
[160] J.-P. Kownacki, D. Mouhanna, Crumpling transition and flat phase of polymerized phantom membranes, Phys. Rev. E 79 (2009) 040101. doi:10.1103/PhysRevE.79.040101.
URL http://link.aps.org/doi/10.1103/PhysRevE.79.040101
[161] F. L. Braghin, N. Hasselmann, Thermal fluctuations of free-standing graphene, Phys. Rev. B 82 (2010) 035407. doi:10.1103/PhysRevB.82.035407.
URL http://link.aps.org/doi/10.1103/PhysRevB.82.035407
[162] N. Hasselmann, F. L. Braghin, Nonlocal effective-average-action approach to crystalline phantom membranes, Phys. Rev. E 83 (2011) 031137. doi:10.1103/PhysRevE.83.031137.
URL http://link.aps.org/doi/10.1103/PhysRevE.83.031137
[163] K. Essafi, J.-P. Kownacki, D. Mouhanna, First-order phase transitions in polymerized phantom membranes, Phys. Rev. E 89 (2014) 042101. doi:10.1103/PhysRevE.89.042101.
URL http://link.aps.org/doi/10.1103/PhysRevE.89.042101
[164] F. F. Abraham, D. R. Nelson, Fluctuations in the flat and collapsed phases of polymerized membranes, J. Phys. France 51 (23) (1990) 2653 – 2672. doi:10.1051/jphys:0199000510230265300.
URL http://dx.doi.org/10.1051/jphys:0199000510230265300
[165] E. Guitter, F. David, S. Leibler, L. Peliti, Crumpling and buckling transitions in polymerized membranes, Phys. Rev. Lett. 61 (1988) 2949–2952. doi:10.1103/PhysRevLett.61.2949.
URL http://link.aps.org/doi/10.1103/PhysRevLett.61.2949
[166] E. Guitter, F. David, S. Leibler, L. Peliti, Thermodynamical behavior of polymerized membranes, J. Phys. France 50 (14) (1989) 1787 – 1819. doi:10.1051/jphys:0198900500140178700.
URL http://dx.doi.org/10.1051/jphys:0198900500140178700
[167] R. Roldán, A. Fasolino, K. V. Zakharchenko, M. I. Katsnelson, Suppression of anharmonicities in crystalline membranes by external strain, Phys. Rev. B 83 (2011) 174104. doi:10.1103/PhysRevB.83.174104.
URL http://link.aps.org/doi/10.1103/PhysRevB.83.174104
[168] D. R. Nelson, L. Radzihovsky, Polymerized membranes with quenched random internal disorder, EPL (Europhysics Letters) 16 (1) (1991) 79.
URL http://stacks.iop.org/0295-5075/16/i=1/a=014
[169] L. Radzihovsky, D. R. Nelson, Statistical mechanics of randomly polymerized membranes, Phys. Rev. A 44 (1991) 3525–3542. doi:10.1103/PhysRevA.44.3525.
URL http://link.aps.org/doi/10.1103/PhysRevA.44.3525
[170] D. C. Morse, T. C. Lubensky, Curvature disorder in tethered membranes: A new flat phase at $T = 0$, Phys. Rev. A 46 (1992) 1751–1768. doi:10.1103/PhysRevA.46.1751.
URL http://link.aps.org/doi/10.1103/PhysRevA.46.1751
[171] P. Le Doussal, L. Radzihovsky, Flat glassy phases and wrinkling of polymerized membranes with long-range disorder, Phys. Rev. B 48 (1993) 3548–3551. doi:10.1103/PhysRevB.48.3548.
URL http://link.aps.org/doi/10.1103/PhysRevB.48.3548
[172] R. C. Thompson-Flagg, M. J. B. Moura, M. Marder, Rippling of graphene, EPL (Europhysics Letters) 85 (4) (2009) 46002.
URL http://stacks.iop.org/0295-5075/85/i=4/a=46002
[173] A. Košmrlj, D. R. Nelson, Mechanical properties of warped membranes, Phys. Rev. E 88 (2013) 012136. doi:10.1103/PhysRevE.88.012136.
URL http://link.aps.org/doi/10.1103/PhysRevE.88.012136
[174] A. Košmrlj, D. R. Nelson, Thermal excitations of warped membranes, Phys. Rev. E 89 (2014) 022126. doi:10.1103/PhysRevE.89.022126.
URL http://link.aps.org/doi/10.1103/PhysRevE.89.022126
[175] I. V. Gornyi, V. Y. Kachorovskii, A. D. Mirlin, Rippling and crumpling in disordered free-standing graphene, ArXiv e-printsarXiv:1505.04483.
[176] J. Meyer, A. Geim, M. Katsnelson, K. Novoselov, T. Booth, S. Roth, The structure of suspended graphene sheets, Nature 446 (2007) 60. doi:10.1038/nature05545.
URL http://dx.doi.org/10.1038/nature05545
[177] D. A. Kirilenko, A. T. Dideykin, G. Van Tendeloo, Measuring the corrugation amplitude of suspended and supported graphene, Phys. Rev. B 84 (2011) 235417. doi:10.1103/PhysRevB.84.235417.
URL http://link.aps.org/doi/10.1103/PhysRevB.84.235417
[178] P. San-Jose, J. González, F. Guinea, Electron-induced rippling in graphene, Phys. Rev. Lett. 106 (2011) 045502. doi:10.1103/PhysRevLett.106.045502.
URL http://link.aps.org/doi/10.1103/PhysRevLett.106.045502
[179] F. Guinea, P. Le Doussal, K. J. Wiese, Collective excitations in a large-d model for graphene, Phys. Rev. B 89 (2014)

125428. doi:10.1103/PhysRevB.89.125428.
URL http://link.aps.org/doi/10.1103/PhysRevB.89.125428
[180] E. I. Kats, V. V. Lebedev, Asymptotic freedom at zero temperature in free-standing crystalline membranes, Phys. Rev. B 89 (2014) 125433. doi:10.1103/PhysRevB.89.125433.
URL http://link.aps.org/doi/10.1103/PhysRevB.89.125433
[181] A. L. C. da Silva, L. Cândido, J. N. T. Rabelo, G.-Q. Hai, F. M. Peeters, Anharmonic effects on thermodynamic properties of a graphene monolayer, EPL (Europhysics Letters) 107 (5) (2014) 56004.
URL http://stacks.iop.org/0295-5075/107/i=5/a=56004
[182] D. Gazit, Theory of the spontaneous buckling of doped graphene, Phys. Rev. B 79 (2009) 113411. doi:10.1103/PhysRevB.79.113411.
URL http://link.aps.org/doi/10.1103/PhysRevB.79.113411
[183] J. González, E. Perfetto, Many-body effects on out-of-plane phonons in graphene, New Journal of Physics 11 (9) (2009) 095015.
URL http://stacks.iop.org/1367-2630/11/i=9/a=095015
[184] J. González, Rippling transition from electron-induced condensation of curvature field in graphene, Phys. Rev. B 90 (2014) 165402. doi:10.1103/PhysRevB.90.165402.
URL http://link.aps.org/doi/10.1103/PhysRevB.90.165402
[185] M. I. Katsnelson, A. Fasolino, Graphene as a prototype crystalline membrane, Accounts of Chemical Research 46 (1) (2013) 97–105. arXiv:http://pubs.acs.org/doi/pdf/10.1021/ar300117m, doi:10.1021/ar300117m.
URL http://pubs.acs.org/doi/abs/10.1021/ar300117m
[186] S. K. Sinha, E. B. Sirota, S. Garoff, H. B. Stanley, X-ray and neutron scattering from rough surfaces, Phys. Rev. B 38 (1988) 2297–2311. doi:10.1103/PhysRevB.38.2297.
URL http://link.aps.org/doi/10.1103/PhysRevB.38.2297
[187] F. F. Abraham, D. R. Nelson, Diffraction from polymerized membranes, Science 249 (4967) (1990) 393–397.
[188] F. F. Abraham, M. Goulian, Diffraction from polymerized membranes: Flat vs. crumpled, EPL (Europhysics Letters) 19 (4) (1992) 293.
URL http://stacks.iop.org/0295-5075/19/i=4/a=008
[189] M. Goulian, N. Lei, J. Miller, S. K. Sinha, Structure factor for randomly oriented self-affine membranes, Phys. Rev. A 46 (1992) R6170–R6173. doi:10.1103/PhysRevA.46.R6170.
URL http://link.aps.org/doi/10.1103/PhysRevA.46.R6170
[190] H.-N. Yang, T.-M. Lu, G.-C. Wang, Diffraction from surface growth fronts, Phys. Rev. B 47 (1993) 3911–3922. doi:10.1103/PhysRevB.47.3911.
URL http://link.aps.org/doi/10.1103/PhysRevB.47.3911
[191] C. Schmidt, K. Svoboda, N. Lei, I. Petsche, L. Berman, C. Safinya, G. Grest, Existence of a flat phase in red cell membrane skeletons, Science 259 (5097) (1993) 952–955. arXiv:http://www.sciencemag.org/content/259/5097/952.full.pdf, doi:10.1126/science.8438153.
URL http://www.sciencemag.org/content/259/5097/952.abstract
[192] C. Gourier, J. Daillant, A. Braslau, M. Alba, K. Quinn, D. Luzet, C. Blot, D. Chatenay, G. Grübel, J.-F. Legrand, G. Vignaud, Bending energy of amphiphilic films at the nanometer scale, Phys. Rev. Lett. 78 (1997) 3157–3160. doi:10.1103/PhysRevLett.78.3157.
URL http://link.aps.org/doi/10.1103/PhysRevLett.78.3157
[193] J. Meyer, A. Geim, M. Katsnelson, K. Novoselov, D. Obergfell, S. Roth, C. Girit, A. Zettl, On the roughness of single- and bi-layer graphene membranes, Solid State Communications 143 (1 - 2) (2007) 101 – 109, exploring graphene Recent research advances. doi:10.1016/j.ssc.2007.02.047.
URL http://www.sciencedirect.com/science/article/pii/S003810980700316X
[194] J. Brivio, D. T. L. Alexander, A. Kis, Ripples and layers in ultrathin mos2 membranes, Nano Letters 11 (12) (2011) 5148–5153. doi:10.1021/nl2022288.
URL http://pubs.acs.org/doi/abs/10.1021/nl2022288
[195] A. Locatelli, K. R. Knox, D. Cvetko, T. O. Menteş, M. A. Niño, S. Wang, M. B. Yilmaz, P. Kim, R. M. Osgood, A. Morgante, Corrugation in exfoliated graphene: An electron microscopy and diffraction study, ACS Nano 4 (8) (2010) 4879–4889, pMID: 20681631. arXiv:http://dx.doi.org/10.1021/nn101116n, doi:10.1021/nn101116n.
URL http://dx.doi.org/10.1021/nn101116n
[196] R. Zan, C. Muryn, U. Bangert, P. Mattocks, P. Wincott, D. Vaughan, X. Li, L. Colombo, R. S. Ruoff, B. Hamilton, K. S. Novoselov, Scanning tunnelling microscopy of suspended graphene, Nanoscale 4 (2012) 3065–3068. doi:10.1039/C2NR30162H.
URL http://dx.doi.org/10.1039/C2NR30162H
[197] E. Cerda, L. Mahadevan, Geometry and physics of wrinkling, Phys. Rev. Lett. 90 (2003) 074302. doi:10.1103/PhysRevLett.90.074302.
URL http://link.aps.org/doi/10.1103/PhysRevLett.90.074302
[198] F. Guinea, B. Horovitz, P. Le Doussal, Gauge field induced by ripples in graphene, Phys. Rev. B 77 (2008) 205421. doi:10.1103/PhysRevB.77.205421.
URL http://link.aps.org/doi/10.1103/PhysRevB.77.205421
[199] U. Bangert, M. H. Gass, A. L. Bleloch, R. R. Nair, A. K. Geim, Manifestation of ripples in free-standing graphene in lattice images obtained in an aberration-corrected scanning transmission electron microscope, physica status solidi (a) 206 (6) (2009) 1117–1122. doi:10.1002/pssa.200824453.

URL http://dx.doi.org/10.1002/pssa.200824453
[200] U. Bangert, M. H. Gass, A. L. Bleloch, R. R. Nair, J. Eccles, Nanotopography of graphene, physica status solidi (a) 206 (9) (2009) 2115–2119. doi:10.1002/pssa.200982207.
URL http://dx.doi.org/10.1002/pssa.200982207
[201] P. Xu, M. Neek-Amal, S. D. Barber, J. K. Schoelz, M. L. Ackerman, P. M. Thibado, A. Sadeghi, F. M. Peeters, Unusual ultra-low-frequency fluctuations in freestanding graphene, Nat Commun 5, supplementary information available for this article at http://www.nature.com/ncomms/2014/140428/ncomms4720/suppinfo/ncomms4720_S1.html. doi:10.1038/ncomms4720.
URL http://dx.doi.org/10.1038/ncomms4720
[202] M. Neek-Amal, P. Xu, J. Schoelz, M. Ackerman, S. Barber, P. Thibado, A. Sadeghi, F. Peeters, Thermal mirror buckling in freestanding graphene locally controlled by scanning tunnelling microscopy, Nat Commun 5 (4962). doi:doi:10.1038/ncomms5962.
URL http://dx.doi.org/10.1038/ncomms5962
[203] J. K. Schoelz, P. Xu, V. Meunier, P. Kumar, M. Neek-Amal, P. M. Thibado, F. M. Peeters, Graphene ripples as a realization of a two-dimensional ising model: A scanning tunneling microscope study, Phys. Rev. B 91 (2015) 045413. doi:10.1103/PhysRevB.91.045413.
URL http://link.aps.org/doi/10.1103/PhysRevB.91.045413
[204] U. Komaragirl, M. R. Begley, S. J. G., The mechanical response of freestanding circular elastic films under point and pressure loads, J. Appl. Mech. 72 (2005) 203 – 212. doi:10.1115/1.1827246.
URL http://dx.doi.org/10.1115/1.1827246
[205] S. Guo, K.-T. Wan, D. A. Dillard, A bending-to-stretching analysis of the blister test in the presence of tensile residual stress, International Journal of Solids and Structures 42 (9–10) (2005) 2771 – 2784. doi:http://dx.doi.org/10.1016/j.ijsolstr.2004.10.007.
URL http://www.sciencedirect.com/science/article/pii/S0020768304005736
[206] C.-r. Jin, Large deflection of circular membrane under concentrated force, Applied Mathematics and Mechanics 29 (7) (2008) 889–896. doi:10.1007/s10483-008-0707-x.
URL http://dx.doi.org/10.1007/s10483-008-0707-x
[207] C. Jin, X. Wang, A theoretical study of a thin-film delamination using shaft-loaded blister test: Constitutive relation without delamination, Journal of the Mechanics and Physics of Solids 56 (9) (2008) 2815 – 2831. doi:http://dx.doi.org/10.1016/j.jmps.2008.04.009.
URL http://www.sciencedirect.com/science/article/pii/S0022509608000859
[208] G. Lopez-Polin, C. Gomez-Navarro, V. Parente, F. Guinea, M. I. Katsnelson, F. Perez-Murano, J. Gomez-Herrero, Increasing the elastic modulus of graphene by controlled defect creation, Nat Phys 11 (2015) 26 – 31, http://www.nature.com/nphys/journal/v11/n1/abs/nphys3183.html supplementary-information. doi:10.1038/nphys3183.
URL http://dx.doi.org/10.1038/nphys3183
[209] A. S. Fedorov, Z. I. Popov, D. A. Fedorov, N. S. Eliseeva, M. V. Serjantova, A. A. Kuzubov, Dft investigation of the influence of ordered vacancies on elastic and magnetic properties of graphene and graphene-like sic and bn structures, Physica Status Solidi (b) 249 (12) (2012) 2549–2552. doi:10.1002/pssb.201200105.
URL http://dx.doi.org/10.1002/pssb.201200105
[210] N. Jing, Q. Xue, C. Ling, M. Shan, T. Zhang, X. Zhou, Z. Jiao, Effect of defects on young's modulus of graphene sheets: a molecular dynamics simulation, RSC Adv. 2 (2012) 9124–9129. doi:10.1039/C2RA21228E.
URL http://dx.doi.org/10.1039/C2RA21228E
[211] M. Neek-Amal, F. M. Peeters, Linear reduction of stiffness and vibration frequencies in defected circular monolayer graphene, Phys. Rev. B 81 (2010) 235437. doi:10.1103/PhysRevB.81.235437.
URL http://link.aps.org/doi/10.1103/PhysRevB.81.235437
[212] G. López-Polín, M. Jaafar, F. Guinea, R. Roldán, C. Gómez-Navarro, J. Gómez-Herrero, Strain dependent elastic modulus of graphene, ArXiv e-printsarXiv:1504.05521.
[213] J. H. Los, A. Fasolino, M. I. Katsnelson, Scaling behavior and strain dependence of in-plane elastic properties of graphene, ArXiv e-printsarXiv:1508.05257.
[214] M. K. Blees, A. W. Barnard, P. A. Rose, S. P. Roberts, K. L. McGill, P. Y. Huang, A. R. Ruyack, J. W. Kevek, B. Kobrin, D. A. Muller, et al., Graphene kirigami, Nature 524 (2015) 204.
[215] A. Kosmrlj, D. R. Nelson, Response of thermalized ribbons to pulling and bending, ArXiv e-printsarXiv:1508.01528.
[216] P. L. de Andres, F. Guinea, M. I. Katsnelson, Bending modes, anharmonic effects, and thermal expansion coefficient in single-layer and multilayer graphene, Phys. Rev. B 86 (2012) 144103. doi:10.1103/PhysRevB.86.144103.
URL http://link.aps.org/doi/10.1103/PhysRevB.86.144103
[217] I. M. Lifshitz, Zh. Eksp. Teor. Fiz. 22 (1952) 475.
[218] N. Mounet, N. Marzari, First-principles determination of the structural, vibrational and thermodynamic properties of diamond, graphite, and derivatives, Phys. Rev. B 71 (2005) 205214. doi:10.1103/PhysRevB.71.205214.
URL http://link.aps.org/doi/10.1103/PhysRevB.71.205214
[219] J.-W. Jiang, J.-S. Wang, B. Li, Thermal expansion in single-walled carbon nanotubes and graphene: Nonequilibrium green's function approach, Phys. Rev. B 80 (2009) 205429. doi:10.1103/PhysRevB.80.205429.
URL http://link.aps.org/doi/10.1103/PhysRevB.80.205429
[220] W. Gao, R. Huang, Thermomechanics of monolayer graphene: Rippling, thermal expansion and elasticity, Journal of the Mechanics and Physics of Solids 66 (0) (2014) 42 – 58. doi:http://dx.doi.org/10.1016/j.jmps.2014.01.011.
URL http://www.sciencedirect.com/science/article/pii/S0022509614000210

[221] B. I. Halperin, D. R. Nelson, Theory of two-dimensional melting, Phys. Rev. Lett. 41 (1978) 121–124.
[222] D. R. Nelson, B. I. Halperin, Dislocation-mediated melting in two dimensions, Phys. Rev. B 19 (1979) 2457–2484. doi:10.1103/PhysRevB.19.2457.
URL http://link.aps.org/doi/10.1103/PhysRevB.19.2457
[223] D. R. Nelson, Defects in Superfluids, Superconductors and Membranes, eprint arXiv:cond-mat/9502114arXiv:cond-mat/9502114.
[224] K. V. Zakharchenko, A. Fasolino, J. H. Los, M. I. Katsnelson, Melting of graphene: from two to one dimension, Journal of Physics: Condensed Matter 23 (20) (2011) 202202.
[225] J. H. Los, K. V. Zakharchenko, M. I. Katsnelson, A. Fasolino, Melting temperature of graphene, Phys. Rev. B 91 (2015) 045415. doi:10.1103/PhysRevB.91.045415.
URL http://link.aps.org/doi/10.1103/PhysRevB.91.045415
[226] S. K. Singh, M. Neek-Amal, F. M. Peeters, Melting of graphene clusters, Phys. Rev. B 87 (2013) 134103.
[227] S. Iijima, C. Brabec, A. Maiti, J. Bernholc, Structural flexibility of carbon nanotubes, The Journal of Chemical Physics 104 (5) (1996) 2089–2092.
[228] M. Buongiorno Nardelli, B. I. Yakobson, J. Bernholc, Mechanism of strain release in carbon nanotubes, Phys. Rev. B 57 (1998) R4277–R4280.
[229] J. H. Warner, E. R. Margine, M. Mukai, A. W. Robertson, F. Giustino, A. I. Kirkland, Dislocation-driven deformations in graphene, Science 337 (2012) 209.
[230] C. Gomez-Navarro, J. C. Meyer, R. S. Sundaram, A. Chuvilin, S. Kurasch, M. Burghard, K. Kern, U. Kaiser, Atomic structure of reduced graphene oxide, Nano Letters 10 (4) (2010) 1144–1148.
[231] A. Carpio, L. L. Bonilla, Periodized discrete elasticity models for defects in graphene, Phys. Rev. B 78 (2008) 085406.
[232] O. Lehtinen, S. Kurasch, A. V. Krasheninnikov, U. Kaiser, Atomic scale study of the life cycle of a dislocation in graphene from birth to annihilation, Nat. Comm. 4 (2013) 2098.
[233] S. Chen, D. C. Chrzan, Continuum theory of dislocations and buckling in graphene, Phys. Rev. B 84 (2011) 214103.
[234] M. Lazar, Dislocation field theory in 2d: Application to graphene, Physics Letters A 377 (5) (2013) 423 – 429.
[235] X. Li, W. Cai, J. An, S. Kim, J. Nah, D. Yang, R. Piner, A. Velamakanni, I. Jung, E. Tutuc, S. K. Banerjee, L. Colombo, R. S. Ruoff, Large-area synthesis of high-quality and uniform graphene films on copper foils, Science 324 (2009) 1312.
[236] Q. Yu, L. A. Jauregui, W. Wu, R. Colby, J. Tian, Z. Su, H. Cao, Z. Liu, D. Pandey, D. Wei, T. F. Chung, P. Peng, N. P. Guisinger, E. A. Stach, J. Bao, S.-S. Pei, Y. P. Chen, Control and characterization of individual grains and grain boundaries in graphene grown by chemical vapour deposition, Nat. Mater. 10 (2011) 443–449.
[237] Y. Wei, J. Wu, H. Yin, X. Shi, R. Yang, M. Dresselhaus, The nature of strength enhancement and weakening by pentagonheptagon defects in graphene, Nat Mater 11 (2012) 759–763.
[238] R. Grantab, V. B. Shenoy, R. S. Ruoff, Anomalous strength characteristics of tilt grain boundaries in graphene, Science 330 (6006) (2010) 946–948.
[239] N. M. R. Peres, Colloquium: The transport properties of graphene: An introduction, Rev. Mod. Phys. 82 (3) (2010) 2673–2700.
URL http://link.aps.org/doi/10.1103/RevModPhys.82.2673
[240] E. H. Hwang, S. Das Sarma, Acoustic phonon scattering limited carrier mobility in two-dimensional extrinsic graphene, Phys. Rev. B 77 (2008) 115449. doi:10.1103/PhysRevB.77.115449.
URL http://link.aps.org/doi/10.1103/PhysRevB.77.115449
[241] E. V. Castro, H. Ochoa, M. I. Katsnelson, R. V. Gorbachev, D. C. Elias, K. S. Novoselov, A. K. Geim, F. Guinea, Limits on charge carrier mobility in suspended graphene due to flexural phonons, Phys. Rev. Lett. 105 (2010) 266601. doi:10.1103/PhysRevLett.105.266601.
URL http://link.aps.org/doi/10.1103/PhysRevLett.105.266601
[242] M. Katsnelson, A. Geim, Electron scattering on microscopic corrugations in graphene, Phil. Trans. R. Soc. A 366 1863 (2008) 195–204.
[243] N. J. G. Couto, D. Costanzo, S. Engels, D.-K. Ki, K. Watanabe, T. Taniguchi, C. Stampfer, F. Guinea, A. F. Morpurgo, Random strain fluctuations as dominant disorder source for high-quality on-substrate graphene devices, Phys. Rev. X 4 (2014) 041019. doi:10.1103/PhysRevX.4.041019.
URL http://link.aps.org/doi/10.1103/PhysRevX.4.041019
[244] C. Dean, A. Young, I. Meric, C. Lee, L. Wang, S. Sorgenfrei, K. Watanabe, T. Taniguchi, P. Kim, K. Shepard, et al., Boron nitride substrates for high-quality graphene electronics, Nature nanotechnology 5 (10) (2010) 722–726.
[245] J. Xue, J. Sanchez-Yamagishi, D. Bulmash, P. Jacquod, A. Deshpande, K. Watanabe, T. Taniguchi, P. Jarillo-Herrero, B. J. LeRoy, Scanning tunnelling microscopy and spectroscopy of ultra-flat graphene on hexagonal boron nitride, Nature materials 10 (4) (2011) 282–285.
[246] R. Decker, Y. Wang, V. W. Brar, W. Regan, H.-Z. Tsai, Q. Wu, W. Gannett, A. Zettl, M. F. Crommie, Local electronic properties of graphene on a bn substrate via scanning tunneling microscopy, Nano letters 11 (6) (2011) 2291–2295.
[247] N. M. R. Peres, Colloquium, Rev. Mod. Phys. 82 (2010) 2673–2700. doi:10.1103/RevModPhys.82.2673.
URL http://link.aps.org/doi/10.1103/RevModPhys.82.2673
[248] S. Das Sarma, S. Adam, E. H. Hwang, E. Rossi, Electronic transport in two-dimensional graphene, Rev. Mod. Phys. 83 (2011) 407–470. doi:10.1103/RevModPhys.83.407.
URL http://link.aps.org/doi/10.1103/RevModPhys.83.407
[249] E. McCann, et al., Weak-localization magnetoresistance and valley symmetry in graphene, Phys. Rev. Lett. 97 (14) (2006) 146805–.
URL http://link.aps.org/doi/10.1103/PhysRevLett.97.146805

[250] A. F. Morpurgo, F. Guinea, Intervalley scattering, long-range disorder, and effective time-reversal symmetry breaking in graphene, Phys. Rev. Lett. 97 (19) (2006) 196804–.
URL http://link.aps.org/doi/10.1103/PhysRevLett.97.196804
[251] S. V. Morozov, K. S. Novoselov, M. I. Katsnelson, F. Schedin, L. A. Ponomarenko, D. Jiang, A. K. Geim, Strong suppression of weak localization in graphene, Phys. Rev. Lett. 97 (2006) 016801. doi:10.1103/PhysRevLett.97.016801.
URL http://link.aps.org/doi/10.1103/PhysRevLett.97.016801
[252] F. V. Tikhonenko, et al., Weak localization in graphene flakes, Phys. Rev. Lett. 100 (5) (2008) 056802–.
URL http://link.aps.org/doi/10.1103/PhysRevLett.100.056802
[253] F. V. Tikhonenko, et al., Transition between electron localization and antilocalization in graphene, Phys. Rev. Lett. 103 (22) (2009) 226801–.
URL http://link.aps.org/doi/10.1103/PhysRevLett.103.226801
[254] J. Martin, et al., Observation of electron-hole puddles in graphene using a scanning single-electron transistor, Nat. Phys. 4 (2) (2008) 144–148.
URL http://dx.doi.org/10.1038/nphys781
[255] K. Nomura, A. H. MacDonald, Quantum transport of massless dirac fermions, Phys. Rev. Lett. 98 (7) (2007) 076602–.
URL http://link.aps.org/doi/10.1103/PhysRevLett.98.076602
[256] E. H. Hwang, S. Adam, S. Das Sarma, Carrier transport in two-dimensional graphene layers, Phys. Rev. Lett. 98 (18) (2007) 186806–.
URL http://link.aps.org/doi/10.1103/PhysRevLett.98.186806
[257] S. Adam, et al., A self-consistent theory for graphene transport, Proc. Nat. Acad. Sci. 104 (47) (2007) 18392–18397.
[258] T. Stauber, N. M. R. Peres, F. Guinea, Electronic transport in graphene: A semiclassical approach including midgap states, Phys. Rev. B 76 (20) (2007) 205423–.
URL http://link.aps.org/doi/10.1103/PhysRevB.76.205423
[259] Z. H. Ni, et al., On resonant scatterers as a factor limiting carrier mobility in graphene, Nano Lett. 10 (10) (2010) 3868–3872. doi:10.1021/nl101399r.
URL http://dx.doi.org/10.1021/nl101399r
[260] C. Woods, L. Britnell, A. Eckmann, R. Ma, J. Lu, H. Guo, X. Lin, G. Yu, Y. Cao, R. Gorbachev, et al., Commensurate-incommensurate transition in graphene on hexagonal boron nitride, Nature Physics 10 (6) (2014) 451–456.
[261] J. Jung, A. Raoux, Z. Qiao, A. H. MacDonald, Ab initio, Phys. Rev. B 89 (2014) 205414. doi:10.1103/PhysRevB.89.205414.
URL http://link.aps.org/doi/10.1103/PhysRevB.89.205414
[262] P. San-Jose, A. Gutiérrez-Rubio, M. Sturla, F. Guinea, Spontaneous strains and gap in graphene on boron nitride, Phys. Rev. B 90 (2014) 075428. doi:10.1103/PhysRevB.90.075428.
URL http://link.aps.org/doi/10.1103/PhysRevB.90.075428
[263] T. Low, Y. Jiang, M. Katsnelson, F. Guinea, Electron pumping in graphene mechanical resonators, Nano Letters 12 (2) (2012) 850–854. doi:10.1021/nl2038985.
[264] J. S. Bunch, A. M. van der Zande, S. S. Verbridge, I. W. Frank, D. M. Tanenbaum, J. M. Parpia, H. G. Craighead, P. L. McEuen, Electromechanical resonators from graphene sheets, Science 315 (5811) (2007) 490–493. doi:10.1126/science.1136836.
[265] C. Chen, S. Lee, V. V. Deshpande, G.-H. Lee, M. Lekas, K. Shepard, J. Hone, Graphene mechanical oscillators with tunable frequency, Nat Nano 8 (12) (2013) 923–927. doi:10.1038/nnano.2013.232.
[266] A. M. van der Zande, R. A. Barton, J. S. Alden, C. S. Ruiz-Vargas, W. S. Whitney, P. H. Q. Pham, J. Park, J. M. Parpia, H. G. Craighead, P. L. McEuen, Large-scale arrays of single-layer graphene resonators, Nano Letters 10 (12) (2010) 4869–4873. doi:10.1021/nl102713c.
[267] S. Shivaraman, R. A. Barton, X. Yu, J. Alden, L. Herman, M. Chandrashekhar, J. Park, P. L. McEuen, J. M. Parpia, H. G. Craighead, M. G. Spencer, Free-standing epitaxial graphene, Nano Letters 9 (9) (2009) 3100–3105. doi:10.1021/nl900479g.
[268] H. G. Craighead, Nanoelectromechanical systems, Science 290 (5496) (2000) 1532–1535. doi:10.1126/science.290.5496.1532.
[269] M. Blencowe, Quantum electromechanical systems, Physics Reports 395 (3) (2004) 159 – 222. doi:10.1016/j.physrep.2003.12.005.
[270] K. L. Ekinci, M. L. Roukes, Nanoelectromechanical systems, Review of Scientific Instruments 76 (6) (2005) 061101. doi:10.1063/1.1927327.
[271] C. Chen, J. Hone, Graphene nanoelectromechanical systems, Proceedings of the IEEE 101 (7) (2013) 1766–1779. doi:10.1109/JPROC.2013.2253291.
[272] J. Atalaya, A. Isacsson, J. M. Kinaret, Continuum elastic modeling of graphene resonators, Nano Letters 8 (12) (2008) 4196–4200. doi:10.1021/nl801733d.
[273] N.-C. Yeh, M.-L. Teague, S. Yeom, B. L. Standley, R. T.-P. Wu, D. A. Boyd, M. W. Bockrath, Strain-induced pseudo-magnetic fields and charging effects on cvd-grown graphene, Surface Science 605 (2011) 1649.
[274] D. Guo, K. Takahiro, T. Machida, K. Iwatake, S. Okada, J. Nakamura, Observation of landau levels in potassium-intercalated graphite under a zero magnetic field, Nature Comm. 3 (2012) 1068.
[275] V. N. Kotov, B. Uchoa, V. M. Pereira, F. Guinea, A. H. Castro Neto, Electron-electron interactions in graphene: Current status and perspectives, Rev. Mod. Phys. 84 (2012) 1067–1125. doi:10.1103/RevModPhys.84.1067.
URL http://link.aps.org/doi/10.1103/RevModPhys.84.1067
[276] J. Gonzalez, F. Guinea, M. Vozmediano, Non-fermi liquid behavior of electrons in the half-filled honeycomb lattice

(a renormalization group approach), Nuclear Physics B 424 (3) (1994) 595 – 618. doi:http://dx.doi.org/10.1016/0550-3213(94)90410-3.

[277] J. González, F. Guinea, M. A. H. Vozmediano, Marginal-fermi-liquid behavior from two-dimensional coulomb interaction, Phys. Rev. B 59 (1999) R2474–R2477. doi:10.1103/PhysRevB.59.R2474.

[278] D. C. Elias, R. V. Gorbachev, A. S. Mayorov, S. V. Morozov, A. A. Zhukov, P. Blake, L. A. Ponomarenko, I. V. Grigorieva, K. S. Novoselov, F. Guinea, A. K. Geim, Dirac cones reshaped by interaction effects in suspended graphene, Nat. Phys. 7 (2011) 701.

[279] J. González, Kohn-luttinger superconductivity in graphene, Phys. Rev. B 78 (2008) 205431. doi:10.1103/PhysRevB.78.205431.
URL http://link.aps.org/doi/10.1103/PhysRevB.78.205431

[280] I. Martin, C. D. Batista, Itinerant electron-driven chiral magnetic ordering and spontaneous quantum hall effect in triangular lattice models, Phys. Rev. Lett. 101 (2008) 156402. doi:10.1103/PhysRevLett.101.156402.
URL http://link.aps.org/doi/10.1103/PhysRevLett.101.156402

[281] B. Valenzuela, M. A. H. Vozmediano, Pomeranchuk instability in doped graphene, New Journal of Physics 10 (11) (2008) 113009.
URL http://stacks.iop.org/1367-2630/10/i=11/a=113009

[282] D. Makogon, R. van Gelderen, R. Roldán, C. M. Smith, Spin-density-wave instability in graphene doped near the van hove singularity, Phys. Rev. B 84 (2011) 125404. doi:10.1103/PhysRevB.84.125404.
URL http://link.aps.org/doi/10.1103/PhysRevB.84.125404

[283] T. Li, Spontaneous quantum hall effect in quarter-doped hubbard model on honeycomb lattice and its possible realization in doped graphene system, EPL (Europhysics Letters) 97 (3) (2012) 37001.
URL http://stacks.iop.org/0295-5075/97/i=3/a=37001

[284] R. Nandkishore, L. S. Levitov, A. V. Chubukov, Chiral superconductivity from repulsive interactions in doped graphene, Nat Phys 8 (2) (2012) 158–163.
URL http://dx.doi.org/10.1038/nphys2208

[285] V. P. Gusynin, V. A. Miransky, S. G. Sharapov, I. A. Shovkovy, Excitonic gap, phase transition, and quantum hall effect in graphene, Phys. Rev. B 74 (2006) 195429. doi:10.1103/PhysRevB.74.195429.
URL http://link.aps.org/doi/10.1103/PhysRevB.74.195429

[286] I. Shovkovy, Magnetic catalysis: A review, in: D. Kharzeev, K. Landsteiner, A. Schmitt, H.-U. Yee (Eds.), Strongly Interacting Matter in Magnetic Fields, Vol. 871 of Lecture Notes in Physics, Springer Berlin Heidelberg, 2013, pp. 13–49. doi:10.1007/978-3-642-37305-3_2.
URL http://dx.doi.org/10.1007/978-3-642-37305-3_2

[287] I. F. Herbut, Pseudomagnetic catalysis of the time-reversal symmetry breaking in graphene, Phys. Rev. B 78 (2008) 205433. doi:10.1103/PhysRevB.78.205433.
URL http://link.aps.org/doi/10.1103/PhysRevB.78.205433

[288] B. Roy, I. F. Herbut, Topological insulators in strained graphene at weak interaction, Phys. Rev. B 88 (2013) 045425. doi:10.1103/PhysRevB.88.045425.
URL http://link.aps.org/doi/10.1103/PhysRevB.88.045425

[289] D. O. Rybalka, E. V. Gorbar, V. P. Gusynin, Gap generation and phase diagram in strained graphene in a magnetic field, ArXiv e-printsarXiv:1501.05156.

[290] F. Guinea, A. K. Geim, M. I. Katsnelson, K. S. Novoselov, Generating quantizing pseudomagnetic fields by bending graphene ribbons, Phys. Rev. B 81 (2010) 035408. doi:10.1103/PhysRevB.81.035408.
URL http://link.aps.org/doi/10.1103/PhysRevB.81.035408

[291] D. A. Abanin, D. A. Pesin, Interaction-induced topological insulator states in strained graphene, Phys. Rev. Lett. 109 (2012) 066802. doi:10.1103/PhysRevLett.109.066802.
URL http://link.aps.org/doi/10.1103/PhysRevLett.109.066802

[292] E. J. Bergholtz, Z. Liu, Topological flat band models and fractional chern insulators, Int. J. Mod. Phys. B 27 (2013) 1330017. doi:10.1142/S021797921330017X.

[293] P. Ghaemi, J. Cayssol, D. N. Sheng, A. Vishwanath, Fractional topological phases and broken time-reversal symmetry in strained graphene, Phys. Rev. Lett. 108 (2012) 266801. doi:10.1103/PhysRevLett.108.266801.
URL http://link.aps.org/doi/10.1103/PhysRevLett.108.266801

[294] H. Chen, K. Yang, Interaction-driven quantum phase transitions in fractional topological insulators, Phys. Rev. B 85 (2012) 195113. doi:10.1103/PhysRevB.85.195113.
URL http://link.aps.org/doi/10.1103/PhysRevB.85.195113

[295] S. Raghu, X.-L. Qi, C. Honerkamp, S.-C. Zhang, Topological mott insulators, Phys. Rev. Lett. 100 (2008) 156401. doi:10.1103/PhysRevLett.100.156401.
URL http://link.aps.org/doi/10.1103/PhysRevLett.100.156401

[296] B. Roy, J. D. Sau, Competing charge-density wave, magnetic, and topological ground states at and near dirac points in graphene in axial magnetic fields, Phys. Rev. B 90 (2014) 075427. doi:10.1103/PhysRevB.90.075427.
URL http://link.aps.org/doi/10.1103/PhysRevB.90.075427

[297] C. Weeks, M. Franz, Interaction-driven instabilities of a dirac semimetal, Phys. Rev. B 81 (2010) 085105. doi:10.1103/PhysRevB.81.085105.
URL http://link.aps.org/doi/10.1103/PhysRevB.81.085105

[298] A. G. Grushin, E. V. Castro, A. Cortijo, F. de Juan, M. A. H. Vozmediano, B. Valenzuela, Charge instabilities and topological phases in the extended hubbard model on the honeycomb lattice with enlarged unit cell, Phys. Rev. B 87

(2013) 085136. doi:10.1103/PhysRevB.87.085136.
URL http://link.aps.org/doi/10.1103/PhysRevB.87.085136
[299] N. A. Garcia-Martinez, A. G. Grushin, T. Neupert, B. Valenzuela, E. V. Castro, Interaction-driven phases in the half-filled spinless honeycomb lattice from exact diagonalization, Phys. Rev. B 88 (2013) 245123. doi:10.1103/PhysRevB.88.245123.
URL http://link.aps.org/doi/10.1103/PhysRevB.88.245123
[300] M. Daghofer, M. Hohenadler, Phases of correlated spinless fermions on the honeycomb lattice, Phys. Rev. B 89 (2014) 035103. doi:10.1103/PhysRevB.89.035103.
URL http://link.aps.org/doi/10.1103/PhysRevB.89.035103
[301] T. DJuric, N. Chancellor, I. F. Herbut, Interaction-induced anomalous quantum hall state on the honeycomb lattice, Phys. Rev. B 89 (2014) 165123. doi:10.1103/PhysRevB.89.165123.
URL http://link.aps.org/doi/10.1103/PhysRevB.89.165123
[302] B. Roy, Odd integer quantum hall effect in graphene, Phys. Rev. B 84 (2011) 035458. doi:10.1103/PhysRevB.84.035458.
URL http://link.aps.org/doi/10.1103/PhysRevB.84.035458
[303] B. Roy, Z.-X. Hu, K. Yang, Theory of unconventional quantum hall effect in strained graphene, Phys. Rev. B 87 (2013) 121408. doi:10.1103/PhysRevB.87.121408.
[304] O. Vafek, Z. Tešanović, M. Franz, Relativity restored: Dirac anisotropy in qed_3, Phys. Rev. Lett. 89 (2002) 157003. doi:10.1103/PhysRevLett.89.157003.
URL http://link.aps.org/doi/10.1103/PhysRevLett.89.157003
[305] D. J. Lee, I. F. Herbut, Velocity anisotropy and the antiferromagnetic instability in the qed_3 theory of underdoped cuprates, Phys. Rev. B 66 (2002) 094512. doi:10.1103/PhysRevB.66.094512.
URL http://link.aps.org/doi/10.1103/PhysRevB.66.094512
[306] A. Sharma, V. N. Kotov, A. H. Castro Neto, Interacting Anisotropic Dirac Fermions in Strained Graphene and Related Systems, ArXiv e-printsarXiv:1206.5427.
[307] N. M. R. Peres, F. Guinea, A. H. Castro Neto, Coulomb interactions and ferromagnetism in pure and doped graphene, Phys. Rev. B 72 (2005) 174406. doi:10.1103/PhysRevB.72.174406.
URL http://link.aps.org/doi/10.1103/PhysRevB.72.174406
[308] A. Sharma, V. N. Kotov, A. H. Castro Neto, Effect of uniaxial strain on ferromagnetic instability and formation of localized magnetic states on adatoms in graphene, Phys. Rev. B 87 (2013) 155431. doi:10.1103/PhysRevB.87.155431.
URL http://link.aps.org/doi/10.1103/PhysRevB.87.155431
[309] A. Sharma, P. Harnish, A. Sylvester, V. N. Kotov, A. H. C. Neto, van der waals forces and electron-electron interactions in two strained graphene layers, Phys. Rev. B 89 (2014) 235425. doi:10.1103/PhysRevB.89.235425.
URL http://link.aps.org/doi/10.1103/PhysRevB.89.235425
[310] B. Roy, F. F. Assaad, I. F. Herbut, Zero modes and global antiferromagnetism in strained graphene, Phys. Rev. X 4 (2014) 021042. doi:10.1103/PhysRevX.4.021042.
URL http://link.aps.org/doi/10.1103/PhysRevX.4.021042
[311] T. O. Wehling, E. Sasioglu, C. Friedrich, A. I. Lichtenstein, M. I. Katsnelson, S. Blügel, Strength of effective coulomb interactions in graphene and graphite, Phys. Rev. Lett. 106 (2011) 236805. doi:10.1103/PhysRevLett.106.236805.
URL http://link.aps.org/doi/10.1103/PhysRevLett.106.236805
[312] P. Ghaemi, S. Gopalakrishnan, S. Ryu, Stability of edge states in strained graphene, Phys. Rev. B 87 (2013) 155422. doi:10.1103/PhysRevB.87.155422.
URL http://link.aps.org/doi/10.1103/PhysRevB.87.155422
[313] S. Cheng, J. Yu, T. Ma, N. M. R. Peres, Strain induced edge magnetism at zigzag edge in graphene quantum dot, ArXiv e-printsarXiv:1409.2341.
[314] R. G. Melko, A. Paramekanti, A. A. Burkov, A. Vishwanath, D. N. Sheng, L. Balents, Supersolid order from disorder: Hard-core bosons on the triangular lattice, Phys. Rev. Lett. 95 (2005) 127207. doi:10.1103/PhysRevLett.95.127207.
URL http://link.aps.org/doi/10.1103/PhysRevLett.95.127207
[315] B. Uchoa, Y. Barlas, Superconducting states in pseudo-landau-levels of strained graphene, Phys. Rev. Lett. 111 (2013) 046604. doi:10.1103/PhysRevLett.111.046604.
URL http://link.aps.org/doi/10.1103/PhysRevLett.111.046604
[316] B. Roy, V. Juricic, Strain-induced time-reversal odd superconductivity in graphene, Phys. Rev. B 90 (2014) 041413. doi:10.1103/PhysRevB.90.041413.
URL http://link.aps.org/doi/10.1103/PhysRevB.90.041413
[317] T. M. G. Mohiuddin, A. Lombardo, R. R. Nair, A. Bonetti, G. Savini, R. Jalil, N. Bonini, D. M. Basko, C. Galiotis, N. Marzari, K. S. Novoselov, A. K. Geim, A. C. Ferrari, Uniaxial strain in graphene by raman spectroscopy: G peak splitting, grüneisen parameters, and sample orientation, Phys. Rev. B 79 (2009) 205433. doi:10.1103/PhysRevB.79.205433.
[318] M. Liu, X. Yin, E. Ulin-Avila, B. Geng, T. Zentgraf, L. Ju, F. Wang, X. Zhang, A graphene-based broadband optical modulator, Nature 474 (7349) (2011) 64–67. doi:10.1038/nature10067.
[319] M. Tamagnone, A. Fallahi, J. R. Mosig, J. Perruisseau-Carrier, Fundamental limits and near-optimal design of graphene modulators and non-reciprocal devices, Nat Photon 8 (7) (2014) 556–563. doi:10.1038/nphoton.2014.109.
[320] M. Huang, H. Yan, T. F. Heinz, J. Hone, Probing strain-induced electronic structure change in graphene by raman spectroscopy, Nano Letters 10 (10) (2010) 4074–4079. doi:10.1021/nl102123c.
[321] A. C. Ferrari, D. M. Basko, Raman spectroscopy as a versatile tool for studying the properties of graphene, Nature Nanotechnology 8 (4) (2013) 235–246. doi:10.1038/nnano.2013.46.
[322] M. Huang, H. Yan, C. Chen, D. Song, T. F. Heinz, J. Hone, Phonon softening and crystallographic orientation of strained

graphene studied by raman spectroscopy, Proceedings of the National Academy of Sciences 106 (18) (2009) 7304–7308. doi:10.1073/pnas.0811754106.
[323] F. Schedin, E. Lidorikis, A. Lombardo, V. G. Kravets, A. K. Geim, A. N. Grigorenko, K. S. Novoselov, A. C. Ferrari, Surface-enhanced raman spectroscopy of graphene, ACS Nano 4 (10) (2010) 5617–5626. doi:10.1021/nn1010842.
[324] S. Heeg, R. Fernandez-Garcia, A. Oikonomou, F. Schedin, R. Narula, S. A. Maier, A. Vijayaraghavan, S. Reich, Polarized plasmonic enhancement by au nanostructures probed through raman scattering of suspended graphene, Nano Letters 13 (1) (2013) 301–308. doi:10.1021/nl3041542.
[325] L. Novotny, B. Hecht, Principles of Nano-Optics, Cambridge University Press, 2012.
[326] A. Y. Nikitin, F. Guinea, F. J. Garcia-Vidal, L. Martin-Moreno, Fields radiated by a nanoemitter in a graphene sheet, Phys. Rev. B 84 (2011) 195446. doi:10.1103/PhysRevB.84.195446.
[327] B. Wunsch, T. Stauber, F. Sols, F. Guinea, Dynamical polarization of graphene at finite doping, New Journal of Physics 8 (12) (2006) 318.
URL http://stacks.iop.org/1367-2630/8/i=12/a=318
[328] E. H. Hwang, S. Das Sarma, Dielectric function, screening, and plasmons in two-dimensional graphene, Phys. Rev. B 75 (2007) 205418. doi:10.1103/PhysRevB.75.205418.
[329] K. F. Mak, M. Y. Sfeir, Y. Wu, C. H. Lui, J. A. Misewich, T. F. Heinz, Measurement of the optical conductivity of graphene, Phys. Rev. Lett. 101 (2008) 196405. doi:10.1103/PhysRevLett.101.196405.
[330] R. R. Nair, P. Blake, A. N. Grigorenko, K. S. Novoselov, T. J. Booth, T. Stauber, N. M. R. Peres, A. K. Geim, Fine structure constant defines visual transparency of graphene, Science 320 (5881) (2008) 1308. doi:10.1126/science.1156965.
[331] M. Jablan, H. Buljan, M. Soljačić, Plasmonics in graphene at infrared frequencies, Phys. Rev. B 80 (2009) 245435. doi:10.1103/PhysRevB.80.245435.
[332] T. Low, P. Avouris, Graphene plasmonics for terahertz to mid-infrared applications, ACS Nano 8 (2) (2014) 1086–1101. doi:10.1021/nn406627u.
[333] F. H. L. Koppens, D. E. Chang, F. J. García de Abajo, Graphene plasmonics: A platform for strong lightmatter interactions, Nano Letters 11 (8) (2011) 3370–3377. doi:10.1021/nl201771h.
[334] G.-X. Ni, H.-Z. Yang, W. Ji, S.-J. Baeck, C.-T. Toh, J.-H. Ahn, V. M. Pereira, B. zyilmaz, Tuning optical conductivity of large-scale CVD graphene by strain engineering, Advanced Materials 26 (7) (2014) 1081–1086. doi:10.1002/adma.201304156.
URL http://dx.doi.org/10.1002/adma.201304156
[335] J. Kim, C. Lee, S. Bae, S. Jin Kim, K. Soo Kim, B. Hee Hong, E. J. Choi, Effect of uni-axial strain on thz/far-infrared response of graphene, Applied Physics Letters 100 (4) (2012) 041910. doi:10.1063/1.3680095.
[336] K. S. Kim, Y. Zhao, H. Jang, S. Y. Lee, J. M. Kim, K. S. Kim, J.-H. Ahn, P. Kim, J.-Y. Choi, B. H. Hong, Large-scale pattern growth of graphene films for stretchable transparent electrodes, Nature 457 (7230) (2009) 706–710. doi:10.1038/nature07719.
[337] F. M. D. Pellegrino, G. G. N. Angilella, R. Pucci, Dynamical polarization of graphene under strain, Phys. Rev. B 82 (2010) 115434. doi:10.1103/PhysRevB.82.115434.
[338] V. K. Dugaev, M. I. Katsnelson, Graphene in periodic deformation fields: Dielectric screening and plasmons, Phys. Rev. B 86 (2012) 115405. doi:10.1103/PhysRevB.86.115405.
[339] J. P. F. LeBlanc, J. P. Carbotte, Effect of dynamical screening on single-particle spectral features of uniaxially strained graphene: Tuning the plasmaron ring, Phys. Rev. B 87 (2013) 205407. doi:10.1103/PhysRevB.87.205407.
[340] Y. Lu, J. Guo, Band gap of strained graphene nanoribbons, Nano Research 3 (3) (2010) 189–199. doi:10.1007/s12274-010-1022-4.
[341] Y. Jia, Y. Gao, Optical properties of armchair graphene nanoribbons under uniaxial strain, physica status solidi (b) 251 (6) (2014) 1252–1256. doi:10.1002/pssb.201350423.
[342] D. L. Sounas, C. Caloz, Electromagnetic nonreciprocity and gyrotropy of graphene, Applied Physics Letters 98 (2011) 021911. doi:http://dx.doi.org/10.1063/1.3543633.
[343] V. P. Gusynin, S. G. Sharapov, Transport of Dirac quasiparticles in graphene: Hall and optical conductivities, Phys. Rev. B 73 (2006) 245411. doi:10.1103/PhysRevB.73.245411.
[344] V. P. Gusynin, S. G. Sharapov, J. P. Carbotte, Unusual microwave response of dirac quasiparticles in graphene, Phys. Rev. Lett. 96 (2006) 256802. doi:10.1103/PhysRevLett.96.256802.
[345] I. Fialkovsky, D. Vassilevich, Faraday rotation in graphene, The European Physical Journal B 85 (11) (2012) 1–10. doi:10.1140/epjb/e2012-30685-9.
[346] M. L. Sadowski, G. Martinez, M. Potemski, C. Berger, W. A. de Heer, Landau level spectroscopy of ultrathin graphite layers, Phys. Rev. Lett. 97 (2006) 266405. doi:10.1103/PhysRevLett.97.266405.
[347] Z. Jiang, E. A. Henriksen, L. C. Tung, Y.-J. Wang, M. E. Schwartz, M. Y. Han, P. Kim, H. L. Stormer, Infrared spectroscopy of landau levels of graphene, Phys. Rev. Lett. 98 (2007) 197403. doi:10.1103/PhysRevLett.98.197403.
[348] D.-B. Zhang, G. Seifert, K. Chang, Strain-induced pseudomagnetic fields in twisted graphene nanoribbons, Phys. Rev. Lett. 112 (2014) 096805. doi:10.1103/PhysRevLett.112.096805.
[349] Bi Lei, Hu Juejun, Jiang Peng, Kim Dong Hun, Dionne Gerald F., Kimerling Lionel C., R. A., On-chip optical isolation in monolithically integrated non-reciprocal optical resonators, Nat Photon 5 (12) (2011) 758–762, http://www.nature.com/nphoton/journal/v5/n12/abs/nphoton.2011.270.html#supplementary-information. doi:10.1038/nphoton.2011.270.
URL http://dx.doi.org/10.1038/nphoton.2011.270
[350] T. Low, F. Guinea, Strain-induced pseudomagnetic field for novel graphene electronics, Nano Letters 10 (9) (2010)

3551–3554. doi:10.1021/nl1018063.
[351] J. S. Alden, A. W. Tsen, P. Y. Huang, R. Hovden, L. Brown, J. Park, D. A. Muller, P. L. McEuen, Strain solitons and topological defects in bilayer graphene, Proceedings of the National Academy of Sciences 110 (28) (2013) 11256–11260.
[352] Z. Y. Rong, P. Kuiper, Electronic effects in scanning tunneling microscopy: Moiré pattern on a graphite surface, Physical Review B 48 (23) (1993) 17427.
[353] P. Poncharal, A. Ayari, T. Michel, J.-L. Sauvajol, Raman spectra of misoriented bilayer graphene, Physical Review B 78 (11) (2008) 113407.
[354] A. Luican, G. Li, A. Reina, J. Kong, R. R. Nair, K. S. Novoselov, A. K. Geim, E. Y. Andrei, Single-layer behavior and its breakdown in twisted graphene layers, Phys. Rev. Lett. 106 (12) (2011) 126802.
[355] I. Brihuega, P. Mallet, H. González-Herrero, G. Trambly de Laissardière, M. M. Ugeda, L. Magaud, J. M. Gómez-Rodríguez, F. Ynduráin, J.-Y. Veuillen, Unraveling the intrinsic and robust nature of van hove singularities in twisted bilayer graphene by scanning tunneling microscopy and theoretical analysis, Phys. Rev. Lett. 109 (2012) 196802.
[356] E. Y. Andrei, G. Li, X. Du, Electronic properties of graphene: a perspective from scanning tunneling microscopy and magnetotransport, Rep. Prog. Phys. 75 (5) (2012) 056501.
[357] K. Kim, S. Coh, L. Z. Tan, W. Regan, J. M. Yuk, E. Chatterjee, M. F. Crommie, M. L. Cohen, S. G. Louie, A. Zettl, Raman spectroscopy study of rotated double-layer graphene: Misorientation-angle dependence of electronic structure, Phys. Rev. Lett. 108 (2012) 246103.
[358] L. A. Ponomarenko, R. V. Gorbachev, G. L. Yu, D. C. Elias, R. Jalil, A. A. Patel, A. Mishchenko, A. S. Mayorov, C. R. Woods, J. R. Wallbank, M. Mucha-Kruczynski, B. A. Piot, M. Potemski, I. V. Grigorieva, K. S. Novoselov, F. Guinea, V. I. Fal'ko, A. K. Geim, Cloning of dirac fermions in graphene superlattices, Nature 497 (7451) (2013) 594–597.
[359] C. R. Dean, L. Wang, P. Maher, C. Forsythe, F. Ghahari, Y. Gao, J. Katoch, M. Ishigami, P. Moon, M. Koshino, T. Taniguchi, K. Watanabe, K. L. Shepard, J. Hone, P. Kim, Hofstadter/'s butterfly and the fractal quantum hall effect in moire superlattices, Nature 497 (7451) (2013) 598–602.
[360] P. San-Jose, J. González, F. Guinea, Non-abelian gauge potentials in graphene bilayers, Phys. Rev. Lett. 108 (2012) 216802.
[361] P. San-Jose, E. Prada, Helical networks in twisted bilayer graphene under interlayer bias, Phys. Rev. B 88 (2013) 121408.
[362] P. San-Jose, R. V. Gorbachev, A. K. Geim, K. S. Novoselov, F. Guinea, Stacking boundaries and transport in bilayer graphene, Nano Letters 14 (4) (2014) 2052–2057.
[363] T. Löfwander, P. San-Jose, E. Prada, Quantum hall effect in graphene with twisted bilayer stripe defects, Phys. Rev. B 87 (2013) 205429.
[364] C. H. Lui, Z. Ye, C. Keiser, E. B. Barros, R. He, Stacking-dependent shear modes in trilayer graphene, Applied Physics Letters 106 (4) (2015) –.
[365] M. Yankowitz, J. I.-J. Wang, A. G. Birdwell, Y.-A. Chen, K. Watanabe, T. Taniguchi, P. Jacquod, P. San-Jose, P. Jarillo-Herrero, B. J. LeRoy, Electric field control of soliton motion and stacking in trilayer graphene, Nat Mater 13 (8) (2014) 786–789.
[366] J. Hicks, M. Sprinkle, K. Shepperd, F. Wang, A. Tejeda, A. Taleb-Ibrahimi, F. Bertran, P. Le Fèvre, W. A. de Heer, C. Berger, E. H. Conrad, Symmetry breaking in commensurate graphene rotational stacking: Comparison of theory and experiment, Phys. Rev. B 83 (2011) 205403.
[367] W. Yan, M. Liu, R.-F. Dou, L. Meng, L. Feng, Z.-D. Chu, Y. Zhang, Z. Liu, J.-C. Nie, L. He, Angle-dependent van hove singularities in a slightly twisted graphene bilayer, Phys. Rev. Lett. 109 (2012) 126801.
[368] L. Britnell, R. V. Gorbachev, R. Jalil, B. D. Belle, F. Schedin, M. I. Katsnelson, L. Eaves, S. V. Morozov, A. S. Mayorov, N. M. Peres, et al., Electron tunneling through ultrathin boron nitride crystalline barriers, Nano letters 12 (3) (2012) 1707–1710.
[369] A. M. van der Zande, J. Kunstmann, A. Chernikov, D. A. Chenet, Y. You, X. Zhang, P. Y. Huang, T. C. Berkelbach, L. Wang, F. Zhang, M. S. Hybertsen, D. A. Muller, D. R. Reichman, T. F. Heinz, J. C. Hone, Tailoring the electronic structure in bilayer molybdenum disulfide via interlayer twist, Nano Letters 14 (7) (2014) 3869–3875.
[370] S. Aubry, The twist map, the extended frenkel-kontorova model and the devil's staircase, Physica D: Nonlinear Phenomena 7 (1) (1983) 240–258.
[371] S. Aubry, P.-Y. Le Daeron, The discrete frenkel-kontorova model and its extensions: I. exact results for the ground-states, Physica D: Nonlinear Phenomena 8 (3) (1983) 381–422.
[372] O. M. Braun, Y. S. Kivshar, The Frenkel-Kontorova model: concepts, methods, and applications, Springer, 2004.
[373] R. Bistritzer, A. H. MacDonald, Transport between twisted graphene layers, Physical Review B 81 (24) (2010) 245412.
[374] M. Mucha-Kruczyński, J. Wallbank, V. Fal'Ko, Heterostructures of bilayer graphene and h-bn: Interplay between misalignment, interlayer asymmetry, and trigonal warping, Physical Review B 88 (20) (2013) 205418.
[375] J. Wallbank, A. Patel, M. Mucha-Kruczyński, A. Geim, V. Fal'ko, Generic miniband structure of graphene on a hexagonal substrate, Physical Review B 87 (24) (2013) 245408.
[376] M. Yankowitz, J. Xue, D. Cormode, J. D. Sanchez-Yamagishi, K. Watanabe, T. Taniguchi, P. Jarillo-Herrero, P. Jacquod, B. J. LeRoy, Emergence of superlattice dirac points in graphene on hexagonal boron nitride, Nature Physics 8 (5) (2012) 382–386. doi:10.1038/nphys2272.
[377] J. L. dos Santos, N. Peres, A. C. Neto, Continuum model of the twisted graphene bilayer, Physical Review B 86 (15) (2012) 155449.
[378] E. J. Mele, Band symmetries and singularities in twisted multilayer graphene, Physical Review B 84 (23) (2011) 235439.
[379] J. L. Dos Santos, N. Peres, A. C. Neto, Graphene bilayer with a twist: Electronic structure, Physical review letters 99 (25) (2007) 256802.
[380] M. Bokdam, T. Amlaki, G. Brocks, P. J. Kelly, Band gaps in incommensurable graphene on hexagonal boron nitride,

Physical Review B 89 (20) (2014) 201404.
[381] G. Giovannetti, P. A. Khomyakov, G. Brocks, P. J. Kelly, J. van den Brink, Substrate-induced band gap in graphene on hexagonal boron nitride: Ab initio density functional calculations, Physical Review B 76 (7) (2007) 073103.
[382] J. Jung, A. DaSilva, A. H. MacDonald, S. Adam, Origin of band gaps in graphene on hexagonal boron nitride, arXiv:1403.0496.
[383] J. C. Song, A. V. Shytov, L. S. Levitov, Electron interactions and gap opening in graphene superlattices, Physical review letters 111 (26) (2013) 266801.
[384] P. San-Jose, A. Gutiérrez-Rubio, M. Sturla, F. Guinea, Electronic structure of spontaneously strained graphene on hexagonal boron nitride, Phys. Rev. B 90 (2014) 115152. doi:10.1103/PhysRevB.90.115152.
URL http://link.aps.org/doi/10.1103/PhysRevB.90.115152
[385] S. Bruzzone, G. Fiori, Ab-initio simulations of deformation potentials and electron mobility in chemically modified graphene and two-dimensional hexagonal boron-nitride, Applied Physics Letters 99 (22) (2011) 222108.
[386] A. M. Popov, I. V. Lebedeva, A. A. Knizhnik, Y. E. Lozovik, B. V. Potapkin, Commensurate-incommensurate phase transition in bilayer graphene, Physical Review B 84 (4) (2011) 045404.
[387] B. Hunt, J. D. Sanchez-Yamagishi, A. F. Young, M. Yankowitz, B. J. LeRoy, K. Watanabe, T. Taniguchi, P. Moon, M. Koshino, P. Jarillo-Herrero, R. C. Ashoori, Massive dirac fermions and hofstadter butterfly in a van der waals heterostructure, Science 340 (6139) (2013) 1427–1430. doi:10.1126/science.1237240.
URL http://www.sciencemag.org/content/340/6139/1427.full.pdf
[388] K. S. Novoselov, D. Jiang, F. Schedin, T. J. Booth, V. V. Khotkevich, S. V. Morozov, A. K. Geim, Two-dimensional atomic crystals, Proc. Natl. Acad. Sci. USA 102 (30) (2005) 10451–10453.
[389] K. F. Mak, C. Lee, J. Hone, J. Shan, T. F. Heinz, Atomically thin mos_2: A new direct-gap semiconductor, Phys. Rev. Lett. 105 (2010) 136805.
[390] S. P. Koenig, R. A. Doganov, H. Schmidt, A. C. Neto, B. Oezyilmaz, Electric field effect in ultrathin black phosphorus, Applied Physics Letters 104 (10) (2014) 103106.
[391] Y. Shi, C. Hamsen, X. Jia, K. K. Kim, A. Reina, M. Hofmann, A. L. Hsu, K. Zhang, H. Li, Z.-Y. Juang, et al., Synthesis of few-layer hexagonal boron nitride thin film by chemical vapor deposition, Nano letters 10 (10) (2010) 4134–4139.
[392] Y.-H. Lee, X.-Q. Zhang, W. Zhang, M.-T. Chang, C.-T. Lin, K.-D. Chang, Y.-C. Yu, J. T.-W. Wang, C.-S. Chang, L.-J. Li, et al., Synthesis of large-area mos2 atomic layers with chemical vapor deposition, Advanced Materials 24 (17) (2012) 2320–2325.
[393] A. Castellanos-Gomez, M. Barkelid, A. Goossens, V. E. Calado, H. S. van der Zant, G. A. Steele, Laser-thinning of mos2: On demand generation of a single-layer semiconductor, Nano letters 12 (6) (2012) 3187–3192.
[394] A. Castellanos-Gomez, V. Singh, H. S. J. van der Zant, G. A. Steele, Mechanics of freely-suspended ultrathin layered materials, Annalen der Physik 527 (1-2) (2015) 27–44. doi:10.1002/andp.201400153.
URL http://dx.doi.org/10.1002/andp.201400153
[395] J. Li, Z. Shan, E. Ma, Elastic strain engineering for unprecedented materials properties, MRS Bulletin 39 (02) (2014) 108–114.
[396] A. Castellanos-Gomez, R. Roldán, E. Cappelluti, M. Buscema, F. Guinea, H. S. J. van der Zant, G. A. Steele, Local strain engineering in atomically thin mos2, Nano Letters 13 (2013) 5361.
[397] Q. H. Wang, K. Kalantar-Zadeh, A. Kis, J. N. Coleman, M. S. Strano, Electronics and optoelectronics of two-dimensional transition metal dichalcogenides, Nature Nanotech. 7 (2012) 699.
[398] D. Jariwala, V. K. Sangwan, L. J. Lauhon, T. J. Marks, M. C. Hersam, Emerging device applications for semiconducting two-dimensional transition metal dichalcogenides, ACS nano 8 (2) (2014) 1102–1120.
[399] X. Xu, W. Yao, D. Xiao, T. F. Heinz, Spin and pseudospins in layered transition metal dichalcogenides, Nature Physics 10 (5) (2014) 343–350.
[400] R. Roldán, J. A. Silva-Guillén, M. P. López-Sancho, F. Guinea, E. Cappelluti, P. Ordejón, Electronic properties of single-layer and multilayer transition metal dichalcogenides mx2 (m = mo, w and x = s, se), Ann. Phy. (Berlin) 526 (9-10) (2014) 347–357.
[401] C. Lee, H. Yan, L. E. Brus, T. F. Heinz, J. Hone, S. Ryu, Anomalous lattice vibrations of single- and few-layer mos2, ACS Nano 4 (5) (2010) 2695–2700.
[402] H. J. Conley, B. Wang, J. I. Ziegler, R. F. Haglund, S. T. Pantelides, K. I. Bolotin, Bandgap engineering of strained monolayer and bilayer mos2, Nano Letters 13 (8) (2013) 3626–3630.
[403] Y. Y. Hui, X. Liu, W. Jie, N. Y. Chan, J. Hao, Y.-T. Hsu, L.-J. Li, W. Guo, S. P. Lau, Exceptional tunability of band energy in a compressively strained trilayer mos2 sheet, ACS Nano 7 (8) (2013) 7126–7131.
[404] H. Peelaers, C. G. Van de Walle, Effects of strain on band structure and effective masses in mos 2, Phys. Rev. B 86 (24) (2012) 241401.
[405] H. Shi, H. Pan, Y.-W. Zhang, B. I. Yakobson, Quasiparticle band structures and optical properties of strained monolayer mos2 and ws2, Phys. Rev. B 87 (2013) 155304.
[406] E. Scalise, M. Houssa, G. Pourtois, V. Afanasév, A. Stesmans, Strain-induced semiconductor to metal transition in the two-dimensional honeycomb structure of mos2, Nano Research 5 (1) (2012) 43–48.
[407] Z. Huang, C. He, X. Qi, H. Yang, W. Liu, X. Wei, X. Peng, J. Zhong, Band structure engineering of monolayer mos 2 on h-bn: first-principles calculations, Journal of Physics D: Applied Physics 47 (7) (2014) 075301.
[408] M. A. Cazalilla, H. Ochoa, F. Guinea, Quantum spin hall effect in two-dimensional crystals of transition-metal dichalcogenides, Phys. Rev. Lett. 113 (2014) 077201.
[409] X. Qian, Junwei, L. Fu, J. Li, Quantum spin hall effect in two-dimensional transition metal dichalcogenides, Science 346 (2014) 1344.

[410] H. Rostami, R. Roldán, E. Cappelluti, R. Asgari, F. Guinea, Theory of strain in single-layer transition metal dichalcogenides, Phys. Rev. B 92 (2015) 195402. doi:10.1103/PhysRevB.92.195402.
URL http://link.aps.org/doi/10.1103/PhysRevB.92.195402
[411] X. Dou, K. Ding, D. Jiang, B. Sun, Tuning and identification of interband transitions in monolayer and bilayer molybdenum disulfide using hydrostatic pressure, ACS nano 8 (7) (2014) 7458–7464.
[412] L. Yang, X. Cui, J. Zhang, K. Wang, M. Shen, S. Zeng, S. A. Dayeh, L. Feng, B. Xiang, Lattice strain effects on the optical properties of mos2 nanosheets, Scientific reports 4.
[413] J. Feng, X. Qian, Junwei, C. Huang, J. Li, Quantum spin hall effect in two-dimensional transition metal dichalcogenides, Nature Photonics (2012) 866.
[414] E. Cappelluti, R. Roldán, J. Silva-Guillén, P. Ordejón, F. Guinea, Tight-binding model and direct-gap/indirect-gap transition in single-layer and multilayer mos 2, Physical Review B 88 (7) (2013) 075409.
[415] R. Roldán, M. P. López-Sancho, F. Guinea, E. Cappelluti, J. A. Silva-Guillén, P. Ordejón, Momentum dependence of spinorbit interaction effects in single-layer and multi-layer transition metal dichalcogenides, 2D Materials 1 (3) (2014) 034003.
[416] H. Li, A. W. Contryman, X. Qian, S. M. Ardakani, Y. Gong, X. Wang, J. M. Weisse, C. H. Lee, J. Zhao, P. M. Ajayan, J. Li, H. C. Manoharan, X. Zheng, Optoelectronic crystal of artificial atoms in strain-textured molybdenum disulphide, Nat Commun 6. doi:10.1038/ncomms8381.
URL http://dx.doi.org/10.1038/ncomms8381
[417] Wu Wenzhuo, Wang Lei, Li Yilei, Zhang Fan, Lin Long, Niu Simiao, Chenet Daniel, Zhang Xian, Hao Yufeng, Heinz Tony F., Hone James, Wang Zhong Lin, Piezoelectricity of single-atomic-layer MoS2 for energy conversion and piezotronics, Nature 514 (7523) (2014) 470–474. doi:10.1038/nature13792.
URL http://dx.doi.org/10.1038/nature13792
[418] A. S. Rodin, A. Carvalho, A. H. Castro Neto, Strain-induced gap modification in black phosphorus, Phys. Rev. Lett. 112 (2014) 176801.
[419] H. Liu, A. T. Neal, Z. Zhu, Z. Luo, X. Xu, D. Tománek, P. D. Ye, Phosphorene: An unexplored 2d semiconductor with a high hole mobility, ACS nano 8 (4) (2014) 4033–4041.
[420] L. Li, Y. Yu, G. J. Ye, Q. Ge, X. Ou, H. Wu, D. Feng, X. H. Chen, Y. Zhang, Black phosphorus field-effect transistors, Nature Nanotechnology 9 (2014) 372.
[421] L. Cartz, S. Srinivasa, R. Riedner, J. Jorgensen, T. Worlton, Effect of pressure on bonding in black phosphorus, The Journal of Chemical Physics 71 (4) (1979) 1718–1721.
[422] H. Asahina, K. Shindo, A. Morita, Electronic structure of black phosphorus in self-consistent pseudopotential approach, Journal of the Physical Society of Japan 51 (4) (1982) 1193–1199.
[423] G. Seifert, E. Hernandez, Theoretical prediction of phosphorus nanotubes, Chemical Physics Letters 318 (4) (2000) 355–360.
[424] X. Peng, Q. Wei, A. Copple, Strain-engineered direct-indirect band gap transition and its mechanism in two-dimensional phosphorene, Phys. Rev. B 90 (2014) 085402.
[425] Q. Wei, X. Peng, Superior mechanical flexibility of phosphorene and few-layer black phosphorus, Applied Physics Letters 104 (25) (2014) 251915.
[426] A. Manjanath, A. Samanta, T. Pandey, A. K. Singh, Semiconductor to metal transition in bilayer phosphorene under normal compressive strain, Nanotechnology 26 (7) (2015) 075701.
URL http://stacks.iop.org/0957-4484/26/i=7/a=075701
[427] F. Xia, H. Wang, Y. Jia, Rediscovering black phosphorus: A unique anisotropic 2d material for optoelectronics and electronics, Nature Comm. 5 (2014) 4458.
[428] T. Low, R. Roldán, H. Wang, F. Xia, P. Avouris, L. M. Moreno, F. Guinea, Plasmons and screening in monolayer and multilayer black phosphorus, Phys. Rev. Lett. 113 (2014) 106802.
[429] R. Fei, L. Yang, Lattice vibrational modes and raman scattering spectra of strained phosphorene, Applied Physics Letters 105 (8) (2014) 083120.
[430] M. Elahi, K. Khaliji, S. M. Tabatabaei, M. Pourfath, R. Asgari, Modulation of electronic and mechanical properties of phosphorene through strain, Phys. Rev. B 91 (2015) 115412. doi:10.1103/PhysRevB.91.115412.
URL http://link.aps.org/doi/10.1103/PhysRevB.91.115412
[431] J. Quereda, V. Parente, P. San-José, N. Agraït, G. Rubio-Bollinger, F. Guinea, R. Roldán, A. Castellanos-Gomez, Quantum confinement in black phosphorus through strain-engineered rippling, ArXiv e-printsarXiv:1509.01182.
[432] C.-C. Liu, W. Feng, Y. Yao, Quantum spin hall effect in silicene and two-dimensional germanium, Phys. Rev. Lett. 107 (2011) 076802.
[433] Y. Li, Z. Chen, Tuning electronic properties of germanane layers by external electric field and biaxial tensile strain: A computational study, The Journal of Physical Chemistry C 118 (2) (2014) 1148–1154.
[434] C. Kamal, M. Ezawa, Arsenene: Two-dimensional buckled and puckered honeycomb arsenic systems, Phys. Rev. B 91 (2015) 085423. doi:10.1103/PhysRevB.91.085423.
URL http://link.aps.org/doi/10.1103/PhysRevB.91.085423
[435] R. Biele, E. Flores, J. R. Ares, C. Sanchez, I. J. Ferrer, G. Rubio-Bollinger, A. Castellanos-Gomez, R. D'Agosta, Strain induced bang-gap engineering in layered TiS_3, ArXiv e-printsarXiv:1509.00532.